

General Disclaimer

One or more of the Following Statements may affect this Document

- This document has been reproduced from the best copy furnished by the organizational source. It is being released in the interest of making available as much information as possible.
- This document may contain data, which exceeds the sheet parameters. It was furnished in this condition by the organizational source and is the best copy available.
- This document may contain tone-on-tone or color graphs, charts and/or pictures, which have been reproduced in black and white.
- This document is paginated as submitted by the original source.
- Portions of this document are not fully legible due to the historical nature of some of the material. However, it is the best reproduction available from the original submission.

A COMPARISON OF EXPERIMENTAL HEAT-TRANSFER COEFFICIENTS
IN A NOZZLE WITH ANALYTICAL PREDICTIONS FROM BARTZ'S METHODS
FOR VARIOUS COMBUSTION CHAMBER PRESSURES
IN A SOLID PROPELLANT ROCKET MOTOR

by

DEWEY M SMITH

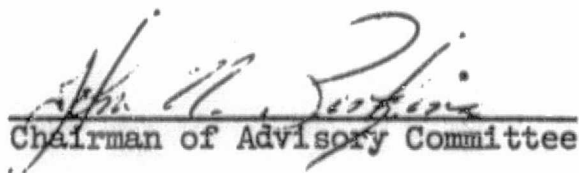
A thesis submitted to the Graduate Faculty of
North Carolina State University at Raleigh
in partial fulfillment of the
requirements for the Degree of
Master of Science

DEPARTMENT OF MECHANICAL AND AEROSPACE ENGINEERING

RALEIGH

1970

APPROVED BY:


Chairman of Advisory Committee



N69-40076

(ACCESSION NUMBER)

106

(PAGES)

TRX-61900

(NASA CR OR TMX OR AD NUMBER)

(THRU)

1

(CODE)

28

(CATEGORY)

ABSTRACT

SMITH, DEWEY M. A Comparison of Experimental Heat Transfer Coefficients in a Nozzle With Analytical Predictions From Bartz's Methods for Various Combustion Chamber Pressures in a Solid Propellant Rocket Motor. (Under the direction of JOHN NOBLE PERKINS.)

The experimental heat transfer coefficients measured in the nozzle of a small solid propellant motor are compared to the predictions from D. R. Bartz's Nusselt number correlation equation and his technique of solving the boundary layer momentum and energy equations simultaneously for the heat transfer coefficient. The propellant was a composite of ammonium perchlorate and polybutadiene acrylic acid and the average motor chamber pressures were 220, 410, and 742 psia. The nozzle was made with a steel casing and a ZTA graphite throat insert. Measurement locations were at a local to throat area ratio of 1.785 in the convergent section, at the throat and at a local to throat area ratio of 2.369 in the divergent section for the chamber pressures of 220 and 410 psia. The measurements were made at a local to throat area ratio of 2.067 in the convergent section, at the throat, and at a local to throat area ratio of 3.764 in the divergent section for the chamber pressure of 742 psia. Test measurements consisted of temperature responses of five thermocouples mounted on a line perpendicular to the heated surface of the nozzle at each of the measurement locations. The heating rates and the corresponding convective heat transfer coefficients were determined by using the thermocouple data as input to a finite difference heat balance program.

The results of the comparisons showed the experimental data from the convergent region and throat to be consistently lower than the predictions made using Bartz's two techniques. It was found that the experimental data in the divergent sections could be correlated by evaluating the skin friction coefficient at the free stream temperature and using it in the simultaneous solution.

ACKNOWLEDGMENTS

The author would like to thank the National Aeronautics and Space Administration for providing the opportunity to conduct this study through its graduate study program. Appreciation is also extended to the personnel at Langley Research Center who assisted in fabricating the test hardware, in conducting the tests, in reducing the test data, and in preparing this document.

The author thanks Dr. John N. Perkins, Chairman of his Advisory Committee, for his advice in organizing the study and for his suggestions concerning the presentation of the results. The constructive criticisms of Dr. J. C. Williams III, and Dr. W. J. Harrington were helpful.

The author expresses his appreciation to his wife, Rudeen, for her patience and encouragement throughout the course of this study.

TABLE OF CONTENTS

	Page
LIST OF SYMBOLS	iv
LIST OF TABLES	vii
LIST OF FIGURES	viii
INTRODUCTION	1
REVIEW OF THE LITERATURE	3
THEORY	8
DESCRIPTION OF EXPERIMENTAL TECHNIQUE	14
Discussion of Experimental Apparatus	14
Thermal and Physical Properties	16
Data Reduction	18
RESULTS	21
Presentation and Discussion of Results	21
Average Chamber Pressure of 220 psia	21
Average Chamber Pressure of 410 psia	24
Average Chamber Pressure of 742 psia	26
Accuracy of Results	27
SUMMARY AND CONCLUSIONS	30
LIST OF REFERENCES	32
APPENDIX	
Tables	34
Figures	36

LIST OF SYMBOLS

A_L	local area
A_t	throat area
a	exponent in Nusselt number correlation equation
b	exponent in Nusselt number correlation equation
C	constant in Nusselt number correlation equation
C_f	skin-friction coefficient based on R_θ
\bar{C}_f	low-speed adiabatic skin-friction coefficient
C_{fa}	adiabatic skin-friction coefficient
C_p	specific heat at constant pressure
D	diameter
D_*	throat diameter
\dot{H}_p	enthalpy flux of wall flow (potential)
\dot{H}_r	enthalpy flux of wall flow (real)
h_g	convective heat-transfer coefficient
K_{1-2}	average thermal conductivity in elements 1 and 2
K'_i	translational thermal conductivity of gas i
K''_i	internal thermal conductivity of gas i
M	Mach number
\dot{M}_p	momentum flux of the wall flow (potential)
\dot{M}_r	momentum flux of the wall flow (real)
m	exponent of temperature dependence of viscosity
\dot{m}_p	wall mass flux (potential)
\dot{m}_r	wall mass flux (real)

N_{Nu} or Nu	Nusselt number
N_{Pr} or Pr	Prandtl number
N_{Re} or Re	Reynolds number
N_{St} or C_h	Stanton number
n	boundary-layer interaction component
P_{avg}	average chamber pressure
P_c	chamber pressure
P_o	stagnation pressure
Q	heating rate
q_w	wall heating rate
R_θ	Reynolds number based on momentum thickness
\bar{R}_θ	low-speed Reynolds number corresponding to R_θ
T	static temperature in free stream or in calorimeter
T'	temperature calculated in previous time increment
T_{aw}	adiabatic wall temperature
T_o	stagnation temperature
T_w	wall temperature
t	time
\bar{t}	local time - mean static temperature in boundary layer
\bar{t}_o	local time - mean stagnation temperature in boundary layer
U	free-stream velocity
\bar{u}	local time - mean x-component of velocity in boundary layer

V	volume
x	distance along wall or mole fraction
y	distance from wall
Z	distance along axis of nozzle

Greek symbols

γ	specific heat ratio
Δ	temperature thickness of boundary layer
δ	velocity thickness of boundary layer
δ^*	displacement thickness of boundary layer
δ'	thickness of wall flow
θ	momentum thickness of the boundary layer
μ	viscosity of gas
μ_0	viscosity of gas at stagnation conditions
μ_{ref}	viscosity determined for a reference temperature
ν	number of gas constituents
ρ	density
$\bar{\rho}$	local time - mean density in boundary layer
ρ_{ref}	density based on a reference temperature
τ_w	shear stress at wall
ϕ	energy thickness of the boundary layer
ϕ_{ij}	parameter used in calculating mixture properties
ψ_{ij}	parameter used in calculating internal thermal conductivity of gas mixture

LIST OF TABLES

	Page
1. Variation of Motor Characteristics to Achieve Different Chamber Pressures	34
2. Exhaust Gas Properties	35

LIST OF FIGURES

	Page
1. Control volumes for real and potential flow in nozzle	36
(a) Control volume of real flow	36
(b) Control volume of potential flow	36
2. Nozzle for evaluation of constant in heat-transfer coefficient equation (from ref. 4)	37
3. Experimental solid-propellant motor schematic	38
4. Chamber pressure vs time - $P_{avg} = 220$ psia	39
5. Chamber pressure vs time - $P_{avg} = 410$ psia	40
6. Chamber pressure vs time - $P_{avg} = 742$ psia	41
7. Calorimeter locations within nozzle	42
8. Calorimeter dimensions	43
9. Experimental solid-propellant motor mounted in thrust stand	44
10. Instrumented nozzle on experimental solid-propellant motor	45
11. Specific heat - C_p vs temperature of ZTA graphite whose density is 119.3 lb/ft ³	46
12. Thermal conductivity vs temperature of ZTA graphite whose density is 119.3 lb/ft ³	47
13. ZTA graphite core finite elements	48
14. Comparison of experimental and calculated temperature response of thermocouples 1, 2, and 3. Convergent calorimeter - $P_c = 220$ psia	49
15. Heating rate vs burn time. Convergent calorimeter - $P_c = 220$ psia	50
16. Convective heat-transfer coefficient vs burn time. Con- vergent calorimeter - $P_c = 220$ psia	51
17. Comparison of experimental and calculated temperature response of thermocouples 1 and 2. Throat calorimeter - $P_c = 220$ psia	52

LIST OF FIGURES (Continued)

	Page
18. Heating rate vs burn time. Throat calorimeter - $P_c = 220$ psia	53
19. Convective heat-transfer coefficient vs burn time. Throat calorimeter - $P_c = 220$ psia	54
20. Comparison of experimental and calculated temperature response of thermocouples 1, 2, and 3. Divergent calorimeter - $P_c = 220$ psia	55
21. Heating rate vs burn time. Divergent calorimeter - $P_c = 220$ psia	56
22. Convective heat-transfer coefficient vs burn time. Diver- gent calorimeter - $P_c = 220$ psia	57
23. Comparison of analytical and experimental heat-transfer coefficients - $P_c = 220$ psia	58
24. Extrapolated thermocouple number 1 response. Convergent calorimeter - $P_c = 220$ psia	59
25. Extrapolated thermocouple number 1 response. Throat calorimeter - $P_c = 220$ psia	60
26. Dimensionless convective heat-transfer coefficient vs Reynolds number - $P_c = 220$ psia	61
27. Comparison of experimental and calculated temperature response of thermocouples 1, 2, and 3. Convergent calorimeter - $P_c = 410$ psia	62
28. Heating rate vs burn time. Convergent calorimeter - $P_c = 410$ psia	63
29. Convective heat-transfer coefficient vs burn time. Con- vergent calorimeter - $P_c = 410$ psia	64
30. Comparison of experimental and calculated temperature response of thermocouples 1, 2, and 3. Throat calorimeter - $P_c = 410$ psia	65
31. Heating rate vs burn time. Throat calorimeter - $P_c = 410$ psia	66
32. Convective heat-transfer coefficient vs burn time. Throat calorimeter - $P_c = 410$ psia	67

LIST OF FIGURES (Continued)

	Page
33. Comparison of experimental and calculated temperature response of thermocouples 1, 2, and 3. Divergent calorimeter - $P_c = 410$ psia	68
34. Heating rate vs burn time. Divergent calorimeter - $P_c = 410$ psia	69
35. Convective heat-transfer coefficient vs burn time. Divergent calorimeter - $P_c = 410$ psia	70
36. Comparison of analytical and experimental heat-transfer coefficients - $P_c = 410$ psia	71
37. Comparison of experimental and calculated temperature response of thermocouples 1, 2, and 3. Convergent calorimeter - $P_c = 742$ psia	72
38. Heating rate vs burn time. Convergent calorimeter - $P_c = 742$ psia	73
39. Convective heat-transfer coefficient vs burn time. Convergent calorimeter - $P_c = 742$ psia	74
40. Comparison of experimental and calculated temperature response of thermocouples 1, 2, and 3. Throat calorimeter - $P_c = 742$ psia	75
41. Heating rate vs burn time. Throat calorimeter - $P_c = 742$ psia	76
42. Convective heat-transfer coefficient vs burn time. Throat calorimeter - $P_c = 742$ psia	77
43. Comparison of experimental and calculated temperature response of thermocouples 1, 2, and 3. Divergent calorimeter - $P_c = 742$ psia	78
44. Heating rate vs burn time. Divergent calorimeter - $P_c = 742$ psia	79
45. Convective heat-transfer coefficient vs burn time. Divergent calorimeter - $P_c = 742$ psia	80
46. Comparison of experimental and analytical heat-transfer coefficients - $P_c = 742$ psia	81
47. Typical X-ray of calorimeters	82

LIST OF FIGURES (Concluded)

	Page
48. Comparison of analytical and experimental temperature distributions - $P_c = 220$ psia	83
49. Comparison of analytical and experimental temperature distributions - $P_c = 410$ psia	84
50. Comparison of analytical and experimental temperature distributions - $P_c = 742$ psia	85

INTRODUCTION

During recent years, attempts have been made to analytically predict heat transfer rates in the combustion chamber and along the nozzle wall of solid propellant rocket motors. The prediction techniques were developed by researchers in the liquid propellant rocket engine field and they have been fairly successful in defining the heating loads for this type engine.

The two most widely used methods for predicting the heat transfer rates were set forth by D. R. Bartz. The first method is a Nusselt number correlation equation which was developed before the advent of high speed computers and is still used today for rapid estimations. The second method solves the boundary layer momentum and energy equations for the heat transfer coefficient and requires the use of a computer.

These techniques are now being applied to solid propellant rocket motor nozzles. The experimental data on heat transfer rates for this type motor are not extensive and therefore it is difficult to determine the applicability of Bartz's techniques to solid propellant motors. Most of the nozzles on solid propellant motors are not externally cooled and their design is based on the materials in the nozzle wall being able to absorb the heat transferred from the exhaust gases. During the times immediately after ignition, severe temperature gradients are set up through the nozzle wall and this condition must be taken into consideration in the design. Accurate prediction of the heating loads is desirable so that the nozzle may be designed efficiently.

To provide additional experimental data, the heating rates in a converging - diverging nozzle on a small solid propellant rocket motor were measured at a point in the convergent region, at the throat, and at a point in the divergent region. The average chamber pressures were 220, 410, and 742 psia which represent the range of chamber pressures used in full scale motors. The heating rates were determined from the temperature responses of five thermocouples mounted on a line perpendicular to the heated surface of the nozzle at each of the measurement locations. The experimental heat transfer coefficients were then compared with predictions from the two techniques of Bartz. This thesis presents these comparisons and the intention is to provide some basis for applying the Bartz techniques to solid propellant rocket motor nozzles.

REVIEW OF THE LITERATURE

Bartz (4) has documented in detail the developments of both the analytical and the experimental research in rocket nozzle heat transfer. Published in 1965, it provides a convenient catalog of the most recent experimental results and techniques and was referred to often in the performance of the work for this thesis.

The initial prediction method of rocket nozzle heat transfer was based on the turbulent pipe flow heat transfer correlation equations of McAdams (13). This method assumed the flow in the nozzle to be fully developed with each point on the nozzle contour assumed to be preceded by a long pipe. Sibulkin and Bartz (15, 2) were the first to treat the nozzle heat transfer problem with a boundary layer approach by making use of the integral momentum and energy equations (Sibulkin's was an incompressible flow analysis). These treatments were an improvement over the McAdams equations since the flow in rocket nozzles is not usually fully developed. The main difference in Bartz's initial boundary layer analysis and the one used today is the method of solving the boundary layer equations. The original analysis was done before the advent of high speed computers. Bartz pointed out the equations were interdependent upon the ratios of wall temperature to stagnation temperature, $\frac{T_w}{T_0}$, and the temperature to velocity boundary layer thickness, $\frac{\Delta}{\delta}$. However, to simplify the mechanics of solution of the equations, he assumed initial values for these ratios and solved the two equations separately. The boundary layer equations were reduced to linear ordinary differential equations with variable coefficients.

The other basic assumptions in the analysis were:

(1) $1/7$ power law profiles of both velocity and the difference between stagnation temperature and wall temperature in the turbulent boundary layer,

(2) the local skin-friction coefficients along the nozzle are the same as those on a flat plate for the same boundary-layer thickness, and

(3) Reynolds analogy between momentum transfer and heat transfer applies for the nozzle boundary-layer flow. Elliot et al. (8) developed a computer program in 1963 that solves the boundary-layer equations simultaneously by an iterative method which allows the ratios, $\frac{T_w}{T_0}$ and $\frac{\Delta}{\delta}$, to vary along the nozzle wall.

A Nusselt number correlation equation was also developed by Bartz (3) for the purpose of making calculations of the local heat-transfer coefficients by hand. This method was based on the solution for the heat-transfer coefficient from the original boundary-layer analysis which showed the local coefficient to be strongly dependent upon the local mass flow rate. The boundary-layer solutions also showed that the local diameter should be used as the characteristic length in the correlation equation. The proportionality constant was obtained by matching the heat-transfer coefficients at the throat of a particular nozzle with the coefficient that was calculated from the boundary-layer analysis. This correlation equation is still used today for rapid calculations of the local heat-transfer coefficient.

Numerous experiments have been performed to determine the accuracy of the methods. These experiments, for the most part, have involved heat transfer measurements in nozzles with heated air or various liquid propellant exhaust gases as the working fluid. The heated air experiments are unique in that the inlet conditions to the nozzle can be controlled thus eliminating such combustion effects as secondary flows, oscillations in pressure, or free stream turbulence that can occur in rocket motors. Of particular interest are the data of Back, et al. (1) which are from heated air experiments with stagnation pressures ranging from 30 to 250 psia and stagnation temperatures over the 1000 -2000° R range. The nozzle was a 30-degree half-angle convergent, 15-degree half-angle divergent nozzle which is similar to the nozzles used in the set of tests reported on here.

The boundary layer analysis predicted the heat transfer coefficient accurately throughout the nozzle whereas the correlation equation was approximately 50 percent high for chamber pressures in the range 75 - 250 psia. One other interesting point was the indication that the boundary layer turbulence seemed to decay back toward transition of laminar flow near the throat in the lower stagnation pressure tests and was reflected in the heat transfer results.

The data obtained by Kolozsi (10), using air at stagnation pressures of 225 and 370 psia and stagnation temperatures of 1100 - 1200° R in a convergent-divergent nozzle, indicated the correlation equation predicted coefficients too high (45 percent high at the throat) and the boundary layer equations were accurate throughout the nozzle. Fortini and Ehlers (9) found that both methods predicted the heat

transfer coefficients accurately in a Rao-design divergent section nozzle using air at a stagnation pressure of 300 psia and a stagnation temperature of 1600° R. Their results also showed that two-dimensional flow must be considered in this type nozzle instead of one-dimensional flow that can be used in most convergent-divergent nozzles.

Welsh and Witte (19) used a N_2O_4 - hydrazine liquid propellant rocket engine to gather heat transfer data and compared it with only the correlation equation for stagnation pressures between 80 - 290 psia. They found the predictions to be considerably lower in the convergent region when compared with the experimentally determined coefficient, from 80 percent above to 45 percent below in the throat region, with the best correlation in the divergent section. They theorized that the effects of combustion in the vicinity of the nozzle inlet influenced the flow in the convergent and throat region. Convergent-divergent nozzle configurations were used in these tests with varying contraction ratios.

Witte and Harper (20) used the same liquid propellant engine used by Welsh and Witte (19) with nozzles over an extended range of contraction and supersonic area ratios. They had the same general results as in (19). They also concluded that the wide variation of data in the throat region of (19) was due to the transitional tendencies of the turbulent boundary layer here. This tendency was felt to be caused by the acceleration of the flow.

Lee (12) obtained experimental heat transfer data from a solid propellant motor with an uncooled molybdenum nozzle that was found to agree with Bartz's correlation equation. The data could be correlated also by assuming the skin friction coefficient to be dependent on the

momentum thickness and numerically integrating the boundary layer momentum equation. Brinsmade and Desmon (5) conducted tests with a solid propellant motor at stagnation pressures between 160 - 300 psia and a stagnation temperature of 4900° R and found that the data at the throat could be correlated by using laminar heat transfer equations.

THEORY

The integral momentum and energy equations of the turbulent boundary layer can be derived by writing momentum and energy balances on a control volume in the vicinity of the wall where there are viscous effects in a real fluid. This was the method used by Bartz (4). The derivation is based on the definitions of displacement, momentum, and energy thicknesses as the deficiencies in mass, momentum, and energy caused by friction and heat transfer. These deficiencies are determined by comparing real flow with potential flow near the wall where the mass flow rates are made equal in the control volume for these two types of flow (see Fig. 1).

The basic definitions are:

- (1) Displacement thickness

$$\delta^* = \delta'_r - \delta'_p = \int_0^{\delta'_r} \left(1 - \frac{\bar{\rho} \bar{u}}{\rho U} \right) dy \quad (1)$$

which is the difference in thickness in the two control volumes in order to have the mass flow rates equal.

- (2) Momentum thickness

$$\theta = \int_0^{\delta'_r} \frac{\bar{\rho} \bar{u}}{\rho U} \left(1 - \frac{\bar{u}}{U} \right) dy \quad (2)$$

which is the thickness of potential flow which has a momentum flux that is equal to the difference between the potential and real flow momentum fluxes for the same mass flux.

(3) Energy thickness

$$\delta = \int_0^{\delta^*} \frac{\bar{\rho}\bar{u}}{\rho U} \left(1 - \frac{T_o - T_w}{T_o - T_w} \right) dy \quad (3)$$

which is the thickness of potential flow that has an enthalpy flux equal to the difference between the enthalpy fluxes of the potential and real flows for the same mass flux. In forming these definitions, the time-mean flow density, $\bar{\rho}\bar{u}$, has been represented by the product of the mean values, $\bar{\rho}$ and \bar{u} , and ignoring the cross-correlation terms. This can be done on the assumption the correlation terms cancel out when integrated over the boundary layer as suggested by Shapiro (14).

Using these definitions in the momentum and energy balances on the control volumes in the potential and real flows, the following equations are formed:

(1) Integral Momentum Equation

$$\frac{d\theta}{dx} = \frac{C_f}{2} - \theta \left[\frac{1 + \frac{\delta^*}{\theta}}{U} \frac{dU}{dx} + \frac{1}{\rho U} \frac{d(\rho U)}{dx} + \frac{1}{r} \frac{dr}{dx} \right] \quad (4)$$

where C_f is defined as

$$C_f = \frac{2\tau_w}{\rho U^2} \quad (5)$$

(2) Integral Energy Equation

$$\frac{d\phi}{dx} = C_h \left(\frac{T_{aw} - T_w}{T_o - T_w} \right) - \phi \left[\frac{1}{\rho U} \frac{d(\rho U)}{dx} + \frac{1}{r} \frac{dr}{dx} - \frac{1}{T_o - T_w} \frac{dT_w}{dx} \right] \quad (6)$$

where C_h is defined as

$$C_h = \frac{q_w}{\rho U C_p (T_{aw} - T_w)} \quad (7)$$

The basic assumptions used by Bartz in solving these equations are as follows:

(1) The flow is axisymmetric and steady, the forces acting on the gas are the pressure gradient and skin friction at the wall, and the boundary layer is small compared to the distance from the axis of symmetry.

(2) The flow through the nozzle is reversible and adiabatic with the change in total enthalpy of the gas due to the heat flux to the wall.

(3) The gas is perfect, has a constant Prandtl number, and its viscosity is related to the gas temperature raised to a power.

(4) The skin-friction coefficient and the Stanton number are the same as they would be on a flat plate at the same free-stream conditions, wall temperature, and momentum thickness.

(5) The Stanton number for unequal momentum and energy thicknesses is that for equal thicknesses multiplied by $\left(\frac{\delta}{\theta}\right)^n$, where (n) is an "interaction component." The Stanton number for equal momentum and energy thicknesses is related to the skin-friction coefficient by von Karman's form of Reynold's analogy

$$C_h = \frac{\frac{C_f}{2}}{1 - 5 \left(\frac{C_f}{2}\right)^{1/2} \left[1 - Pr + \ln\left(\frac{6}{5Pr + 1}\right) \right]} \quad (8)$$

(6) Heat transfer has either no effect on the skin-friction coefficient, and C_f is the same as for adiabatic flow, or has an effect and the C_f is the same for adiabatic incompressible flow with

the density and viscosity evaluated at the arithmetic mean of the wall and free stream static temperatures.

(7) The boundary layer velocity and temperature distributions are 1/7-power profiles.

Values for the skin friction coefficient are taken from data of adiabatic flow over flat plates correlated by Coles (7). Coles found the data could be represented by one curve of \bar{C}_f versus $\bar{C}_f \bar{R}_\theta$ where the low speed value, \bar{C}_f , is related to the actual C_{fa} by

$$\bar{C}_f = C_{fa} \left(\frac{T_{aw}}{T} \right) \left(\frac{T_s}{T_{aw}} \right)^m \quad (9)$$

where T_s is a temperature within the boundary layer which is found by

$$\frac{T_s}{T_{aw}} = 1 + 17.2 \left(\frac{T_o}{T_{aw}} - 1 \right) \left(\frac{\bar{C}_f}{2} \right)^{1/2} - 305 \left(\frac{T_o}{T_{aw}} - \frac{T}{T_{aw}} \right) \frac{\bar{C}_f}{2} \quad (10)$$

and m is the exponent in the viscosity relationship, $\mu \sim T^m$. The \bar{R}_θ is related to R_θ by

$$\frac{C_{fa} R_\theta}{\bar{C}_f \bar{R}_\theta} = \frac{1}{\left(\frac{T_{aw}}{T} \right)^{1-m}} \quad (11)$$

A film temperature correction can be made by evaluating the gas properties ρ and μ , at the arithmetic mean temperature of the free stream temperature and the wall temperature. When this is done the relationship between C_f and \bar{C}_f is

$$\frac{C_f}{\bar{C}_f} = \frac{1}{\left[\frac{1}{2} \left(\frac{T_w}{T} + 1 \right) \right]^{\left(\frac{5-m}{4} \right)}} \quad (12)$$

The term, $\frac{\delta^*}{\theta}$, in the momentum equation can be evaluated from the integrals which define δ^* and θ , equations (1) and (2), by using the assumed 1/7-power profiles for the velocity and temperature ratio in the boundary layer. The limits on the integrals for these thicknesses as well as for the momentum thickness, ϕ , are expressed in terms of δ and Δ , which are not necessarily equal. Therefore the boundary layer momentum and energy equations are solved iteratively for θ and ϕ in order to determine the proper $\frac{\Delta}{\delta}$ as well as the proper skin friction coefficient.

The mass rate of flow per unit area through the nozzle can be determined from one dimensional isentropic relationships. By specifying the nozzle contour, wall temperature, and chamber conditions, the heat transfer coefficient at any point along the nozzle wall can be found from solving the boundary layer equations for the Stanton number, C_h :

$$C_h = \frac{h_c}{\rho U C_p} = \frac{q_w}{\rho U (T_{aw} - T_w)} \quad (13)$$

In the solutions for h_g developed by Bartz (2), it was found that the heat transfer coefficient was a strong function of the mass flow rate per unit area, ρU . From this, Bartz developed a nondimensional equation in the form

$$N_{Nu} = C \left(N_{Re} \right)^a \left(N_{Pr} \right)^b \quad (14)$$

for the determination of h_g . The analysis by Bartz (2) showed that ($a = 0.8$) and the exponent, b , was evaluated to be 0.4 from von Karman's modification of Reynold's analogy for $N_{Pr} = 1$. The characteristic length in the Reynolds number is the local diameter

which varies approximately with the boundary layer. One notable exception to this variation is in the entrance region of a nozzle where the boundary layer thickness may be small.

The constant C was evaluated by determining the heat transfer coefficient at the throat of the nozzle shown in Figure 2, with the boundary layer analysis and solving for C in equation (14) using this h_g . To insure that this equation would apply to other nozzle contours and conditions, a factor $\left(\frac{D_*}{r_c}\right)^{0.1}$, found from nozzle similarity studies in (2) was multiplied into the equation. If it is assumed that the specific heat, C_p , and the Prandtl number, Pr , are constant with temperature and that the gas properties ρ and μ are evaluated at a reference temperature to account for compressibility and/or heat transfer effects, equation (14) can be expressed as

$$h_g = \frac{.026}{D^{.2}} \left(\frac{D_*}{r_c}\right)^{0.1} \left(\frac{\mu^{0.2} C_p}{Pr^{0.6}}\right)_0 (\rho U)^{0.8} \left[\left(\frac{\rho_{ref}}{\rho}\right)^{0.8} \left(\frac{\mu_{ref}}{\mu}\right)^{0.2} \right] \quad (15)$$

This equation can be used to obtain a rapid estimation of the heat transfer distribution. It has been found to give good results except in the entrance region of nozzles with thin boundary layer thicknesses.

DESCRIPTION OF EXPERIMENTAL TECHNIQUE

Discussion of Experimental Apparatus

The rocket engine used to obtain the experimental heat transfer data is shown in the schematic in Figure 3. The solid propellant was a composite of 83.3 percent by weight ammonium perchlorate (oxidizer), 14.4 percent polybutadiene acrylic acid (fuel) and 2.3 percent stabilizer. This propellant was selected because there are only small amounts of solid particles (carbon residue) in the exhaust products, which minimizes heat transfer by radiation, and because its combustion chamber temperature is relatively low (about 4500° F). There is very little dissociation of the exhaust gases in this temperature range.

Average chamber pressures of 220, 410, and 742 psia were obtained by varying either the throat area or the volume of the combustion chamber and the amount of propellant. Table 1 gives the pertinent parameters for each of the chamber pressures used in the experiments. It was desirable to have a constant chamber pressure over the data taking period. To approximate this condition, the propellant was cast in a hollow cylinder configuration with the inner cylindrical surface being used as the exposed burning surface. Figures 4, 5, and 6 show the pressure traces for the three test conditions. It can be seen that a good approximation of constant chamber pressure with time was achieved.

The convergent-divergent nozzle was made with a ZTA graphite insert and a steel housing. The internal surface contour was made smooth and continuous which allowed an assumption to be made that the beginning of the boundary layer coincided with the beginning of

convergent section of the nozzle. The ZTA graphite was chosen as the material for the insert because of its machinability, resistance to erosion, and its thermal properties. Also by using the graphite insert, the experimental nozzle configuration was similar to nozzles used in full scale motors.

Heat transfer measurements were made in the convergent region, at the throat, and in the divergent region of the nozzle for the three test conditions. A degree of redundancy was obtained by using two calorimeters diametrically opposed in the divergent region. These calorimeters also were used to determine whether the gas flow through the nozzle was concentric. The exact locations of all four calorimeters in the nozzle for each of the tests are shown in Figure 7.

The calorimeters were made with a ZTA graphite core and a silica phenolic insulating sleeve. As can be seen in Figure 3, the graphite core was exposed directly to the flow of gases. By making both the insert and the calorimeter core out of the same material, there was very little disruption of the temperature distribution along the nozzle wall. The insulating sleeve was used to direct the heat flow along the longitudinal axis of the calorimeter. This allows the assumption of one-dimensional heat transfer to be made in the data reduction. The graphite core of the calorimeters was instrumented with five thermocouples. The thermocouple nearest the exposed surface was composed of tungsten -5 percent rhenium and tungsten -26 percent rhenium wires 5 mils in diameter. The other four thermocouples were made of platinum and platinum -13 percent rhodium wires also 5 mils in diameter. Figure 8 shows the locations of the thermocouples along the

longitudinal axis of the core. All calorimeters used in the tests were similarly constructed.

By using five thermocouples in each calorimeter, a temperature distribution through the calorimeter could be obtained even if there were random failures of individual thermocouples. Also the thermal diffusivity of the graphite could be checked by specifying the temperature-time history of one thermocouple in the data reduction analysis and comparing the calculated temperature distribution through the calorimeter with the distribution obtained from the experiment. This procedure will be demonstrated in a later section.

Ideally, the surface temperature of the calorimeter should be directly measured. However, due to the extreme thermal environment at the surface, this measurement is very difficult to make. The surface temperatures of the calorimeters were determined by locating a thermocouple as closely as possible to the surface and extrapolating the temperature data to the calorimeter exposed surface.

All of the heat transfer measurements were taken from static firings of the rocket engine. Figures 9 and 10 show the engine in position on the thrust stand. The thermocouple data as well as chamber pressure and thrust data were recorded on magnetic tape with a computerized data acquisition system.

Thermal and Physical Properties

The exhaust gas constituents were determined by assuming the products of combustion to be in chemical equilibrium at the prescribed pressure and enthalpy in the combustion chamber. Table 2 presents the conditions in the combustion chamber for the three tests and the

resulting mole fractions of each exhaust gas constituent as well as the specific heat ratio, γ , and the specific heat at constant pressure, C_p , for the gas mixture. These values were determined with the use of a computer program described by Zeleznik and Gordon (21). The gas mixture was assumed not to vary in the nozzle (frozen flow) and local conditions at the test measurement locations were determined by expanding the mixture isentropically through the nozzle.

The viscosity and thermal conductivity of the gas mixture were determined by using the equations suggested by Brokaw (6):

$$\mu_{\text{Mix}} = \sum_{i=1}^{\nu} \frac{\mu_i}{1 + \sum_{\substack{j=1 \\ j \neq i}}^{\nu} \phi_{ij} \frac{X_j}{X_i}} \quad (14)$$

$$K'_{\text{Mix}} = \sum_{i=1}^{\nu} \frac{K'_i}{1 + \sum_{\substack{j=1 \\ j \neq i}}^{\nu} \psi_{ij} \frac{X_j}{X_i}} \quad (15)$$

$$K''_{\text{Mix}} = \sum_{i=1}^{\nu} \frac{K''_i}{1 + \sum_{\substack{j=1 \\ j \neq i}}^{\nu} \phi_{ij} \frac{X_j}{X_i}} \quad (16)$$

$$K_{\text{Mix}} = K'_{\text{Mix}} + K''_{\text{Mix}} \quad (17)$$

These equations express the mixture viscosity and thermal conductivity in terms of the viscosity and thermal conductivity of the

mixture constituents. The constituents that are starred in Table 2 were accounted for in these calculations since they represent the major quantities in the mixture. The viscosity and thermal conductivity of each component were taken from data presented by Svehla (16). Their values were evaluated at the combustion chamber temperature.

The properties of the ZTA graphite used in the calorimeter core that are required are the density, constant pressure, specific heat, and the thermal conductivity. The density and specific heat data were taken from (17). The thermal conductivity data were taken from the results of Wagner and Dauelsberg (18). Figures 11 and 12 show the variation of the specific heat and thermal conductivity of ZTA graphite with temperature. The thermal conductivity shown is for the "across the grain" direction of the graphite which was the direction of heat flow in the calorimeters. It can be seen in the figure that the experimental data used to determine the curve is scattered. The thermal conductivity of any graphite is difficult to control. The effects of this variation on the test data will be discussed in the "Accuracy of Results" section. The density and specific heat of graphites do not vary nearly as much and can be controlled readily.

Data Reduction

All of the experimental data were recorded on magnetic tape so that the data could be reduced by computers. The thermocouple millivolt readings were converted into degree Fahrenheit according to National Bureau of Standards conversion tables. The temperature data were printed out in specified time increments over the firing time of the

rocket motors. The chamber pressure data were reduced in a similar manner.

The heat flux into the calorimeter was determined by dividing the graphite core into 20 finite elements (Fig. 13), and specifying the temperature-time history of the third element. The temperature-time history was that of thermocouple 1, the thermocouple nearest the heated surface in each calorimeter. By using a finite element technique, heat balance equations can be written for each of the elements over small time increments. For example, considering the heat flow to be one dimensional, the heat balance on element 1 is

$$Q_{in} = Q_{out} + Q_{stored} \quad (16)$$

$$h_g (T_{aw} - T_1) = \frac{K_1 - 2}{\Delta X_1 - 2} (T_1 - T_2) + \rho V_1 C_{p1} \frac{(T_1 - T_1')}{\Delta t} \quad (17)$$

where T_1' is the temperature of element 1 calculated in the previous time interval. After the heat balance equations are written for each of the elements, these equations may be solved simultaneously for the heat transfer coefficient.

A computer program was used to solve for the heat transfer coefficient versus firing time for each of the calorimeters. The program utilizes the Gauss-Jordan method to solve the simultaneous linear heat balance equations. In addition to a temperature-time history of one of the elements, necessary input data include the physical dimensions of each element and the thermal properties of the material (K , ρ , and C_p) which may vary with temperature. Output includes the heat transfer coefficient, the heating rate at the surface

of the calorimeter, and the temperature gradient along the longitudinal axis of the calorimeter for each specified time increment.

Radiative heating from the exhaust gases was not accounted for in the analysis. This was based on the fact, as discussed by Kuby (11), that gases radiate energy in finite frequency bands as opposed to most solid bodies which radiate in a energy continuum and therefore the total integrated value of emitted energy is much less for gaseous radiation. The propellant used in the tests was chosen because the amount of solid particles in its exhaust gases is small enough to be neglected. By not accounting for the radiation from the exhaust products, the data reduction is simplified, and the results are not effected substantially.

RESULTS

Presentation and Discussion of Results

Experimental heat transfer coefficients determined for average chamber pressures of 220, 410, and 742 psia are presented. The experimental coefficients are compared with theoretical coefficients determined from the two methods of Bartz. In determining the theoretical coefficients with the simultaneous solution of the boundary layer momentum and energy equations, the skin friction coefficient was evaluated at the arithmetic mean between the free stream and wall temperature as well as at the free stream temperature. Also, the theoretical coefficient was evaluated with an "interaction component" value of 0.1 as recommended by Bartz and also with a value of zero which essentially decouples the momentum and energy equations.

Other data presented are the calculated temperature distribution derived from the temperature data from the thermocouple 1 of each calorimeter. This calculated temperature distribution is compared with the temperature readings of the thermocouple mounted along the longitudinal axis of the calorimeters to determine the accuracy of the experimental data. The deviations between thermocouple readings and the calculated temperatures are discussed in the "Accuracy of Results" section. The experimental heating rates are also presented.

The thermocouples are numbered consecutively from one to five with thermocouple 1 located nearest the heated surface of each calorimeter.

Average Chamber Pressure of 220 psia

Experimental heat transfer data were obtained at a local area to throat area ratio, $\frac{A_1}{A_t}$, of 1.785 in the convergent section of the

nozzle, at the nozzle throat, $\frac{A_1}{A_t} = 1$, and in the divergent section at $\frac{A_1}{A_t} = 2.369$. Figures 14 through 22 show the temperature response of the three thermocouples nearest the heated surface in each of the calorimeters, the experimental heating rates, and the experimental heat transfer coefficients. The oscillatory nature of the heating rate and heat transfer coefficient curves is due to the data reduction technique rather than physical conditions in the test.

The heating rate curves show a decline in the magnitude of the heat flux with increasing time. This is to be expected since the driving potential, $(T_{aw} - T_w)$, becomes smaller with increasing time. However, the heat transfer coefficients calculated from the measured temperatures in the convergent section and at the throat also decreased with time. In Figure 23 it can be seen that both of Bartz's methods overpredict the heat transfer coefficient throughout the nozzle. The heat transfer data from the latter part of the firing can be correlated by using a laminar flow equation used in (12):

$$N_{St} \times N_{Pr}^{0.6} = \frac{1}{3} N_{Re_D}^{-0.5} N_{Pr}^{-0.067} \quad (18)$$

This is Pohlhausen's equation for laminar flow where the characteristic length has been changed to the local diameter since the flow is internal. The heat transfer coefficient determined from the experimental data in the divergent region of the nozzle did not vary as much as the throat and convergent heat transfer coefficients. The predictions from the simultaneous solutions, where the skin friction coefficient was evaluated at the free stream temperature, and from the laminar flow equation bracketed the test data in the divergent region.

The leveling of the slope of the temperature curves of thermocouple 1 in the convergent and throat calorimeters seemed unusual. In order to determine if the temperature data were valid, a temperature-time response of thermocouple 1 in each calorimeter was assumed as shown in Figures 24 and 25. These assumed temperature responses were used to compute the temperature response throughout the calorimeter with the use of the finite element computer program. Figures 24 and 25 show that on comparing the results using the assumed response with thermocouples 2 and 3 in the convergent calorimeter and thermocouple 2 in the throat calorimeter, the assumed temperature response was incorrect. The calculated responses were higher than the experimental responses at the locations where temperature were measured. These comparisons lend credence to the experimental data which show that the heat transfer coefficient becomes smaller with time.

It is known (4) that cooling the laminar boundary layer increases the stability, i.e., increases the critical Reynolds number for transition to turbulent flow. The boundary layer in this test was cooled by the nozzle wall throughout the test but to a lesser extent as time increased. Thus, it could be assumed that the conditions for laminar flow became less suitable at later times in the firing. The experimental data, however, indicate a tendency from turbulent or transition flow to laminar flow with increasing time.

It is generally assumed (4) that boundary layer heat transfer coefficients are affected by wall temperature. This is accounted for by evaluating the skin friction coefficient and the gas transport properties at some intermediate temperature between the adiabatic and wall temperature. Figure 23 shows the difference between evaluating the skin friction

coefficient at the free stream temperature and the arithmetic mean of the free stream and wall temperature for turbulent flow. Increasing wall temperature would tend to lower the heat transfer coefficient but not to the extent experienced in the test.

A favorable pressure gradient tends to stabilize a laminar boundary layer and since the local pressure decreases along the length of the nozzle, a turbulent boundary layer could revert to laminar flow. In Figure 26 the experimental data from the 220 psia chamber pressure test is compared with experimental data presented in (12). The figure is a plot of the parameter, Stanton number multiplied by the Prandtl number to the 0.6 power versus free stream Reynolds number based on the local diameter. It can be seen that the data reported on herein falls within the transition region as defined in (12). These results suggest that it is possible for laminar or transition flow to occur in a rocket motor nozzle even though the exhaust gases originate from a combustive process within the motor chamber that is highly turbulent.

Average Chamber Pressure of 410 psia

The nozzle used in this test was the same as that used in the 220 psia test with measurements made at the same locations. The additional pressure was generated by coupling two motor cases together with the head end case containing only half as much propellant as the second case. This method gave a chamber pressure that varied more than in the 220 psia test.

Figures 27 through 35 show the temperature response of the three thermocouples nearest the surface in each of the calorimeters, the heating rates, and the experimental heat transfer coefficients.

Figure 36 shows a comparison of the experimentally determined coefficients with the several methods of predicting the coefficients. It can be seen that, as in the 220 psia test, both of the Bartz methods overpredict the heat transfer coefficients, with the technique of evaluating the skin friction coefficient at the free stream temperature coming nearest to correlating the data. The heat transfer coefficient at the throat of the nozzle decreased sharply with time. This is also occurred to a lesser extent at the convergent calorimeter. The local Reynolds number at the convergent, throat, and divergent calorimeter was 0.723×10^6 , 1.02×10^6 , and 0.798×10^6 , respectively, indicating turbulent flow when compared to the data in (12). The drastic reduction of the heat transfer coefficient at the throat is questionable in view of the fact that the Reynolds number at the throat indicates turbulent flow and that the magnitude of the coefficient drops slightly below that of the convergent calorimeter. The initial 1.5 to 2.0 seconds of data do indicate that the Bartz methods slightly overpredicted the results of the test at the throat.

There was very little variation with time in the heat transfer coefficient on the divergent calorimeter. By evaluating the skin friction coefficient at the free stream temperature, the heat transfer coefficient was very nearly predicted. The convergent calorimeter data did show some decrease in the heat transfer coefficient. The heat transfer data at this point was slightly overpredicted by using the free stream skin friction coefficient in the simultaneous solution.

As mentioned before, there was some variation in the chamber pressure. An average chamber pressure of 410 psia was used in the analytical solutions. The chamber pressure varied from 440 psia in the

initial stages of the firing to 360 psia just before burnout. Using the Nusselt number correlation equation, where the heat transfer coefficient is proportional to the 0.8 power of the chamber pressure, to determine the effect on the heat transfer coefficient, it is found that the chamber pressure variation would theoretically cause the heat transfer coefficient to vary 6.5 percent above to 9.8 percent below that for an average chamber pressure of 410 psia. The change in chamber pressure could partially explain the reduction in heat transfer coefficients at the convergent calorimeter and at the throat calorimeter.

Average Chamber Pressure of 742 psia

The nozzle contour for this test was slightly different for this test in order to increase the chamber pressure to 742 psia. The contour still included at 45° half angle convergent region and a 15° half angle exit cone, but had a smaller throat diameter. Heat transfer measurements were made at an area ratio, $\frac{A_1}{A_t} = 2.067$ in the convergent region, $\frac{A_1}{A_t} = 1$, at the throat, and at $\frac{A_1}{A_t} = 3.764$, in the divergent region. Figures 37 through 45 show the temperature responses of the three thermocouples nearest the heated surfaces in each of the calorimeters, the heat fluxes calculated from the temperature responses, and the resulting heat transfer coefficients. Figure 46 compares the experimental results with the various analytical prediction methods. This figure shows the data to be slightly overpredicted when the free stream skin friction coefficient is used in the simultaneous solution. The convergent region data showed very little variation of the heat transfer coefficient during the burning of the motor although the overprediction

was the largest at this measurement location. The heat transfer coefficient at the throat was in the range of the predictions that used the free stream skin friction coefficient initially and decreased as the burning progressed. The divergent calorimeter data agreed very nearly with the predictions of the method stated above.

Accuracy of Results

The accuracy of the experimental results can be broken down into two parts:

- (1) Accuracy of the measured data.
- (2) Accuracy of the method of data reduction.

Factors which affect the accuracy of the measured data are the ability to determine the true location of the thermocouples with respect to the nozzle internal wall and the error introduced by the recording equipment. Factors which affect the accuracy of the data reduction are how well the properties of the ZTA graphite can be determined, i.e., the density and the constant pressure specific heat and thermal conductivity as a function temperature, and how accurate the method of data reduction is.

The location of the thermocouples in the calorimeter could be determined to within ± 0.003 inch by using close tolerances in the fabrication of the calorimeter and X-raying each calorimeter. Figure 47 is a typical X-ray photograph. The tolerances on the installation of the calorimeter in the nozzle were such that the true location of the thermocouples with respect to the nozzle internal wall could be determined to within ± 0.008 inch. This resulted in a band of uncertainty of the temperature distribution along the length of the calorimeter as shown in Figure 48.

The thermocouples used in the tests could measure true temperature within 1 percent. The noise in the recording channels of the measuring equipment could be filtered so that there was negligible error in the recording of the temperatures.

As stated before, the experimental data on the thermal conductivity of ZTA graphite is scattered (Fig. 12). In attempting to fit the temperature data from the thermocouple 1 with the experimental temperature distribution, it was necessary to vary the thermal conductivity of the graphite. The curves shown in the figures that present the temperature data versus time represent a "best fit." Since the thermal conductivity of the graphite varies with temperature, the thermal conductivity versus temperature curve had to be varied rather than a thermal conductivity value. The density and constant pressure specific heat versus temperature of ZTA graphite are accurately known (18) and error in their values were not considered in the analysis.

In order to determine the effect of the ± 0.008 inch error in the location of the thermocouple 1, an error analysis was made by varying its location in the data reduction. The calculated heat input to the nozzle wall was found to vary ± 5 percent during the early times in the test with the variation decreasing to ± 2 percent during the later times in the test. This variation was in the calculated heat input only. As previously stated, the experimental data was not perfectly fitted with the calculated data based on the temperature data of thermocouple 1. Figures 48 through 50 show the percent difference between the heat input based on the temperature data of thermocouples 1, 2, and 3 and the calculated heat input for late times in the tests.

The percent difference was determined by comparing the slopes of curves at the heated surface of the calorimeter since the heat input is:

$$\dot{q}_w = -K \left. \frac{\partial T}{\partial x} \right|_{\text{surface}} \quad (19)$$

The thermal conductivity was not varied since the difference in surface temperature of the two curves was not large.

In the figures that show the calculated heat input and the calculated heat transfer coefficients, there is oscillation in the curves caused by the data reducing process rather than any physical phenomena occurring in the tests. This was caused by the large change in temperature of the graphite in a short time, the temperature variation of the specific heat and thermal conductivity of the graphite, and the fact that a finite difference technique was used.

In summary, the heat transfer results from the tests were not exact results. However, the data did show trends which were presented and discussed previously.

SUMMARY AND CONCLUSIONS

The experimental heat transfer coefficients obtained by firing a solid propellant rocket motor at chamber pressures of 220, 410, and 742 psia were generally below the predictions made by the Bartz methods of solving the boundary layer energy and momentum equations simultaneously and the Nusselt number correlation equation.

The test at 220 psia chamber pressure demonstrated that it is possible to obtain laminar or transitional boundary layer flow in a solid propellant motor even though a turbulent combustive process is occurring in the motor chamber. The best agreement was found in the divergent region of the nozzles at all three pressures where the experimental coefficients were only slightly below the predictions from the simultaneous solution and evaluating the skin friction coefficient at the local free stream temperature.

Data from the convergent and throat calorimeters indicated the heat transfer coefficient decreases with increasing wall temperature. This variation was more pronounced than the variation in the predictions when the skin friction coefficient was evaluated at the arithmetic mean of the free stream and wall temperature (film temperature). The predictions using the film temperature skin friction coefficient were always above the experimental heat transfer coefficients in magnitude. Predictions using the skin friction coefficient evaluated at the free stream temperature were in the same range of the experimental data, but they do not account for wall temperature variation.

These results tend to substantiate the data in the literature in the respect that predicting heat transfer rates in the inlet portion of

a rocket motor nozzle is difficult (4, 19, 20) and that transitional and laminar flow along the nozzle wall is possible (1, 5, 12). The data in (5, 12) were collected from nozzles similar to the nozzles used in the tests reported on here and for similar combustion chamber conditions (P_C on the order of 200 psia). The data from (1) showed the transitional flow phenomena to occur at a lower combustion chamber pressure (75 psia).

These test data indicate that by using either the Bartz simultaneous solution or the Nusselt number correlation equation recommended by Bartz, calculations of the heating load along a nozzle wall would be conservative in that the analytical heat transfer coefficient is higher than the experimental coefficient. It is felt, however, that the degree of conservatism will hamper efforts to have an efficient nozzle design. Further analytical and experimental efforts are needed to refine and improve Bartz's methods.

It should be noted that these sets of data are not a complete test of the Bartz methods since the data was derived from the use of one type of nozzle. A complete conclusion may be drawn when test data are available from a variety of propellants and nozzles used on solid propellant motors.

LIST OF REFERENCES

1. Back, L. H., Massier, P. F., and Gier, H. L. 1964. Convective Heat Transfer in a Convergent-Divergent Nozzle. Intern. J. Heat Mass Transfer 7(5), 549-568.
2. Bartz, D. R. 1955. An Approximate Solution of Compressible Turbulent Boundary-Layer Development and Convective Heat Transfer in Convergent-Divergent Nozzles. Trans ASME, 77(8), 1235-1245.
3. Bartz, D. R. 1957. A Simple Equation for Rapid Estimation of Rocket Nozzle Convective Heat Transfer Coefficients. Jet Propulsion 27(1), 49-51.
4. Bartz, D. R. 1965. Turbulent Boundary-Layer Heat Transfer From Rapidly Accelerating Flow of Rocket Combustion Gases and of Heated Air. Advances in Heat Transfer, Vol. 2. Edited by James P. Hartnett and Thomas F. Irvine, Jr., Academic Press, New York.
5. Brinsmade, A. F., and Desmon, L. G. 1964. Hypothesis for Correlating Rocket Nozzle Throat Convective Heat Transfer. Chemical Engineering Progress Symposium Series, No. 59, Vol. 61, 88-98.
6. Brokaw, R. S. 1961. Alignment Charts for Transport Properties Viscosity, Thermal Conductivity, and Diffusion Coefficients for Nonpolar Gases and Gas Mixtures at Low Density. NASA Technical Report R-81.
7. Coles, D. E. 1961. The Turbulent Boundary Layer in a Compressible Fluid. Rand Corporation, Report Number P-2417, Santa Monica, California.
8. Elliot, David G., Bartz, Donald R., and Silver, Sidney. 1963. Calculations of Turbulent Boundary-Layer Growth and Heat Transfer in Axisymmetric Nozzles. Jet Propulsion Laboratory. Technical Report No. 32-387, Pasadena, California.
9. Fortini, A., and Ehlers, R. C. 1963. Comparison of Experimental to Predicted Heat Transfer in a Bell-Shaped Nozzle With Upstream Flow Disturbances. NASA TN D-1473.
10. Kolozsi, J. J. 1958. An Investigation of Heat Transfer Through the Turbulent Boundary-Layer in an Axially Symmetric, Convergent-Divergent Nozzle. Masters Thesis, Dept. of Aeronautical and Astronautical Engineering, Ohio State University, Columbus, Ohio.
11. Kuby, W. C. 1964. The Internal Environment of a Solid Propellant Rocket Nozzle. AIAA Preprint No. 64-158.

12. Lee, Roland E. 1963. Heat Transfer to the Throat Region of a Solid Propellant Rocket Nozzle. United States Naval Ordnance Laboratory, TR 62-72, White Oak, Maryland.
13. McAdams, W. H. 1954. Heat Transmission, 3rd ed. McGraw-Hill Book Company, New York.
14. Shapiro, A. H. 1954. The Dynamic and Thermodynamics of Compressible Fluid Flow, Vol. 2. The Ronald Press Company, New York.
15. Sibulkin, M. 1956. Heat Transfer to an Incompressible Turbulent Boundary Layer and Estimation of Heat Transfer Coefficients at Supersonic Nozzle Throats. J. Aeron. Sci. 23(2), 162-172.
16. Svehla, R. A. 1962. Estimated Viscosities and Thermal Conductivities of Gases at High Temperatures. NASA Technical Report R-132.
17. Union Carbide Corporation. 1964. Industrial Graphite Engineering Handbook. Union Carbide Corporation, New York.
18. Wagner, P., and Dauelsberg, L. B. 1966. Thermal Conductivity of ZFA Graphite. Los Alamos Scientific Laboratory. Report Number DC-8163, Los Alamos, New Mexico.
19. Welsh, W. E., Jr., and Witte, A. B. 1962. A Comparison of Analytical and Experimental Local Heat Fluxes in Liquid-Propellant Rocket Thrust Chambers. J. Heat Transfer 84(1), 19-28.
20. Witte, A. B., and Harper, E. Y. 1963. Experimental Investigation of Heat Transfer Rates in Rocket Thrust Chambers. AIAA J. 1(2), 443-451.
21. Zeleznik, Frank J., and Gordon, Sanford. 1962. A General IBM 704 or 7090 Computer Program for Computation of Chemical Equilibrium Composition, Rocket Performance, and Chapman-Jouguet Detonations, NASA TN D-1454.

A P P E N D I X

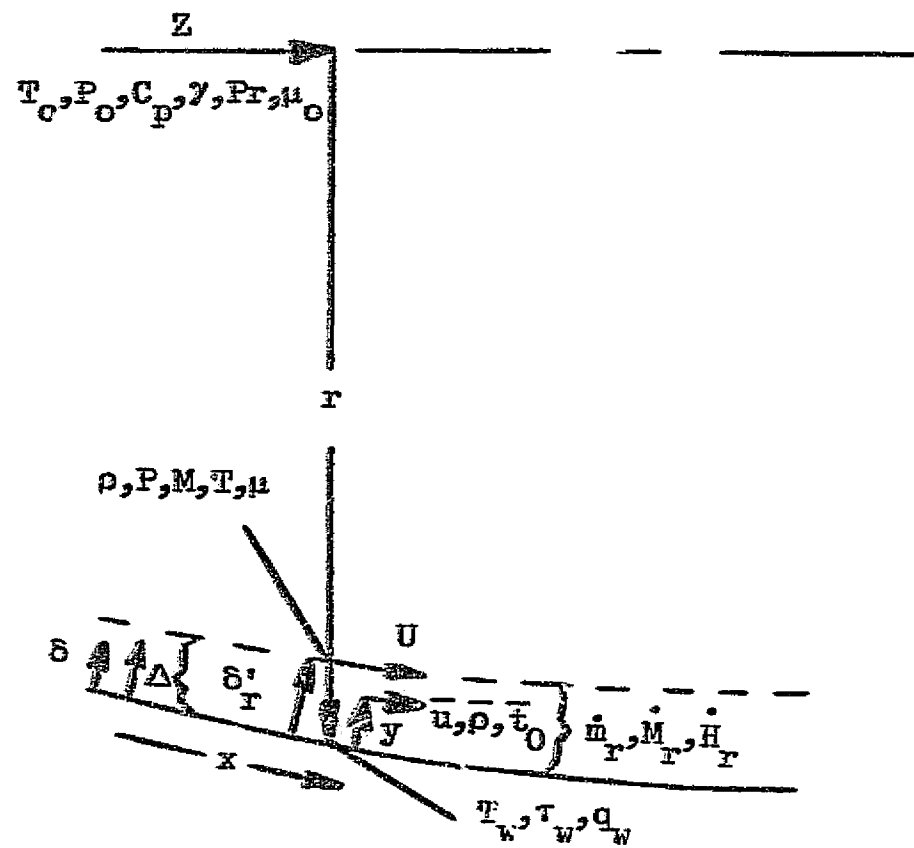
Table 1. Variation of Motor Characteristics to Achieve Different Chamber Pressures

Average Chamber Pressure, psia	Throat Area, in ²	Combustion Chamber Volume, in ³	Pounds of Propellant
220	1.238	322	6.75
410	1.238	644	10.13
742	0.592	322	6.75

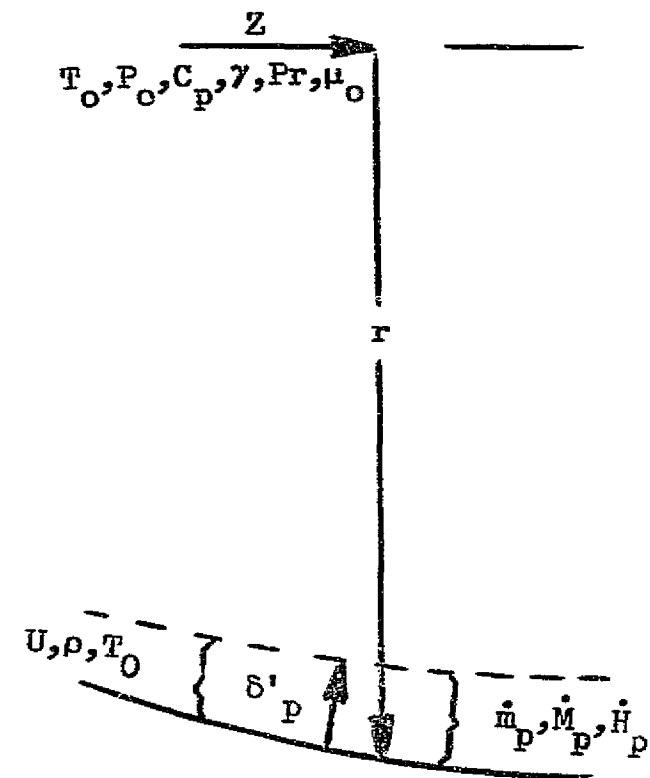
Table 2. Exhaust Gas Properties

Average chamber pressure, psia	220	410	742
Chamber gas temperature, °R	4845	4880	4900
Specific heat ratio	1.23	1.23	1.23
Specific heat constant. Pressure, $\frac{\text{Btu}}{\text{lb } ^\circ\text{R}}$	0.443	0.443	0.443
Viscosity, $\frac{\text{lb}}{\text{ft sec}}$	48.6×10^{-6}	48.6×10^{-6}	48.6×10^{-6}
Thermal conductivity $\frac{\text{Btu ft}}{\text{ft}^2 \text{sec } ^\circ\text{R}}$	35.8×10^{-6}	35.8×10^{-6}	35.8×10^{-6}
Exhaust gas constituents, mole fractions			
	CO	0.193	*
	CL	0.005	
	CO ₂	0.082	*
	H	0.005	
	H ₂	0.119	*
	HCL	0.167	*
	H ₂ O	0.336	*
	N ₂	0.089	*
	OH	0.004	

Note: Mole fractions of constituents did not vary with chamber pressure.



(a) Control volume of real flow



(b) Control volume of potential flow

Figure 1. Control volumes for real and potential flow in nozzle

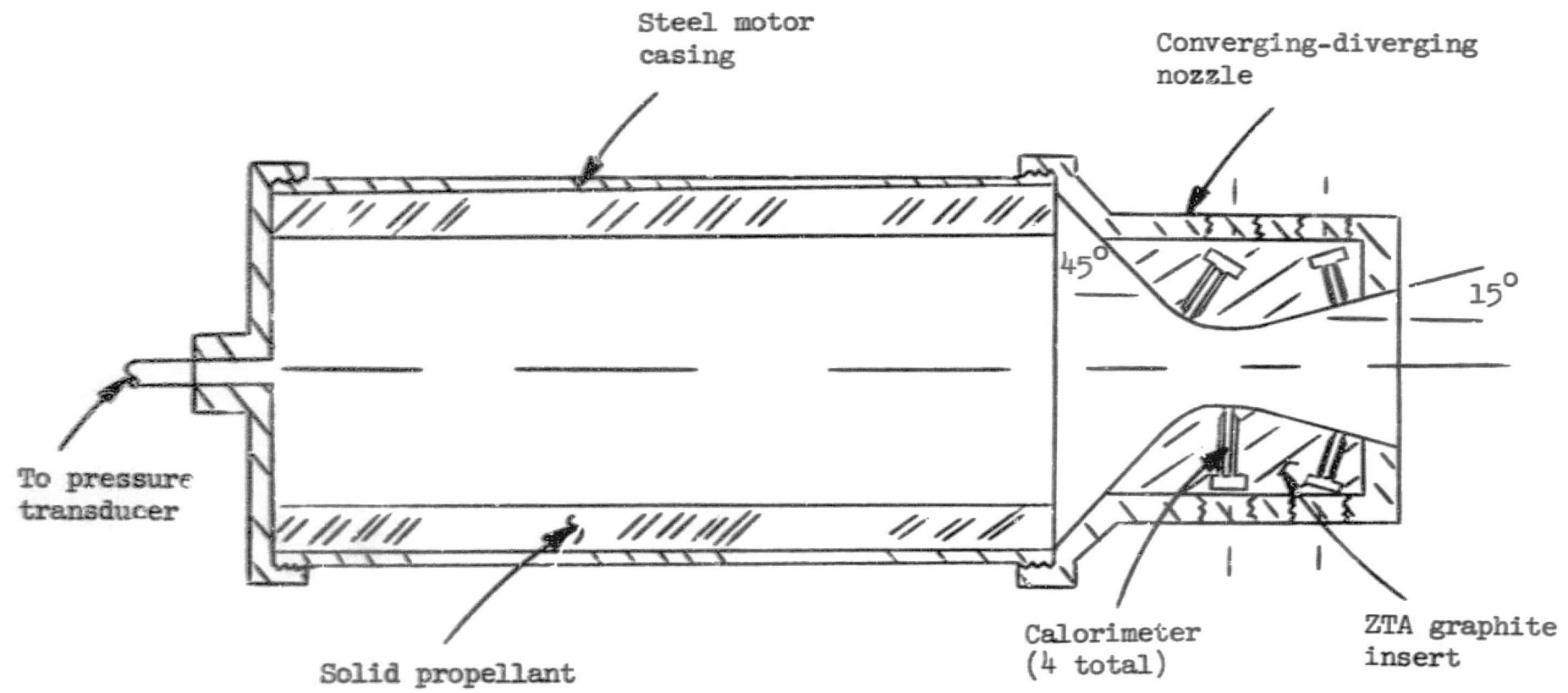


Figure 3. Experimental solid-propellant motor schematic

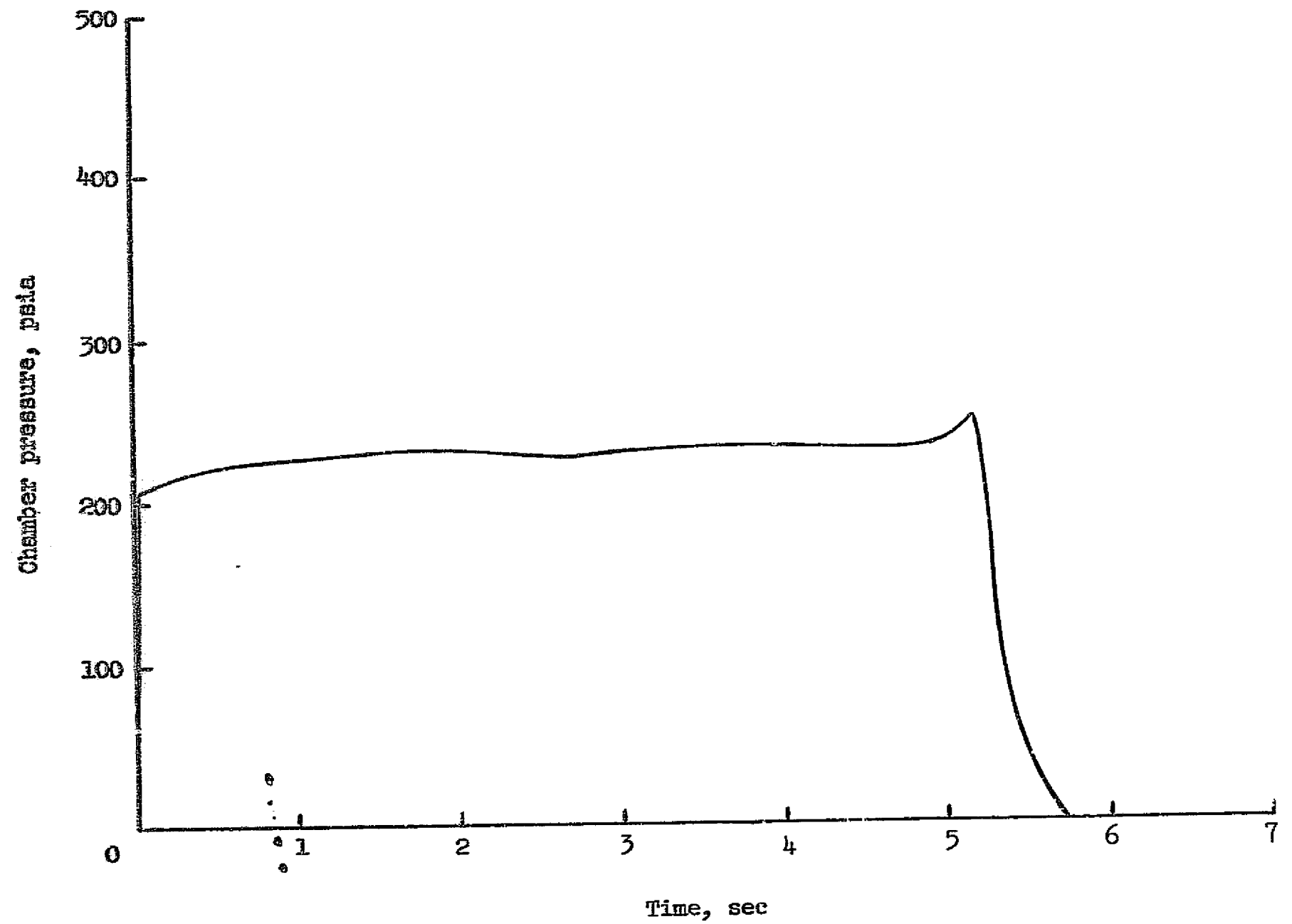


Figure 4. Chamber pressure vs time - $P_{avg} = 220$ psia

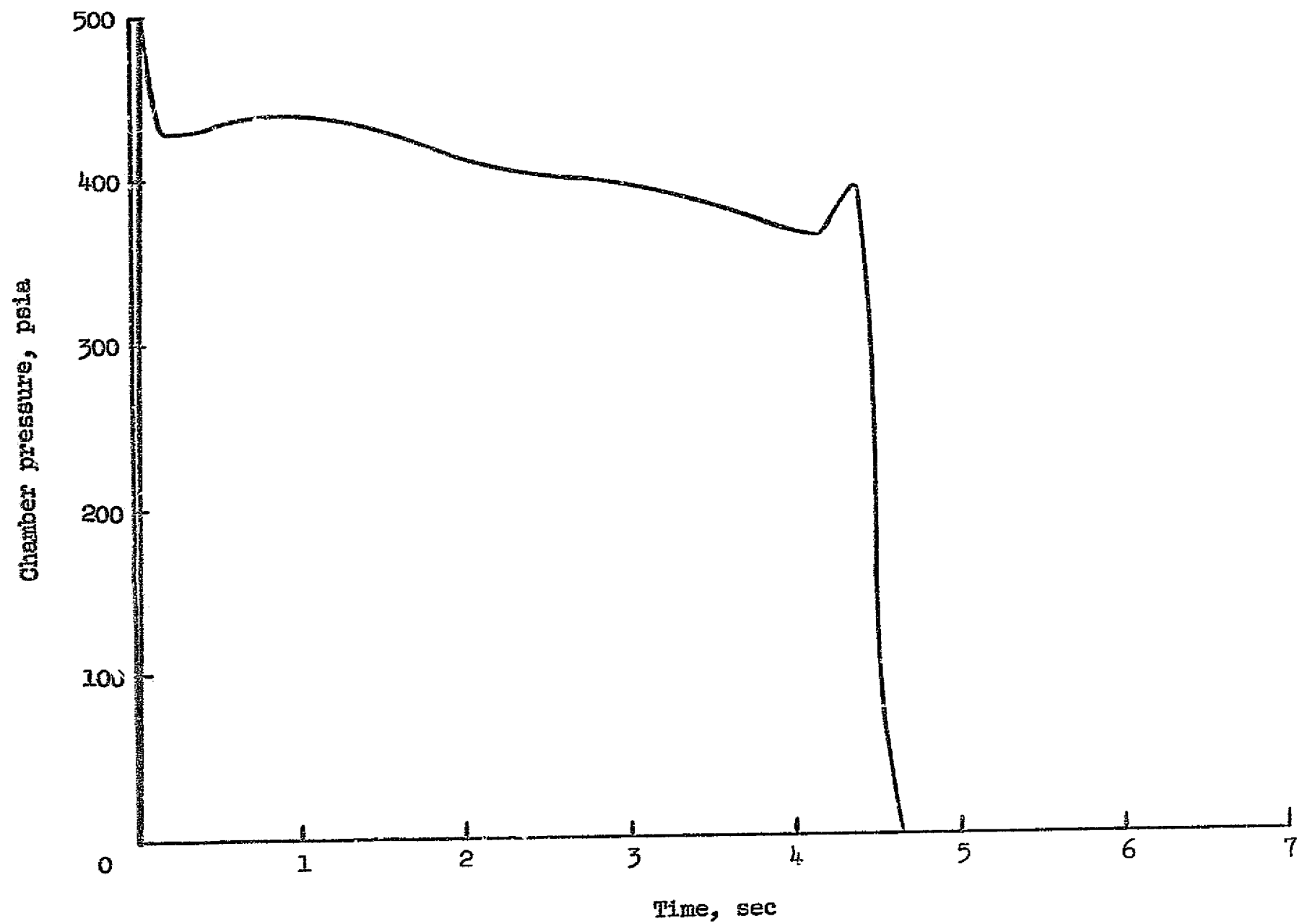


Figure 5. Chamber pressure vs time - $P_{avg} = 410$ psia

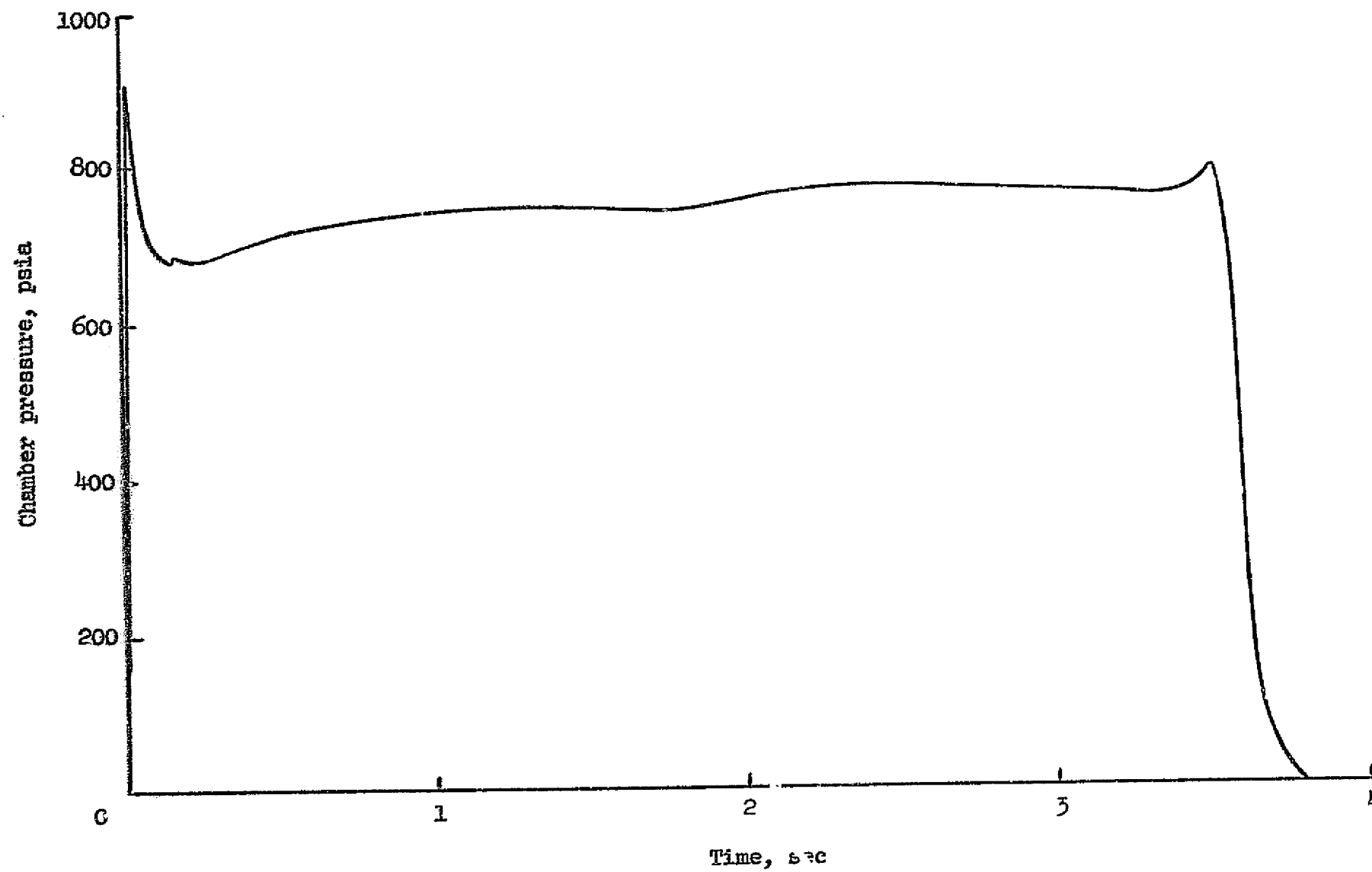


Figure 6. Chamber pressure vs time - $P_{avg} = 742$ psia

Local to Throat Diameter Ratio			
Chamber Pressure	Calorimeter		
	Corv	Throat	Div
220	1.338	1.0	1.538
410	1.338	1.0	1.538
742	1.437	1.0	1.900

Chamber Pressure	Throat Diameter, in.
220	1.25
410	1.25
742	0.868

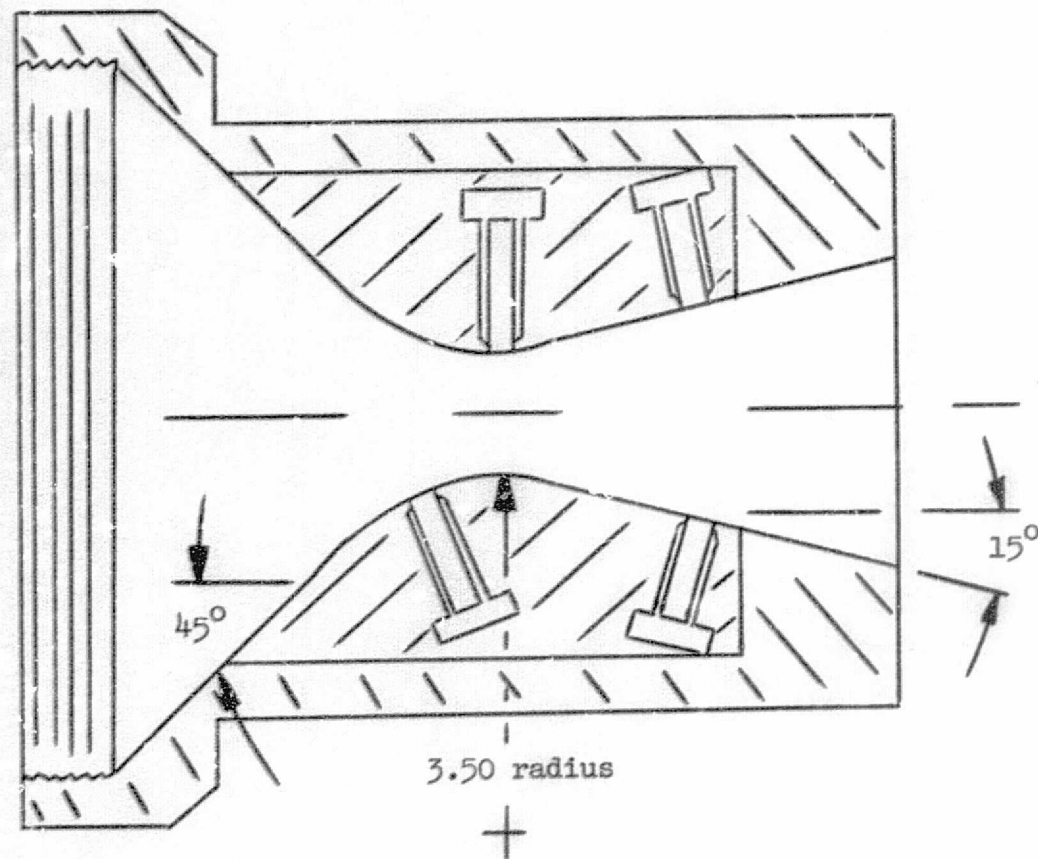
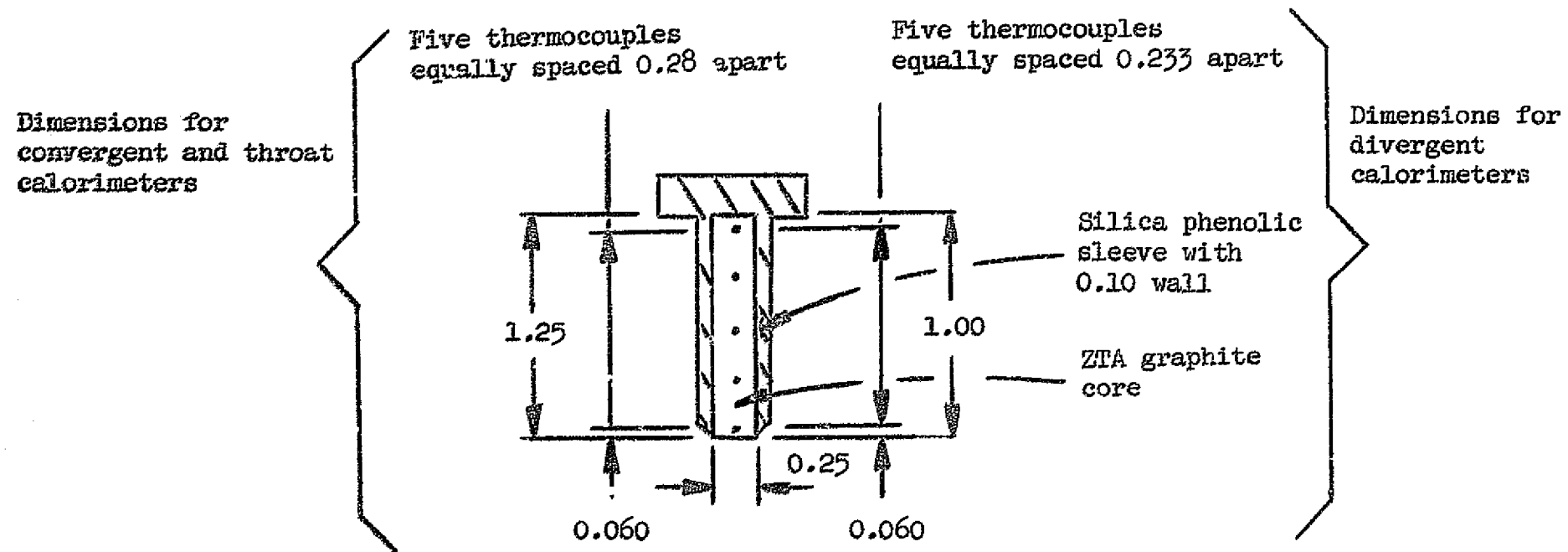


Figure 7. Calorimeter locations within nozzle

Note: All thermocouples were located on graphite core centerline



All dimensions in inches

Figure 8. Calorimeter dimensions

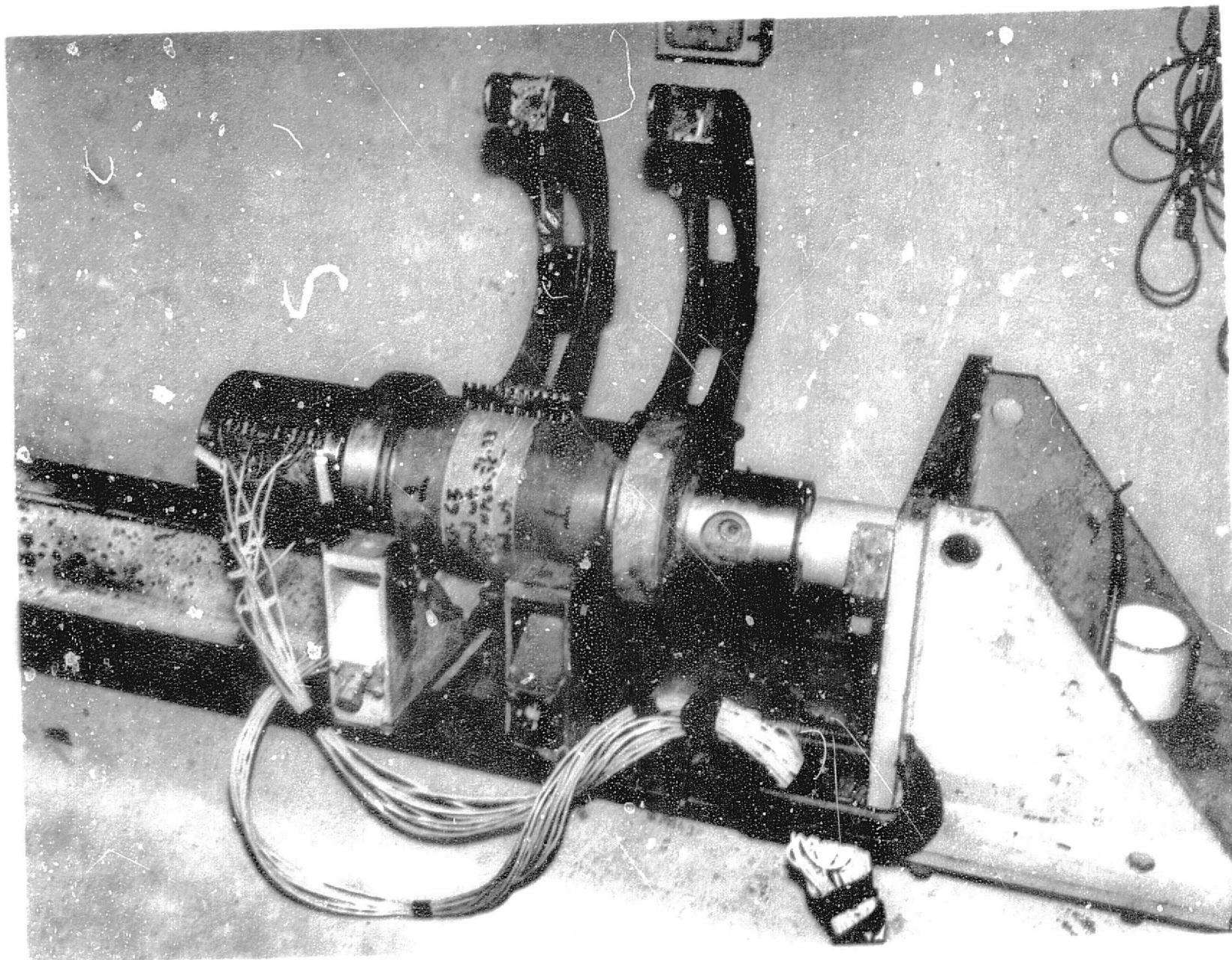


Figure 9. Experimental solid-propellant motor mounted in thrust stand

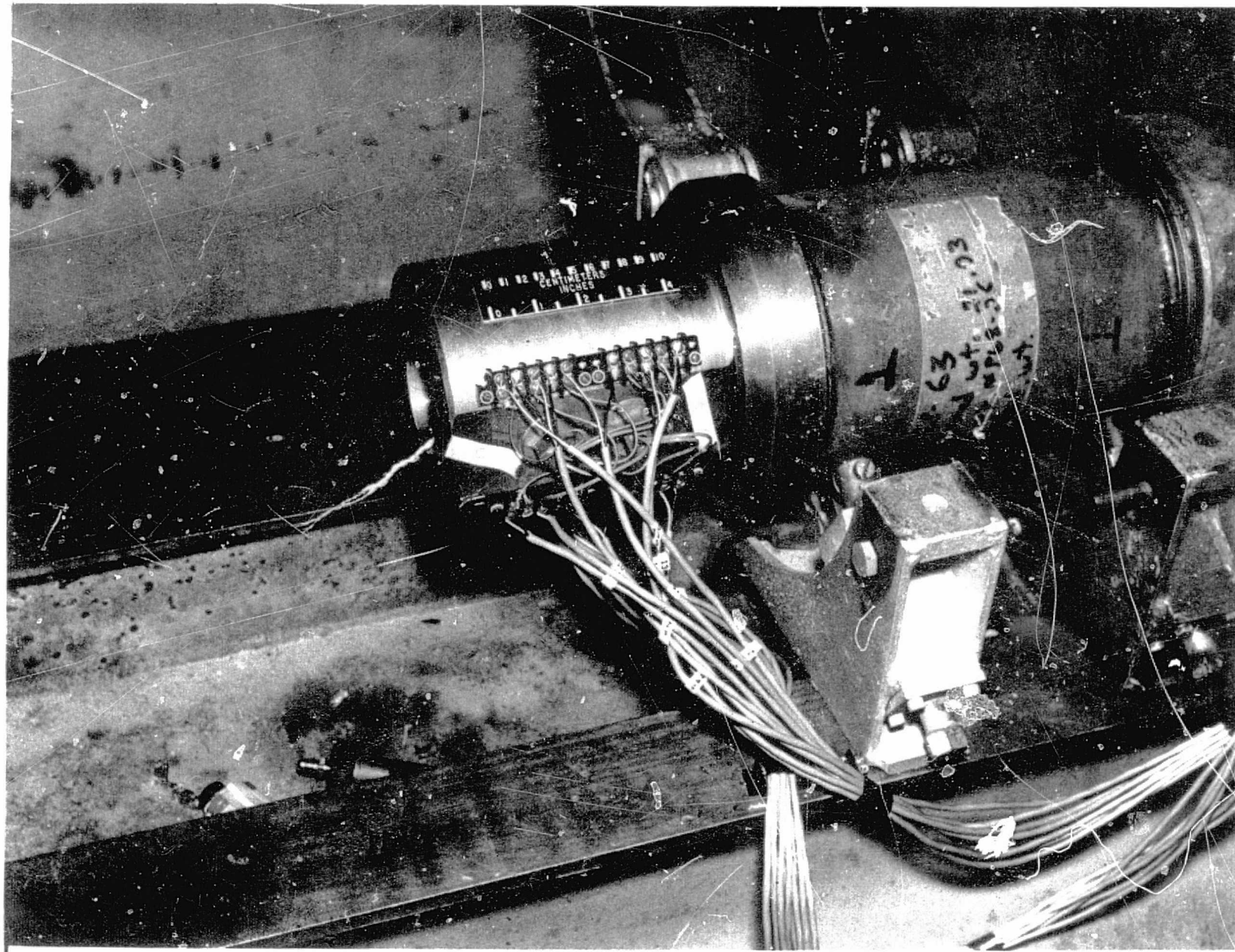


Figure 10. Instrumented nozzle on experimental solid-propellant motor

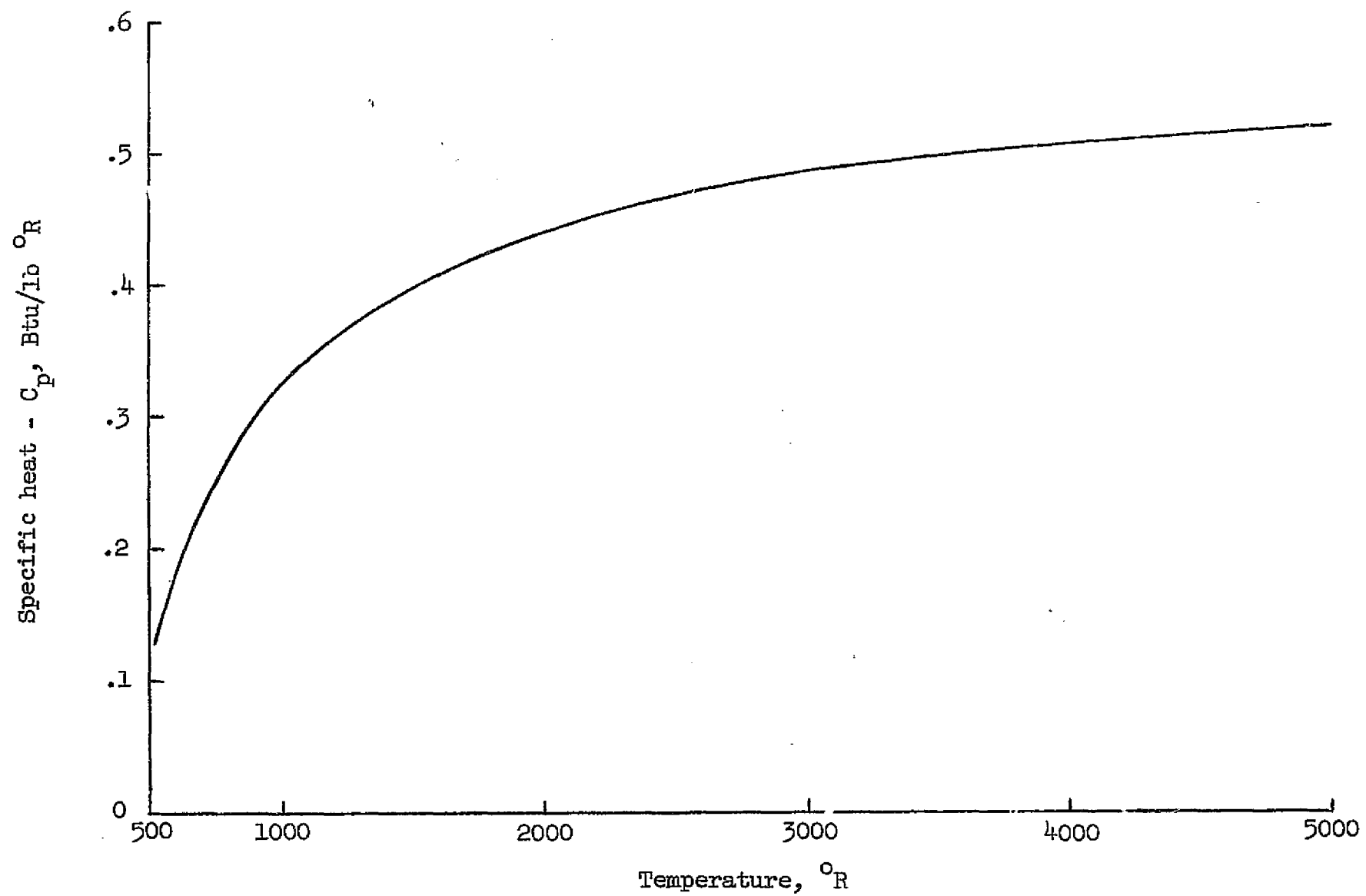


Figure 11. Specific heat - C_p vs temperature of ZTA graphite whose density is 119.3 lb/ft³

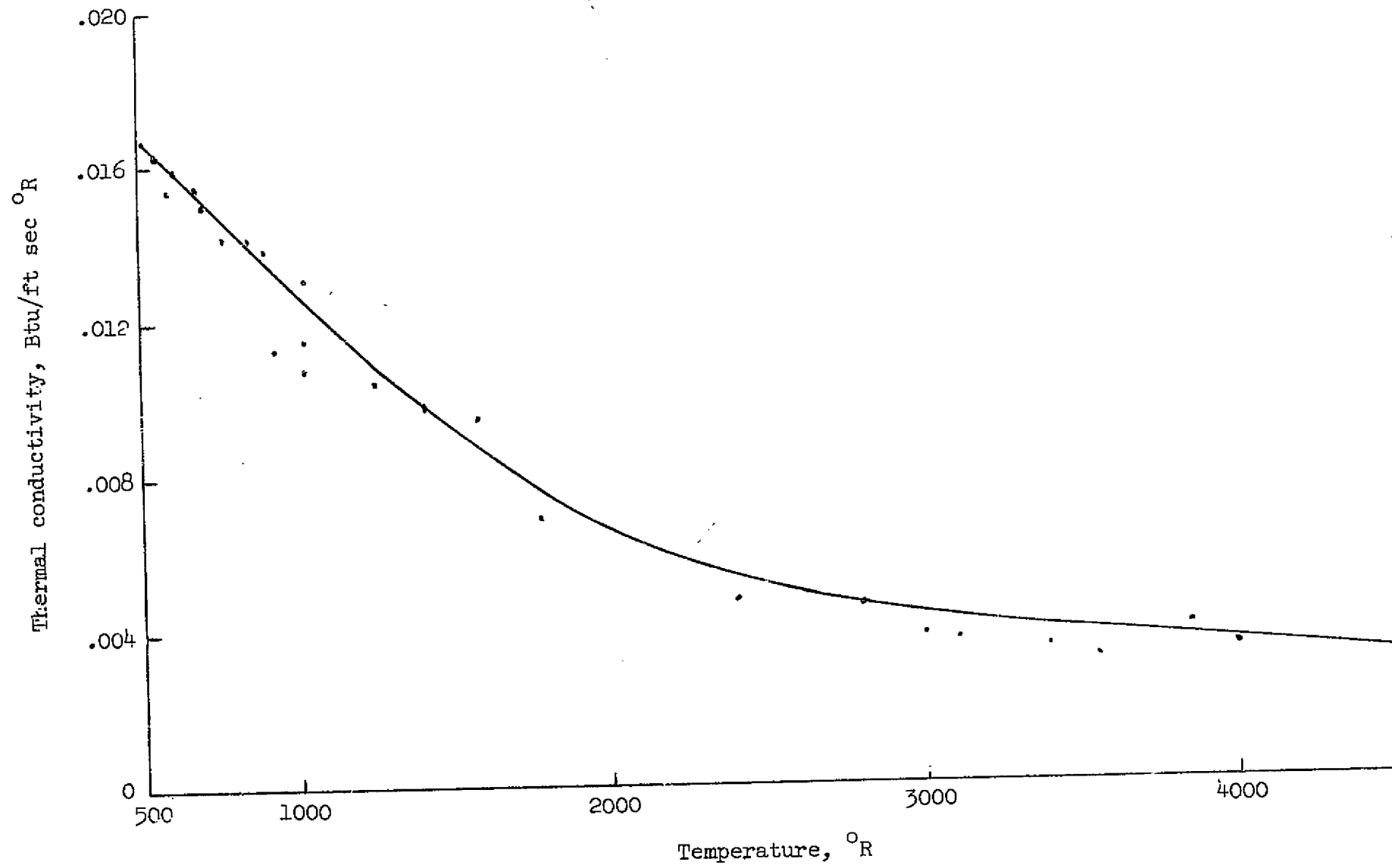
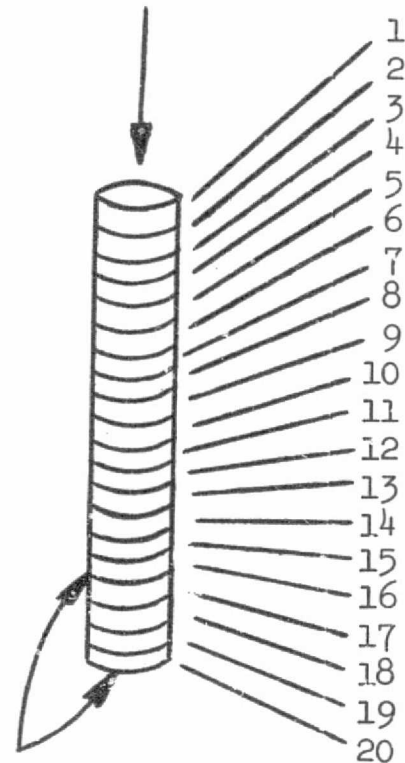


Figure 12. Thermal conductivity vs temperature of ZTA graphite whose density is 119.3 lb/ft³

Convergent and throat
calorimeters

Element	Thickness, in.
1	.0210
2	.0210
3	.0360
4	.0475
5	.0625
6	.0625
7	.0625
8	.0625
9	.0625
10	.0625
11	.0625
12	.0310
13	.0625
14	.0940
15	.0625
16	.0625
17	.0625
18	.1040
19	.1040
20	.1040

Heat in



Side and end
perfectly insulated

Divergent
calorimeters

Element	Thickness, in.
1	.0210
2	.0210
3	.0360
4	.0475
5	.0625
6	.0625
7	.0860
8	.0388
9	.0625
10	.0625
11	.0625
12	.0625
13	.0625
14	.0625
15	.0625
16	.0625
17	.0625
18	.0314
19	.0314
20	.0314

Figure 13. ZTA graphite core finite elements

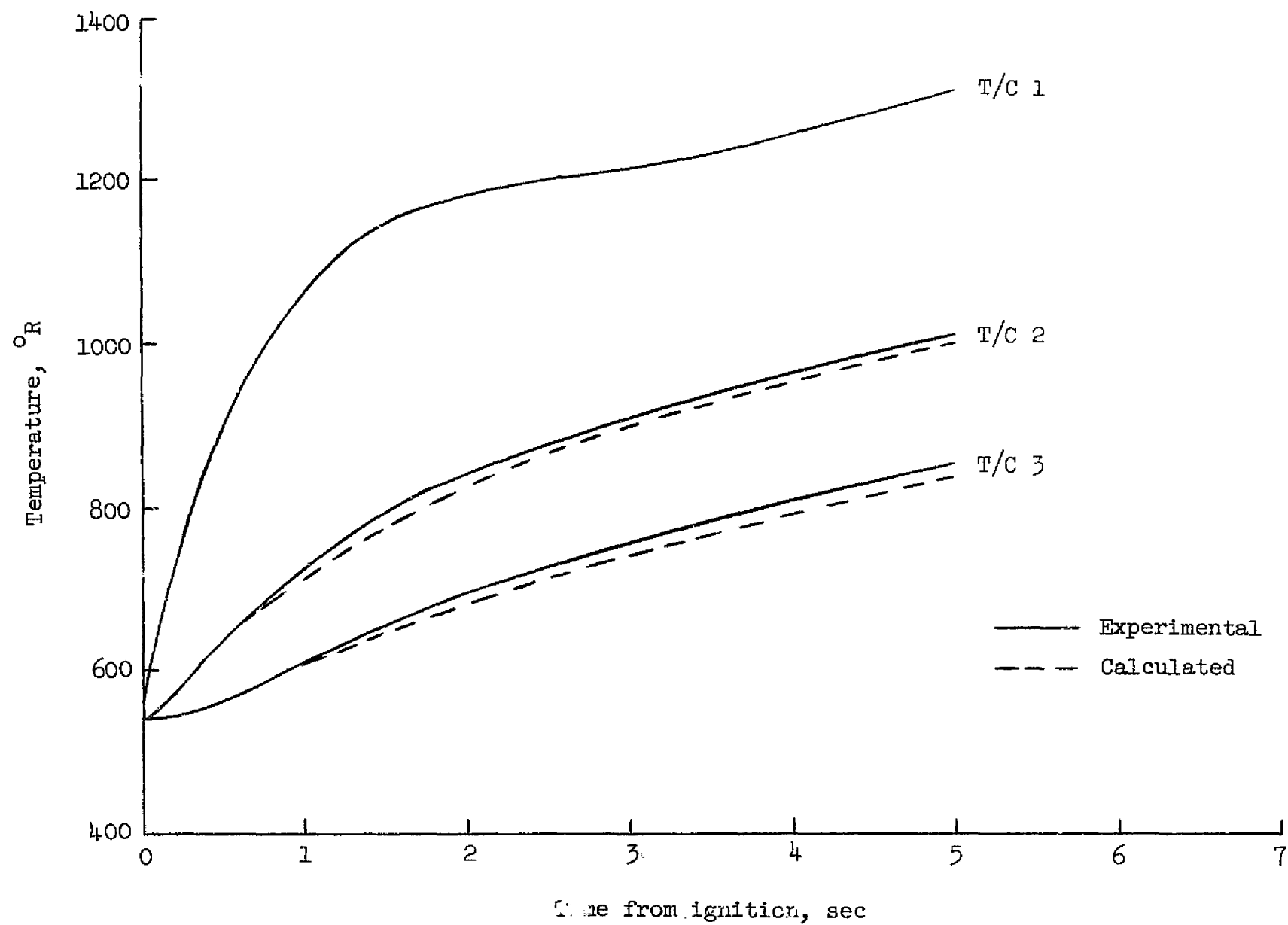


Figure 14. Comparison of experimental and calculated temperature response of thermocouples 1, 2, and 3. Convergent calorimeter - $P_c = 220$ psia

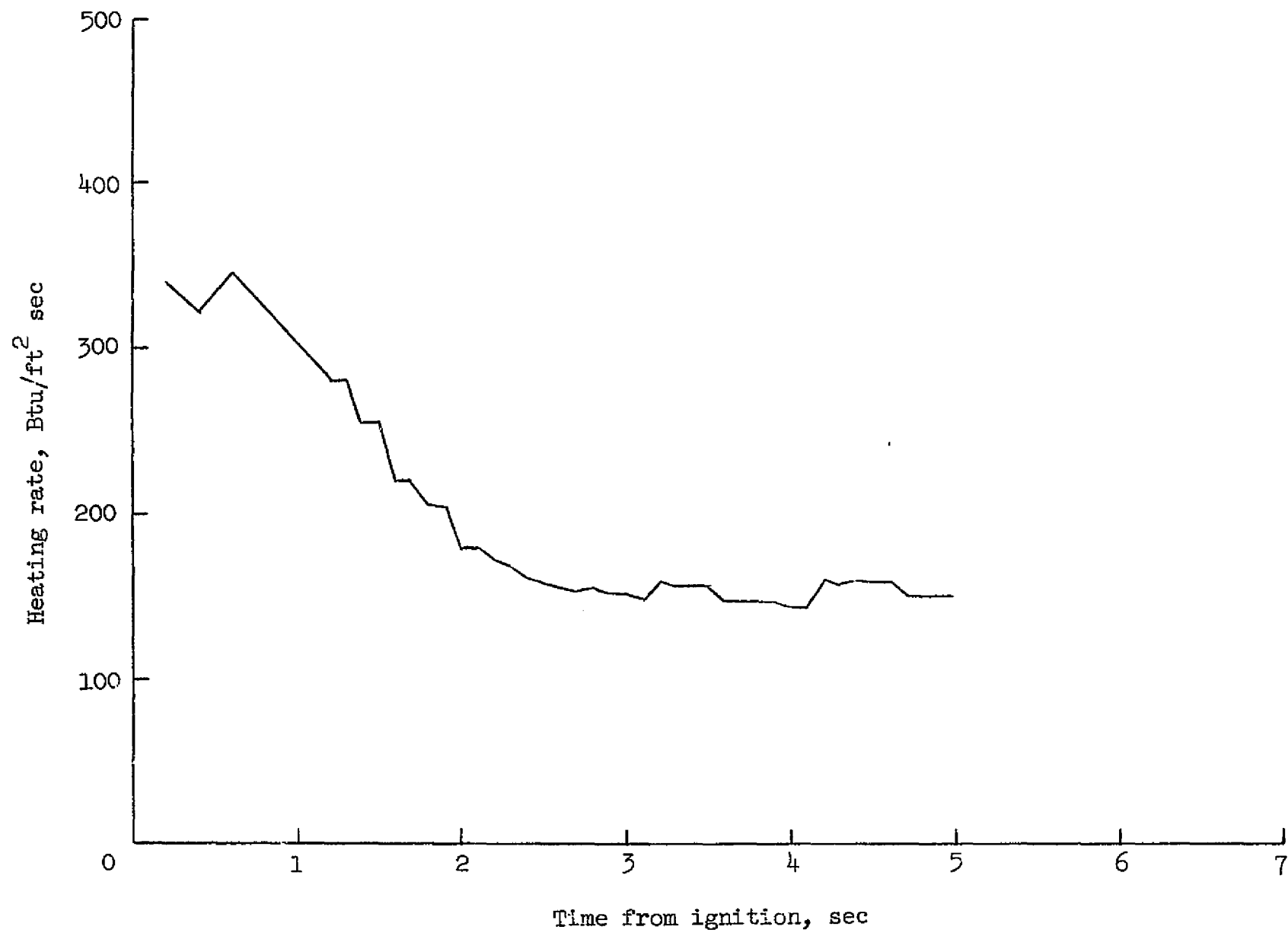


Figure 15. Heating rate vs burn time. Convergent calorimeter - $P_c = 220$ psia

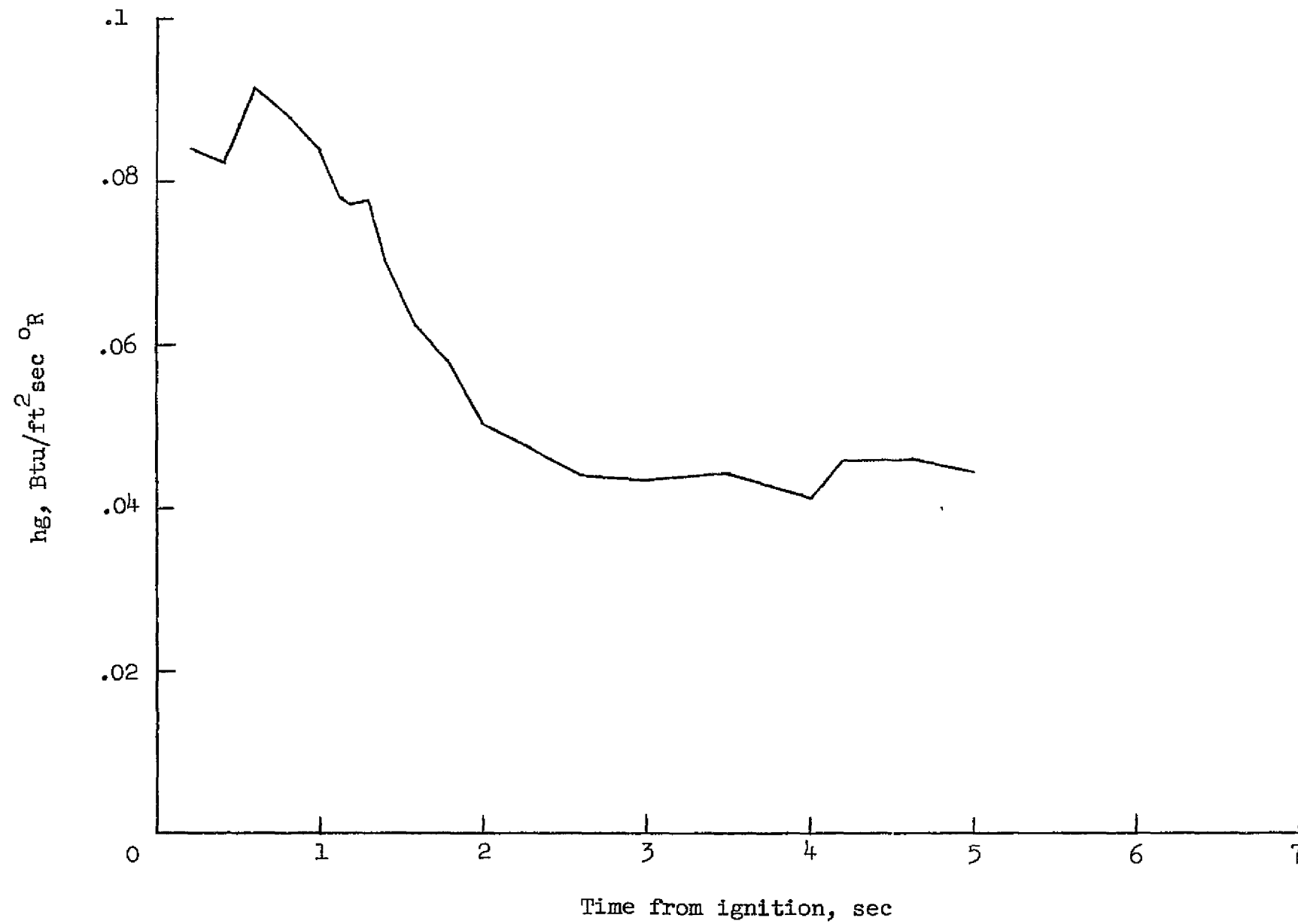


Figure 16. Convective heat-transfer coefficient vs burn time. Convergent calorimeter - $P_c = 220$ psia

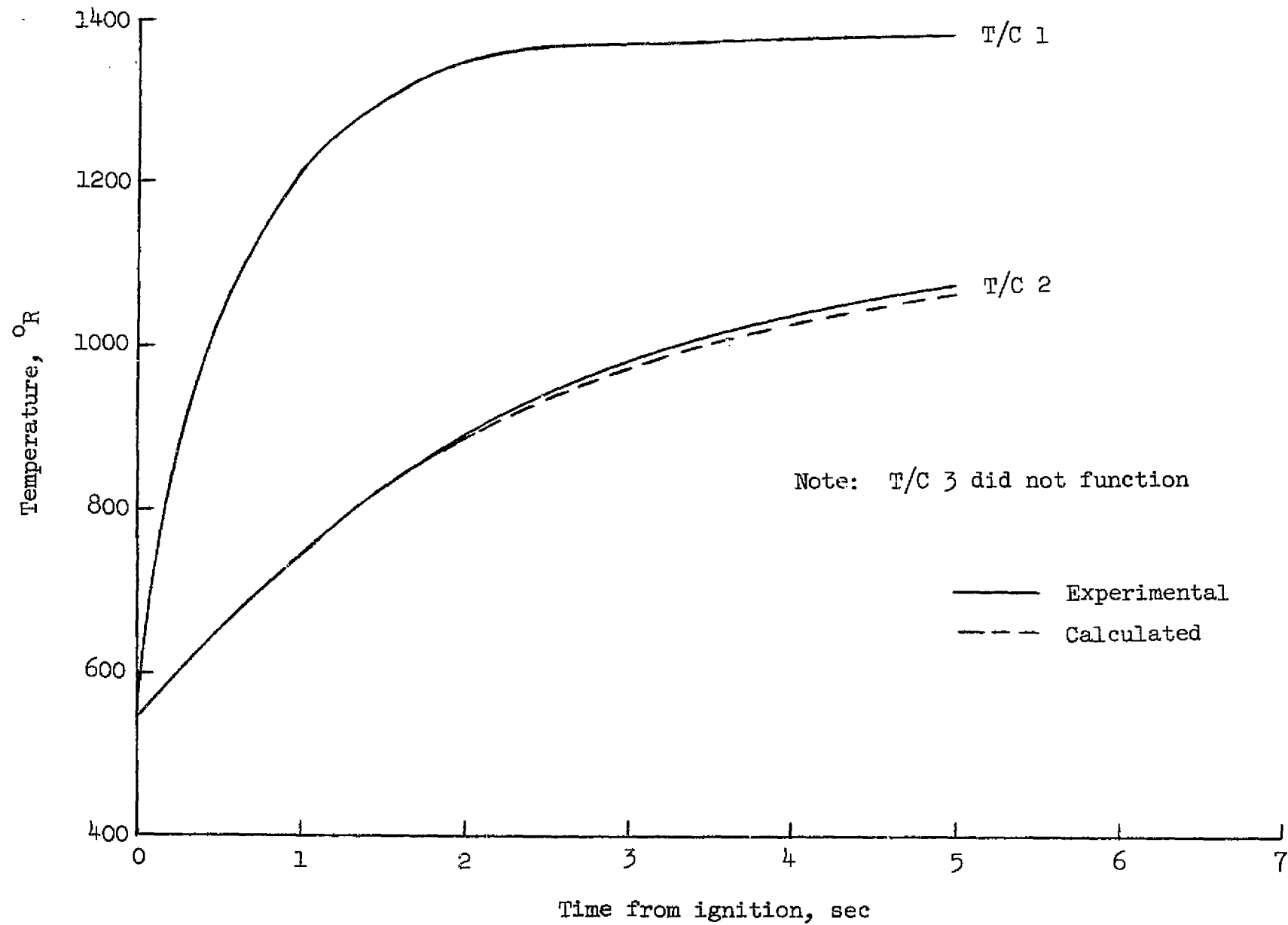


Figure 17. Comparison of experimental and calculated temperature response of thermocouples 1 and 2. Throat calorimeter - $P_c = 220$ psia

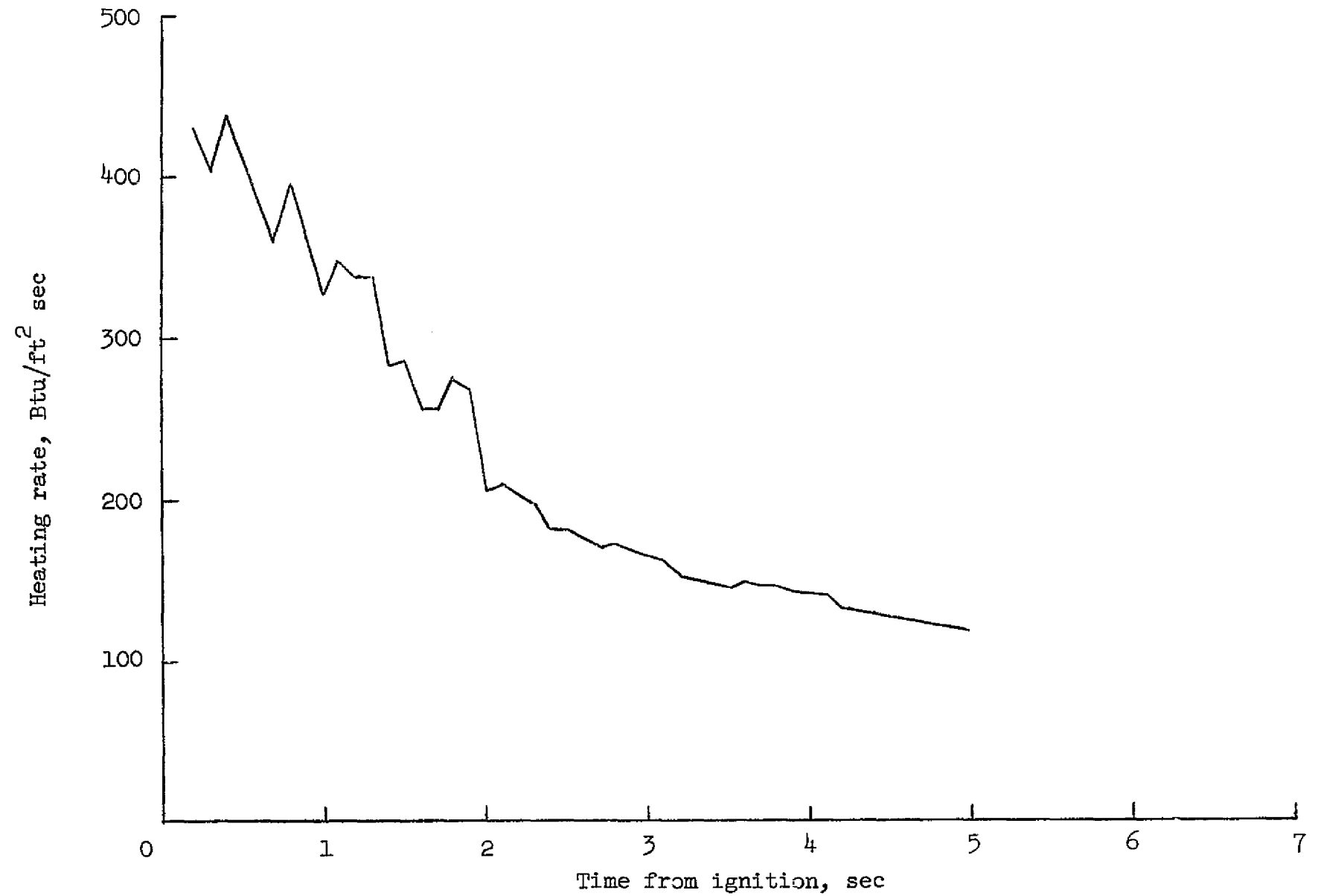


Figure 18. Heating rate vs burn time. Throat calorimeter - $P_c = 220$ psia

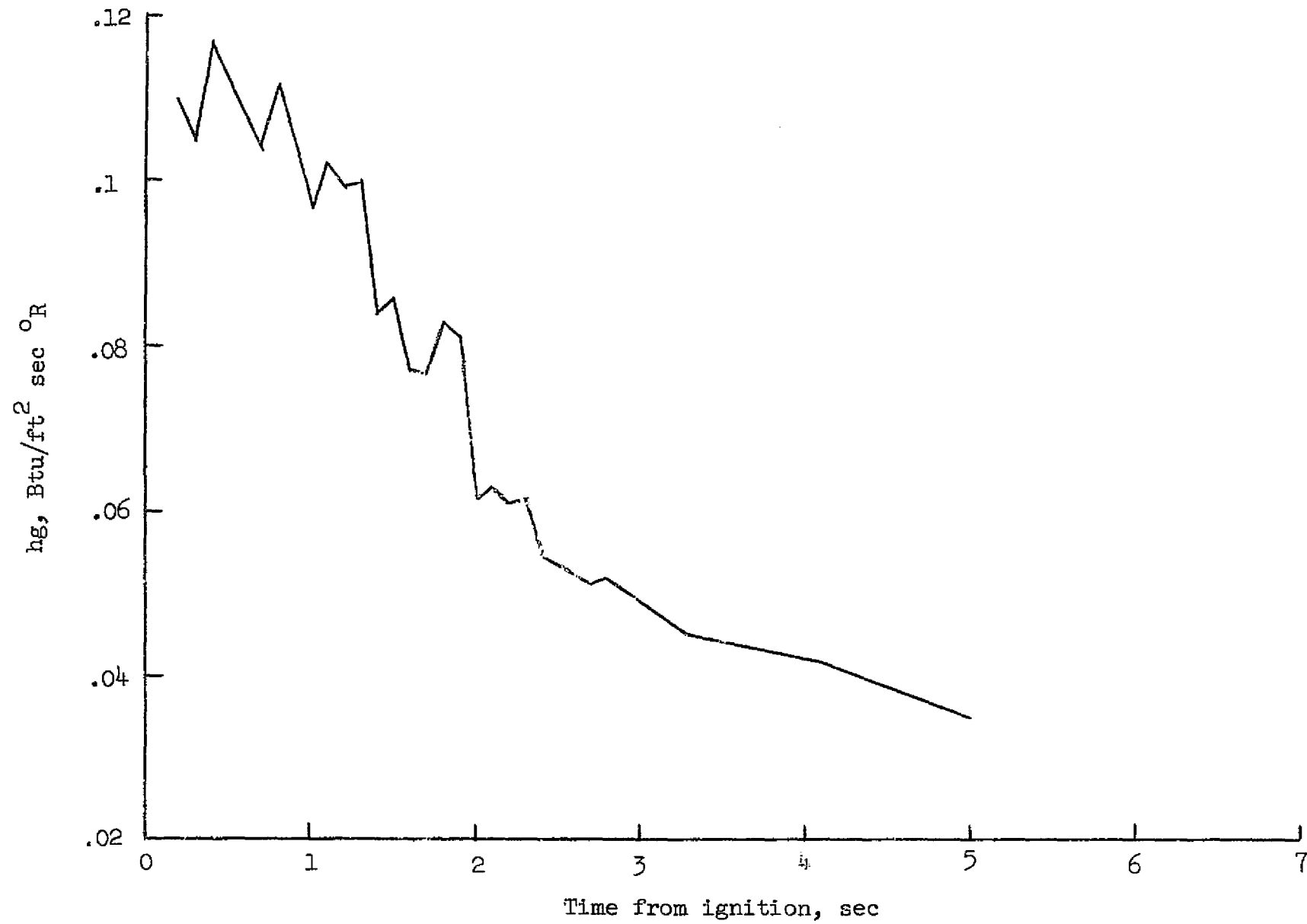


Figure 19. Convective heat-transfer coefficient vs burn time. Throat calorimeter -
 $P_c = 220$ psia

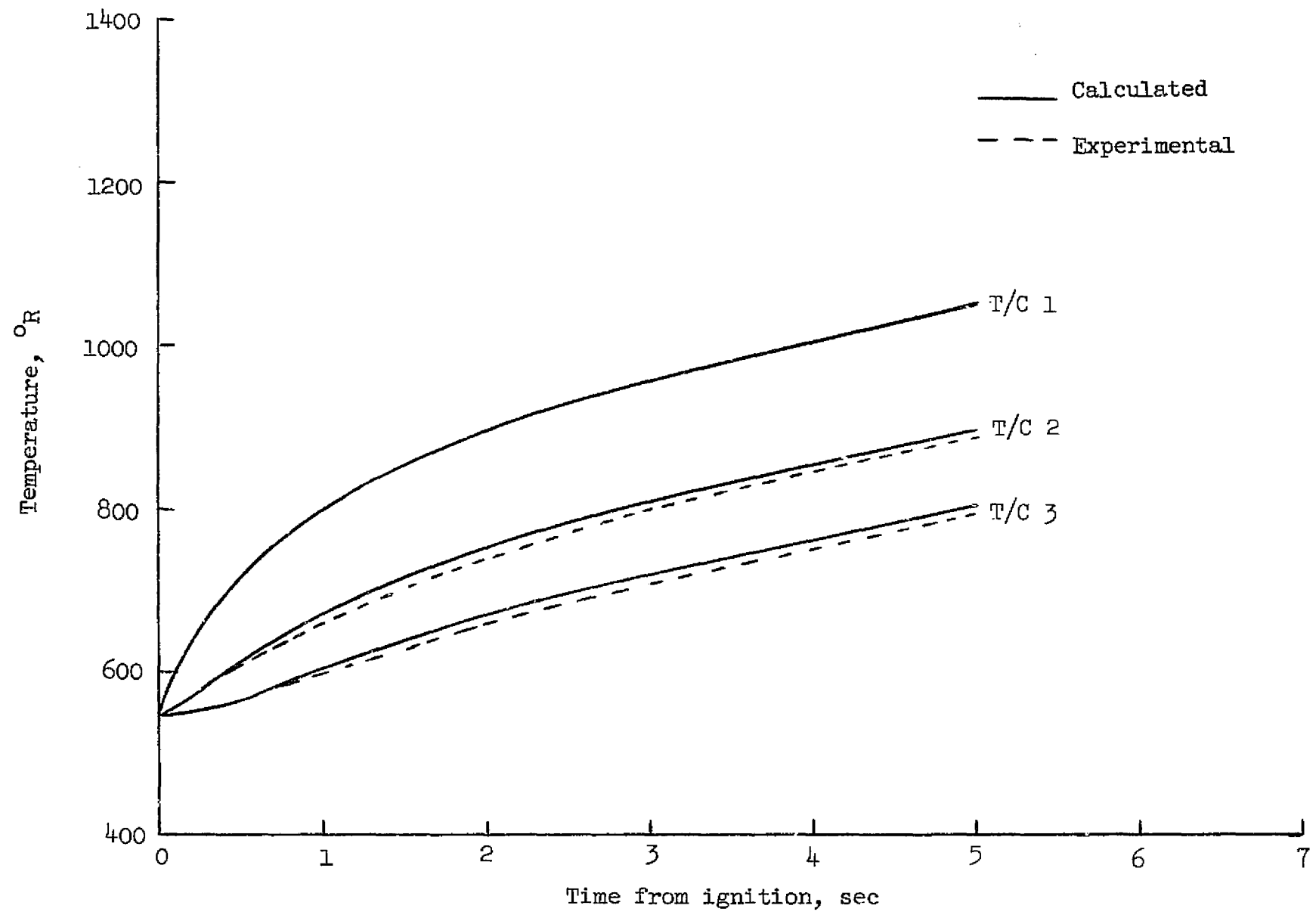


Figure 20. Comparison of experimental and calculated temperature response of thermocouples 1, 2, and 3. Divergent calorimeter - $P_c = 220$ psia

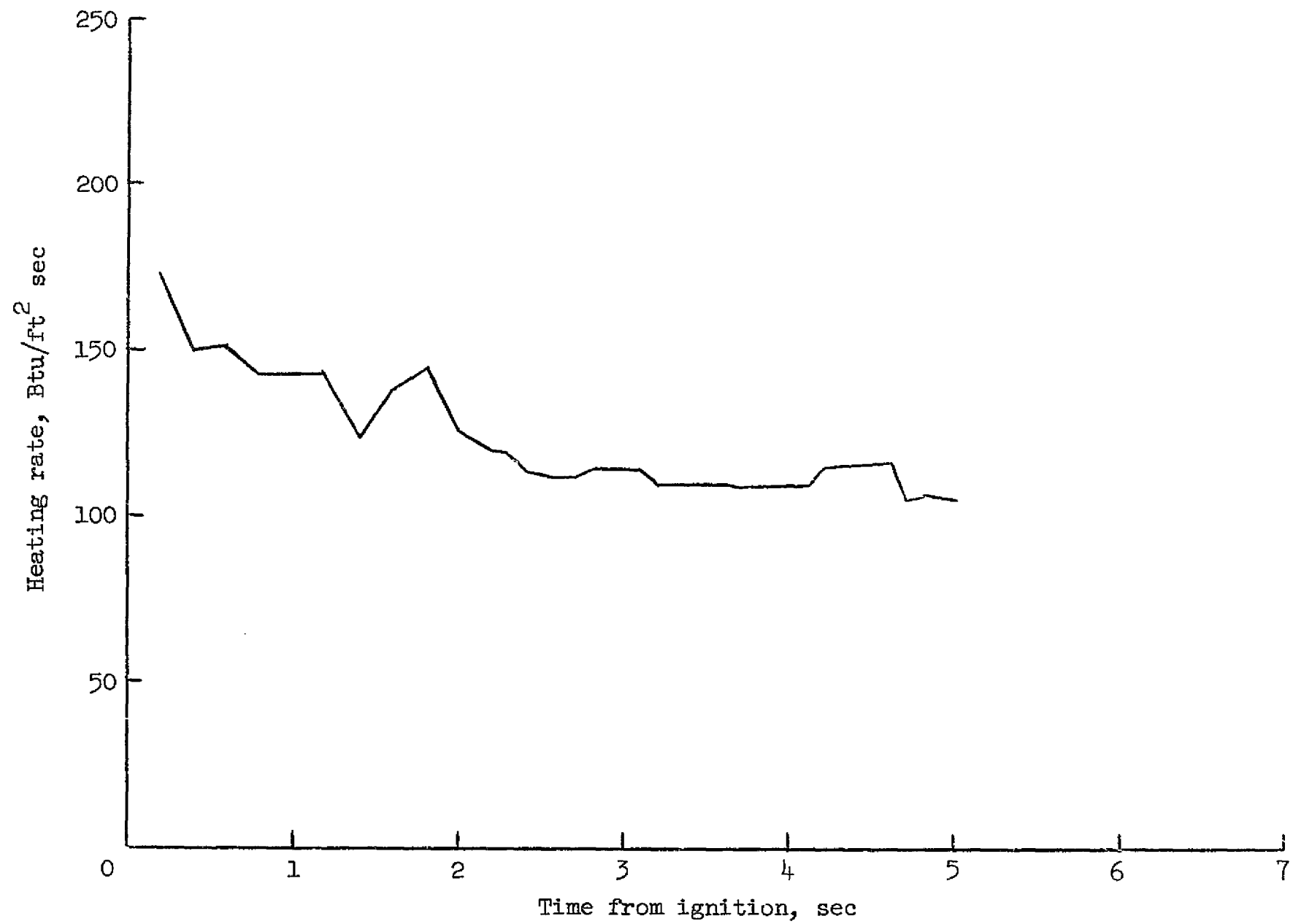


Figure 21. Heating rate vs burn time. Divergent calorimeter - $P_c = 220$ psia

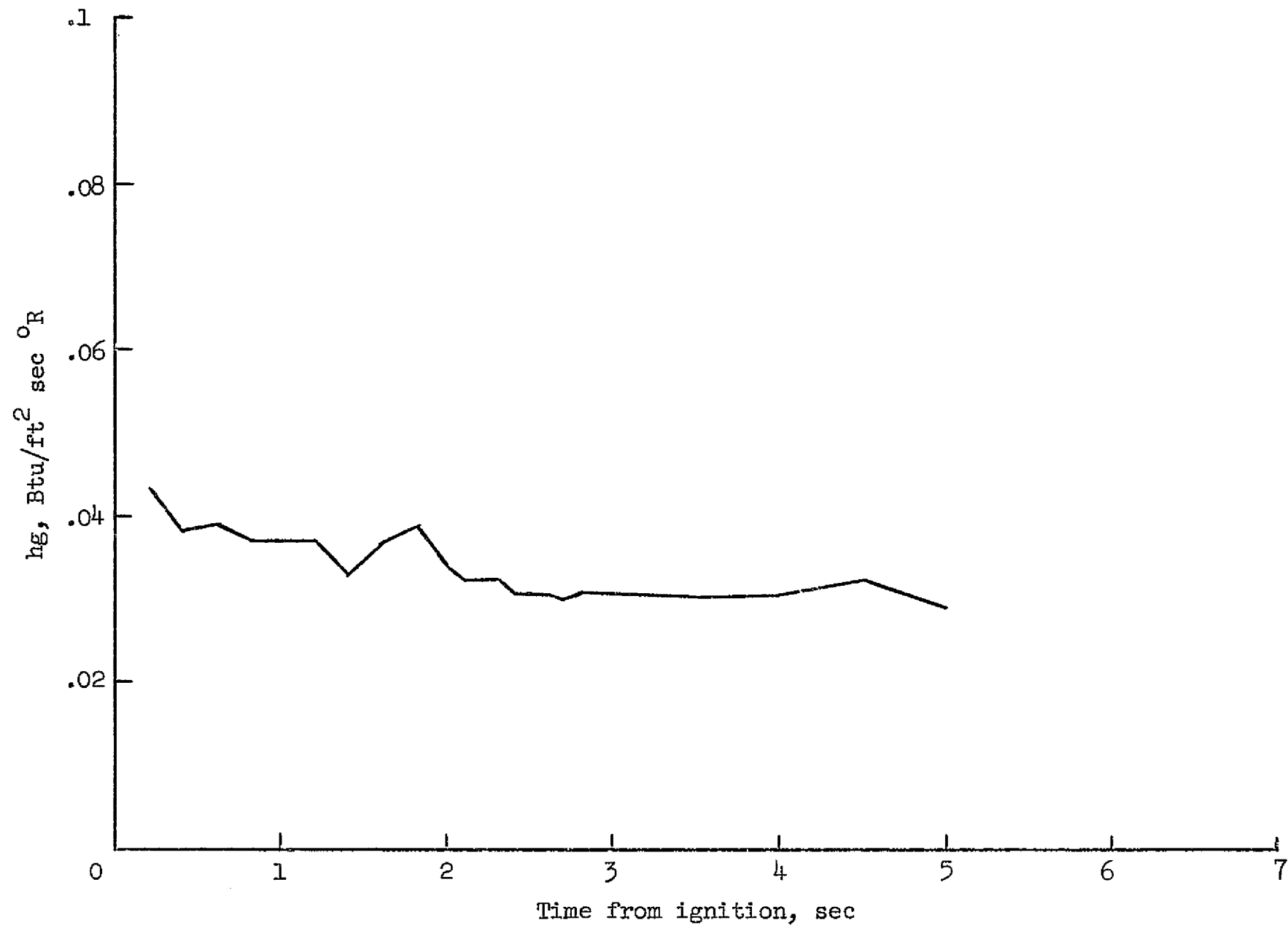


Figure 22. Convective heat-transfer coefficient vs burn time. Divergent calorimeter -
 $P_c = 220$ psia

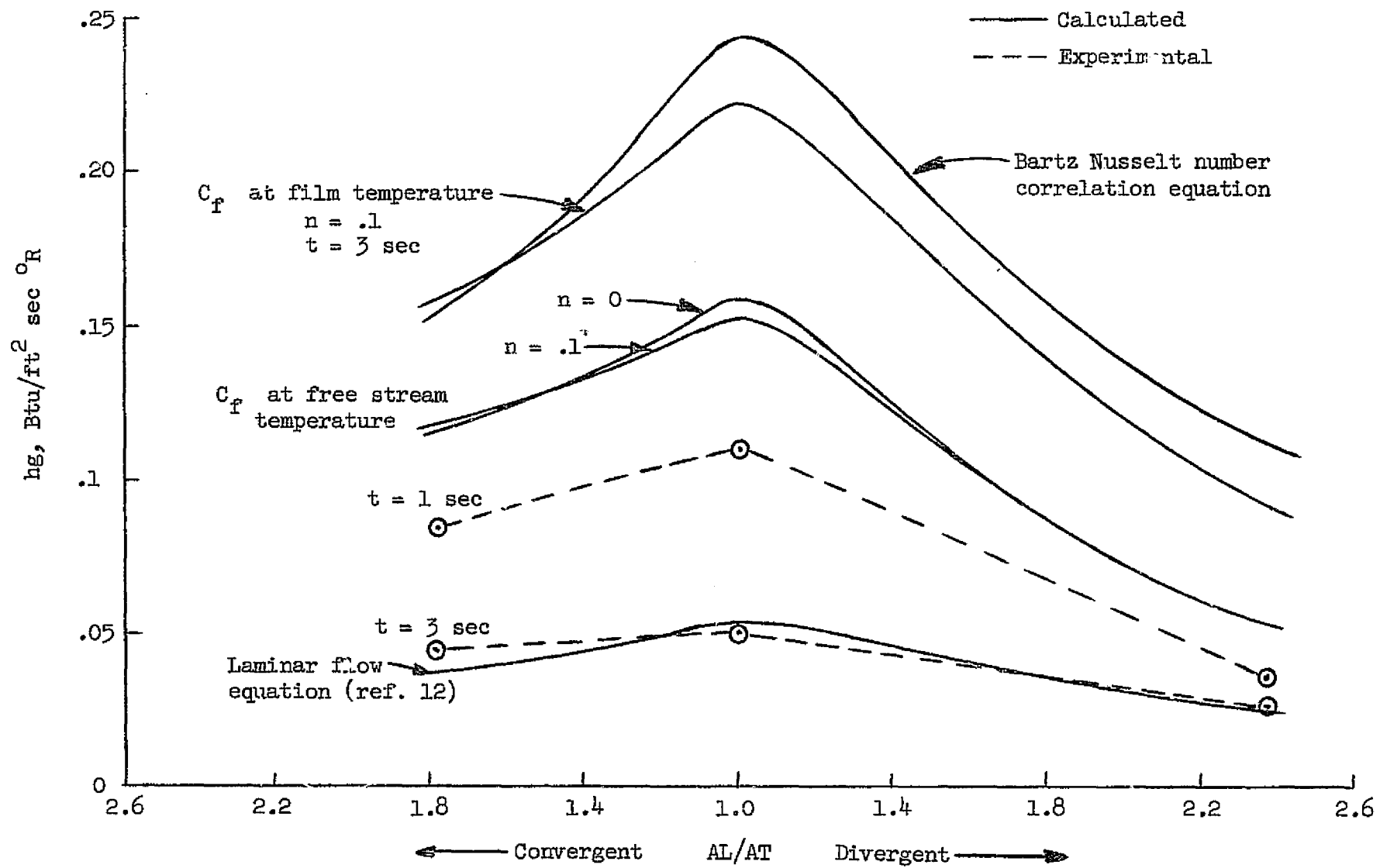


Figure 23. Comparison of analytical and experimental heat-transfer coefficients - $P_c = 220$ psia

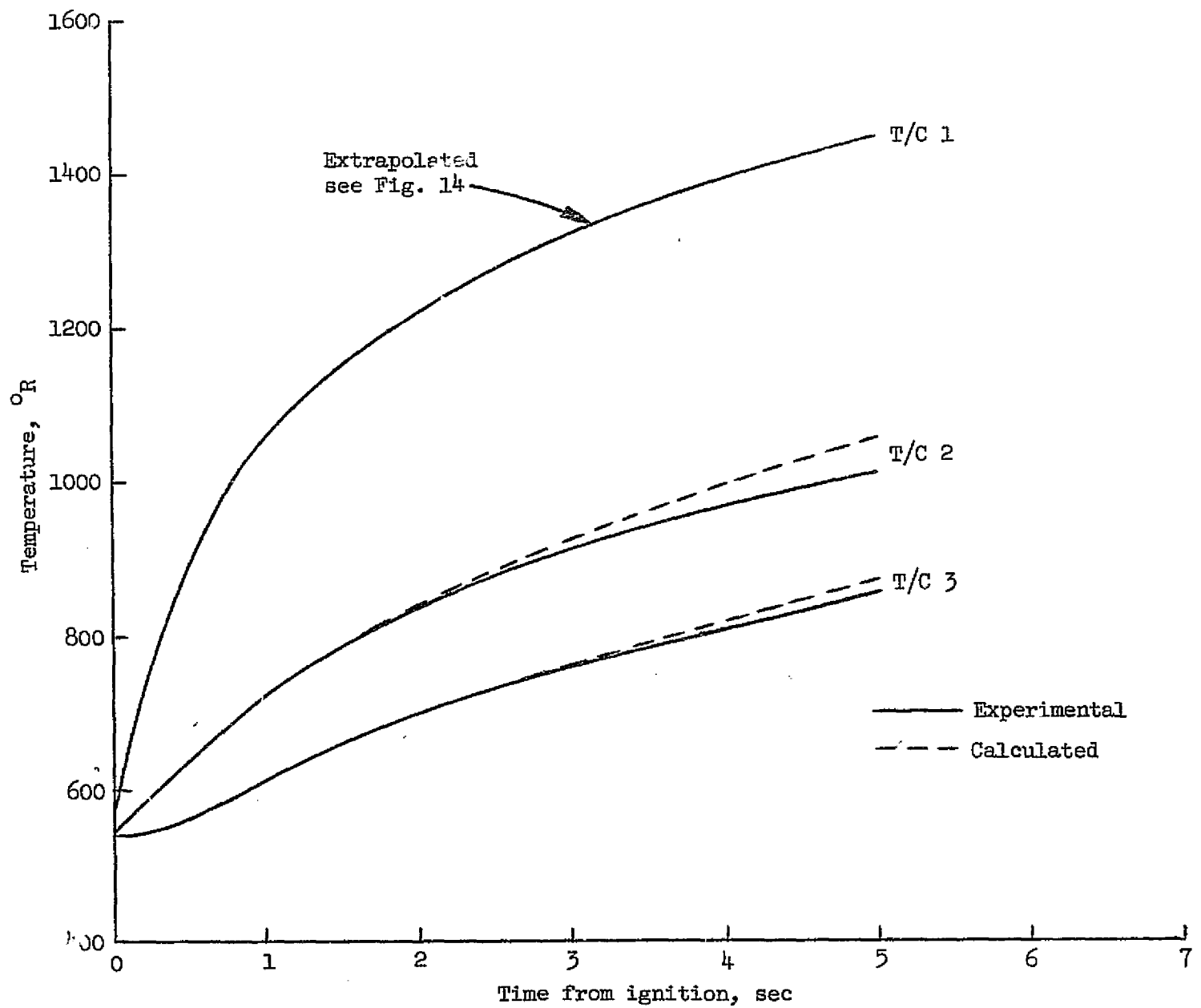


Figure 24. Extrapolated thermocouple number 1 response. Convergent calorimeter - $P_c = 220$ psia

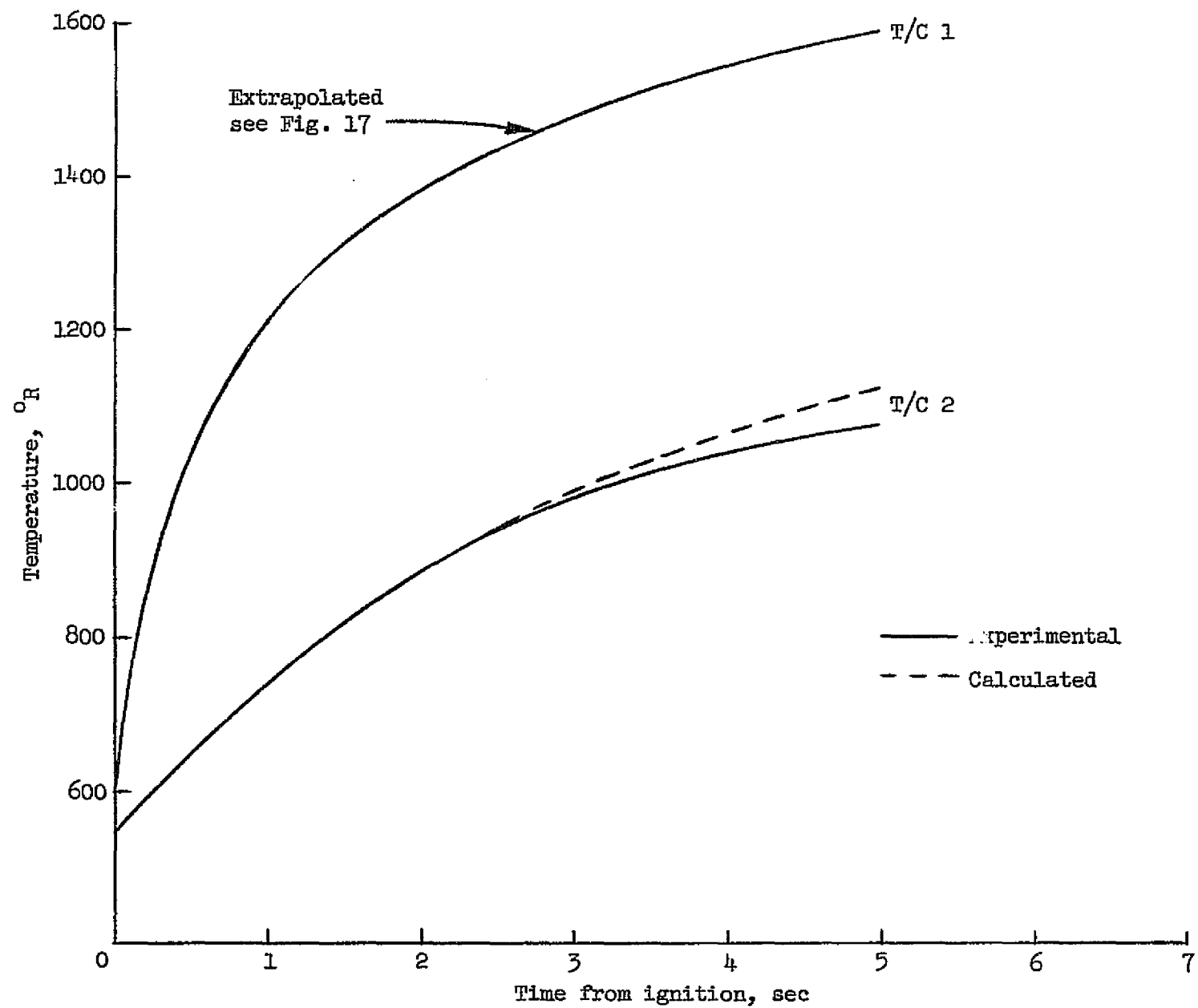


Figure 25. Extrapolated thermocouple number 1 response. Throat calorimeter - $P_c = 220$ psia

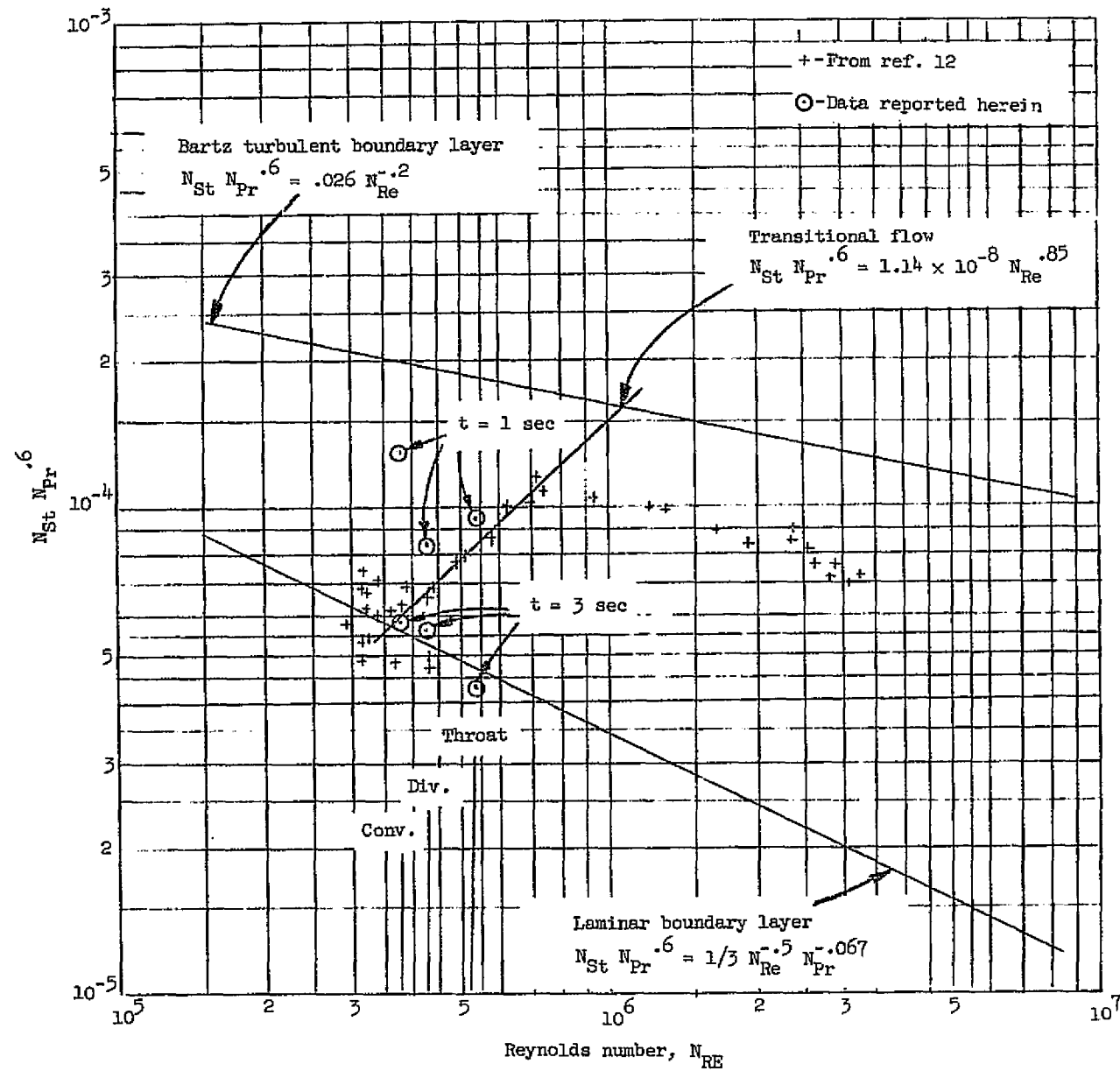


Figure 26. Dimensionless convective heat-transfer coefficient vs Reynolds number - $P_c = 220$ psia

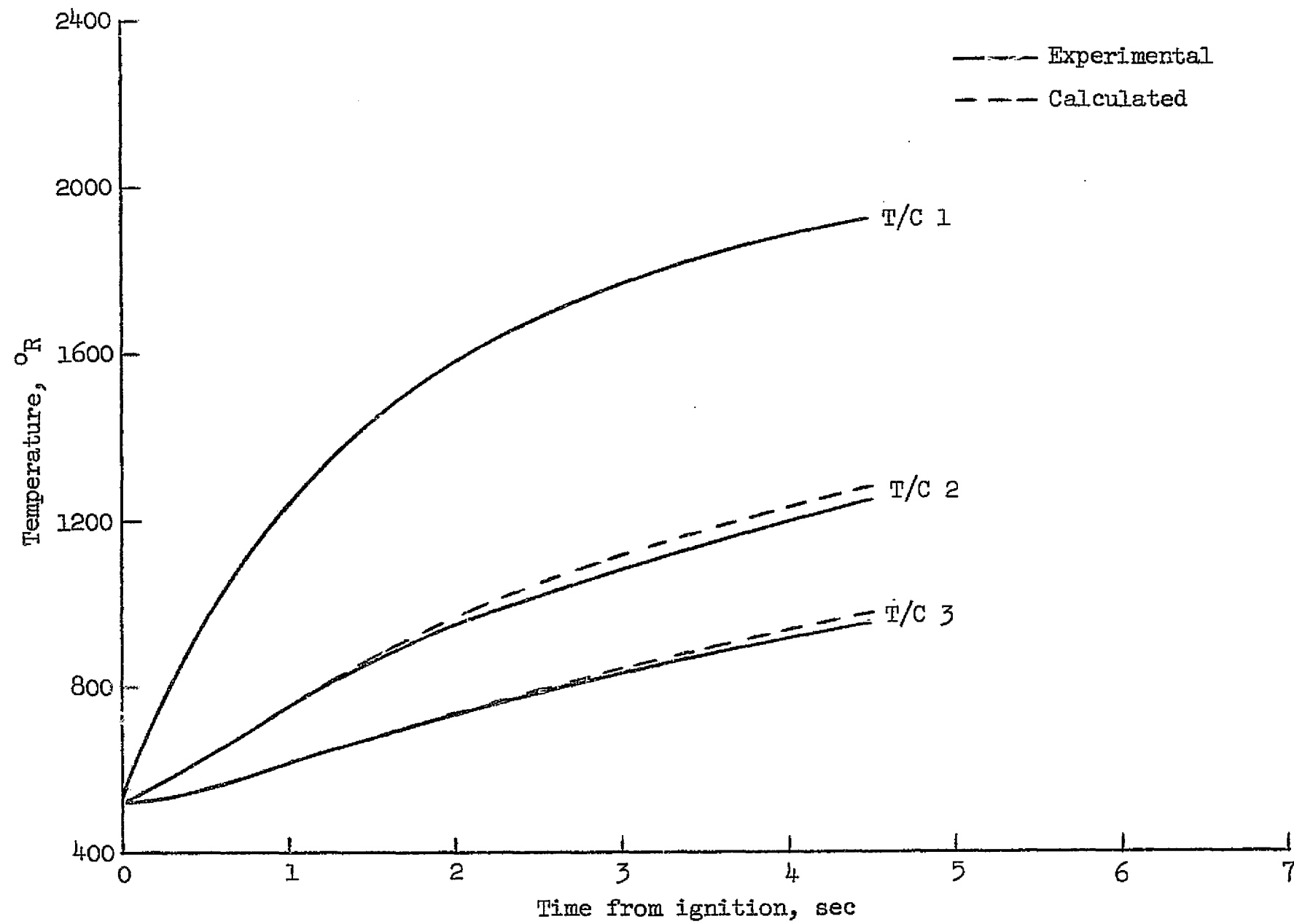


Figure 27. Comparison of experimental and calculated temperature response of thermocouples 1, 2, and 3. Convergent calorimeter - $P_c = 410$ psia

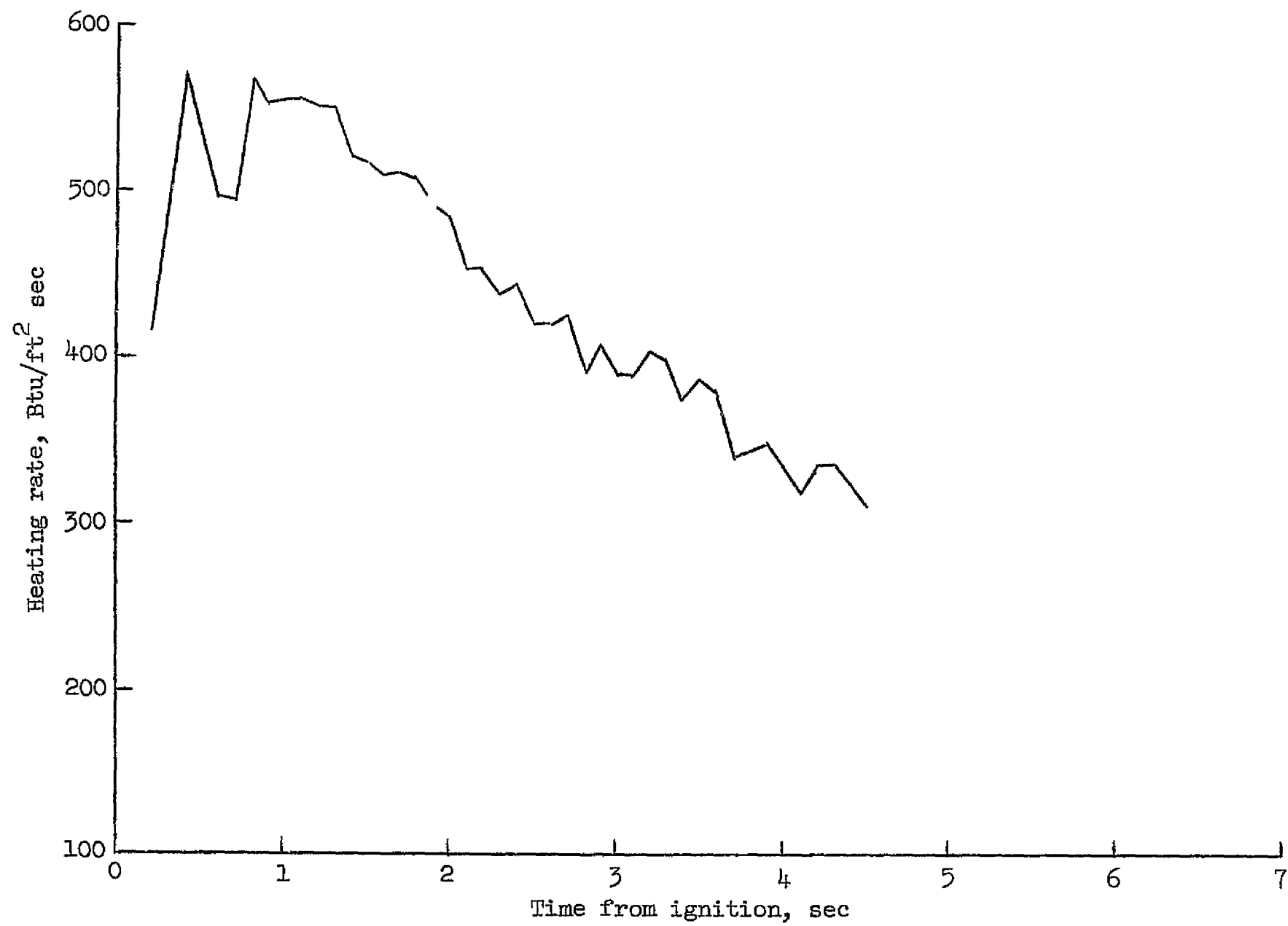


Figure 28. Heating rate vs burn time. Convergent calorimeter - $P_c = 410$ psia

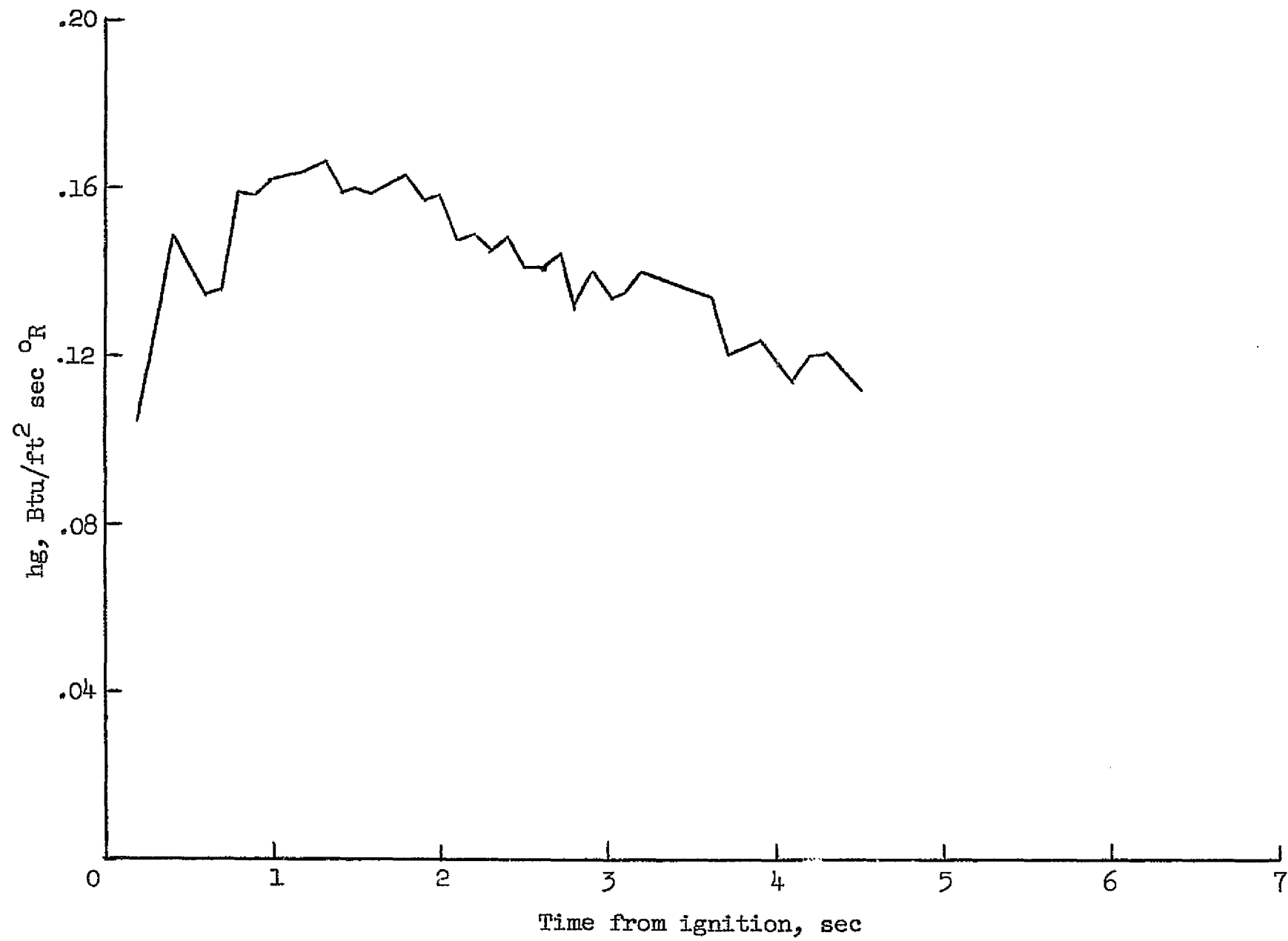


Figure 29. Convective heat-transfer coefficient vs burn time. Convergent calorimeter - $P_c = 410$ psia

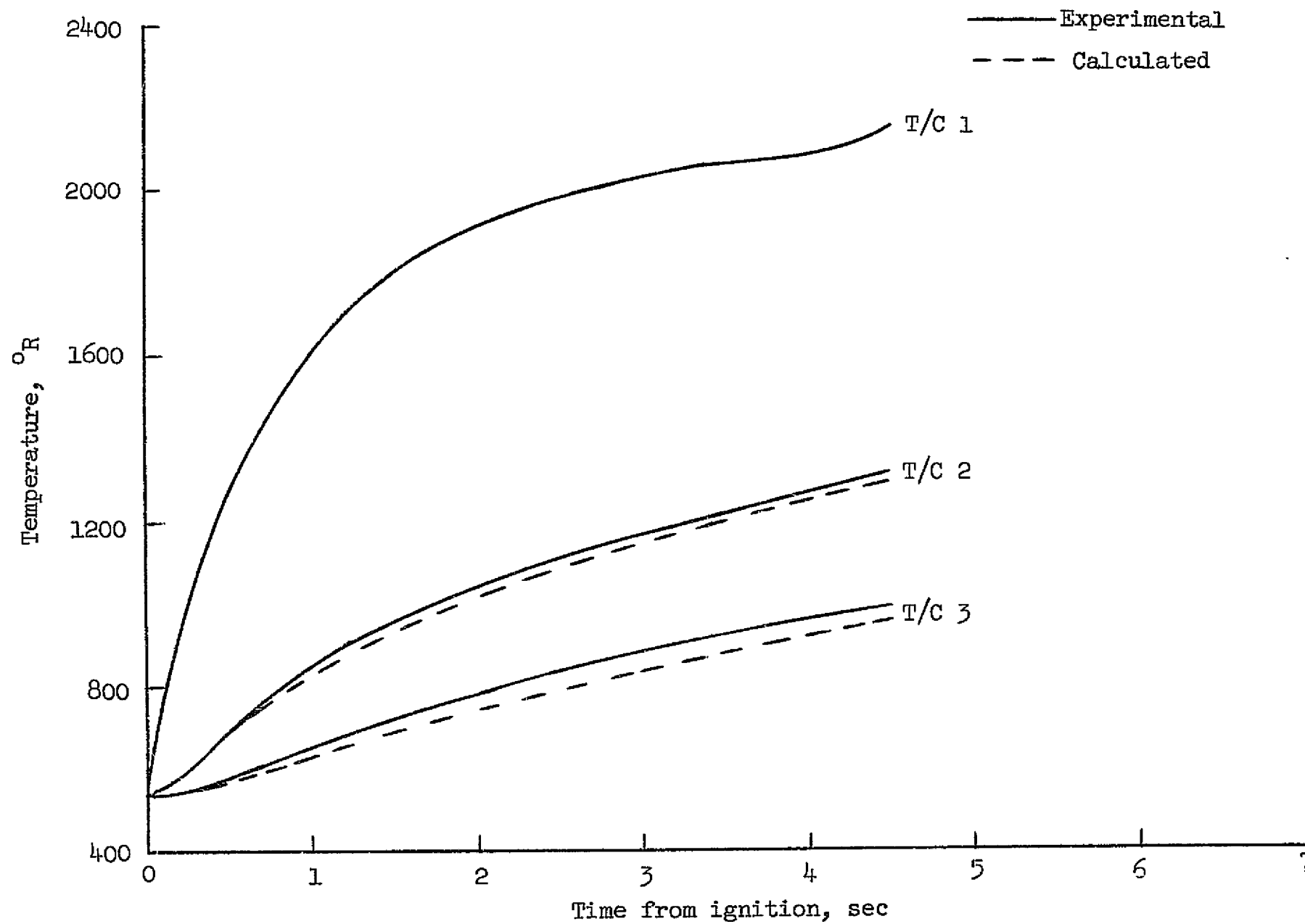


Figure 30. Comparison of experimental and calculated temperature response of thermocouples 1, 2, and 3. Throat calorimeter - $P_c = 410$ psia

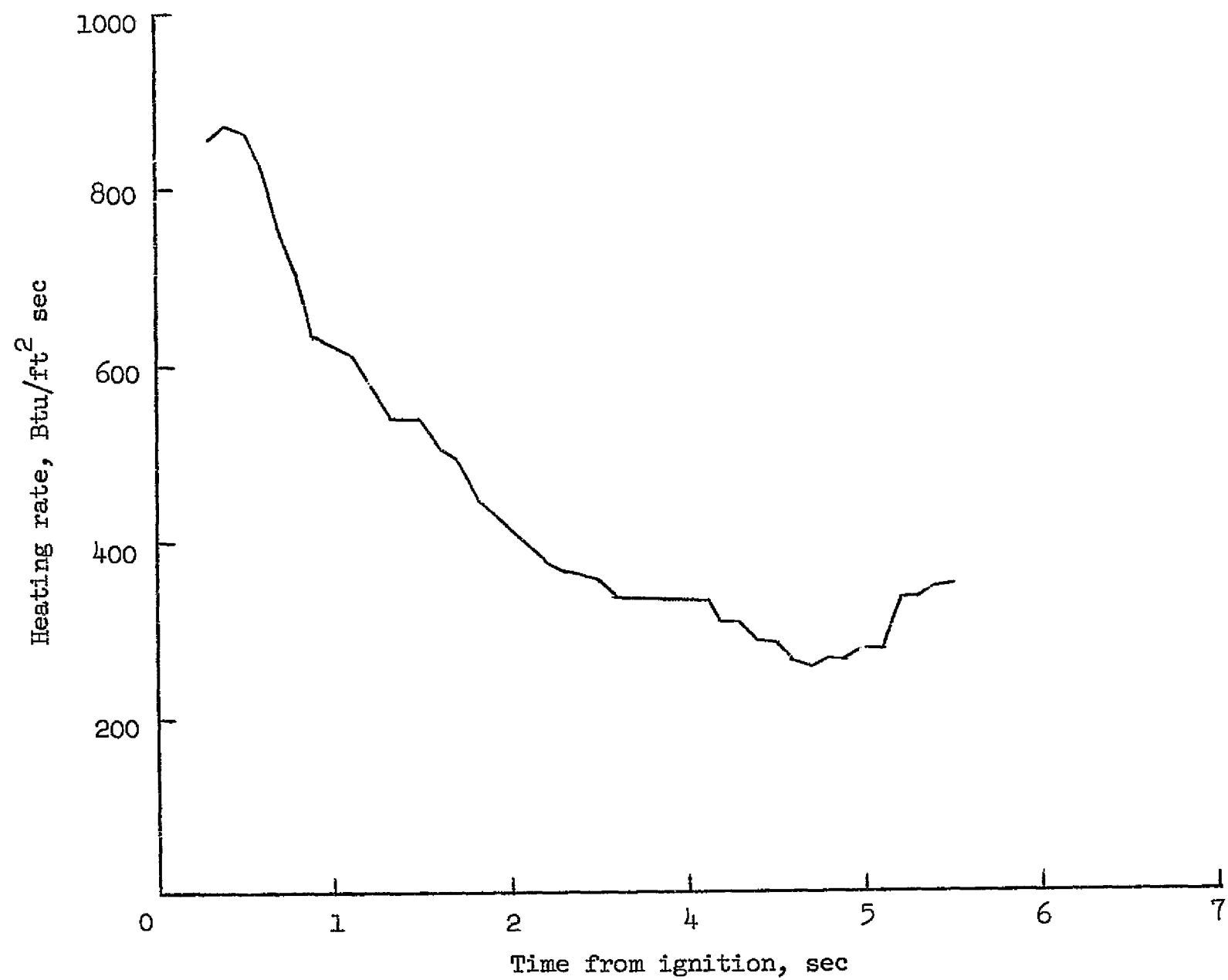


Figure 31. Heating rate vs burn time. Throat calorimeter - $P_c = 410$ psia

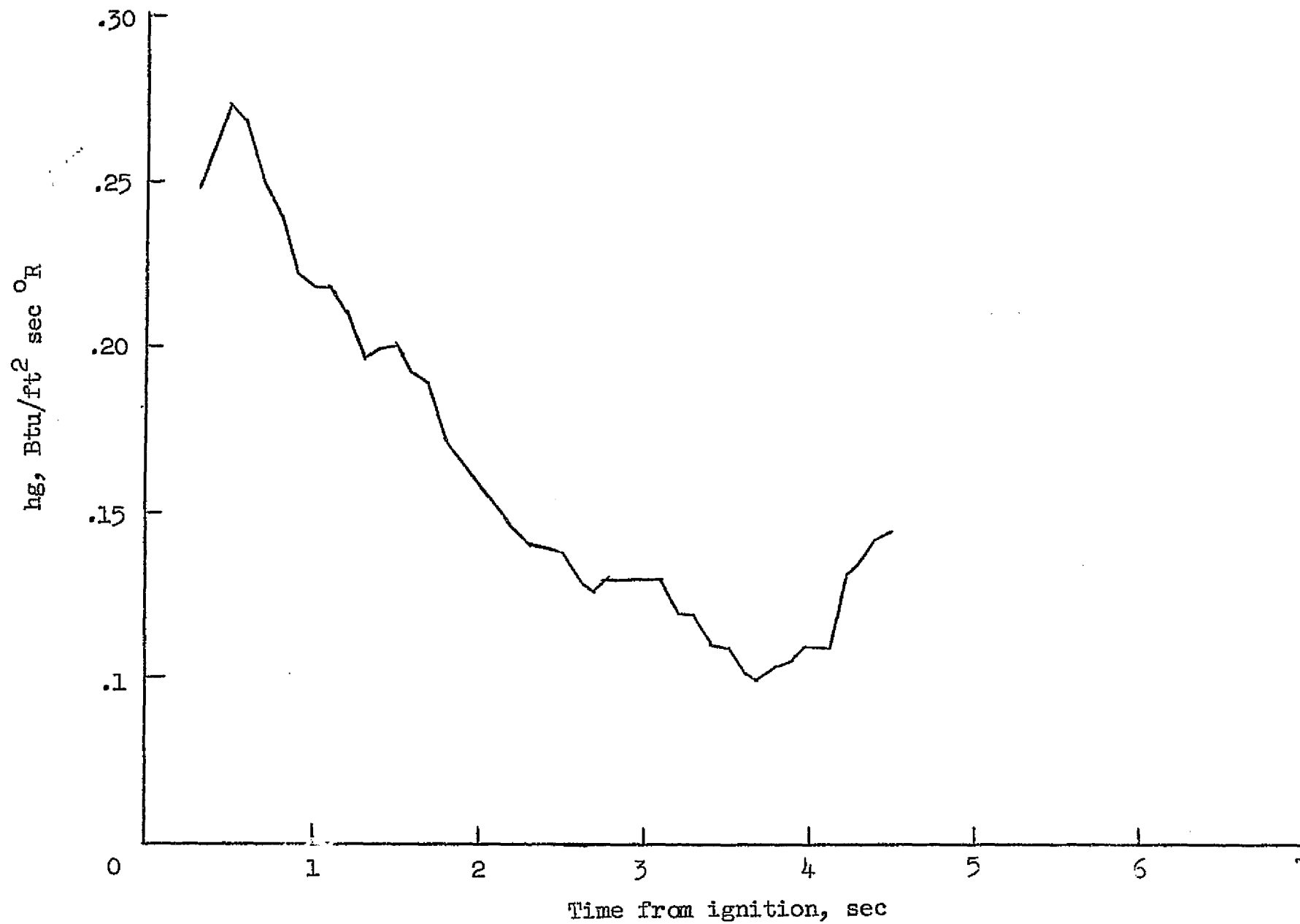


Figure 32. Convective heat-transfer coefficient vs burn time. Throat calorimeter -
 $P_c = 410 \text{ psia}$

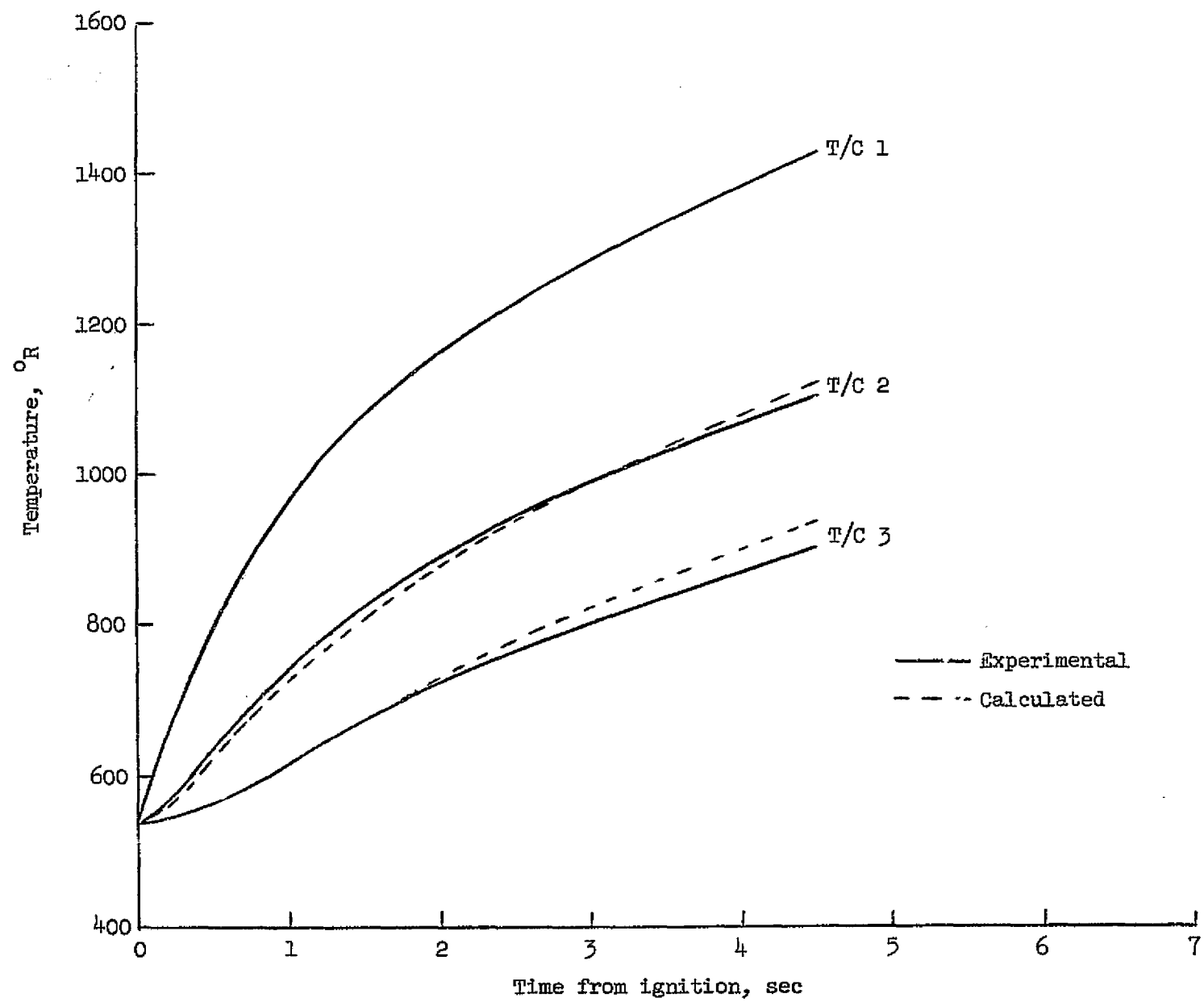


Figure 33. Comparison of experimental and calculated temperature response of thermocouples 1, 2, and 3. Divergent calorimeter - $P_c = 410$ psia

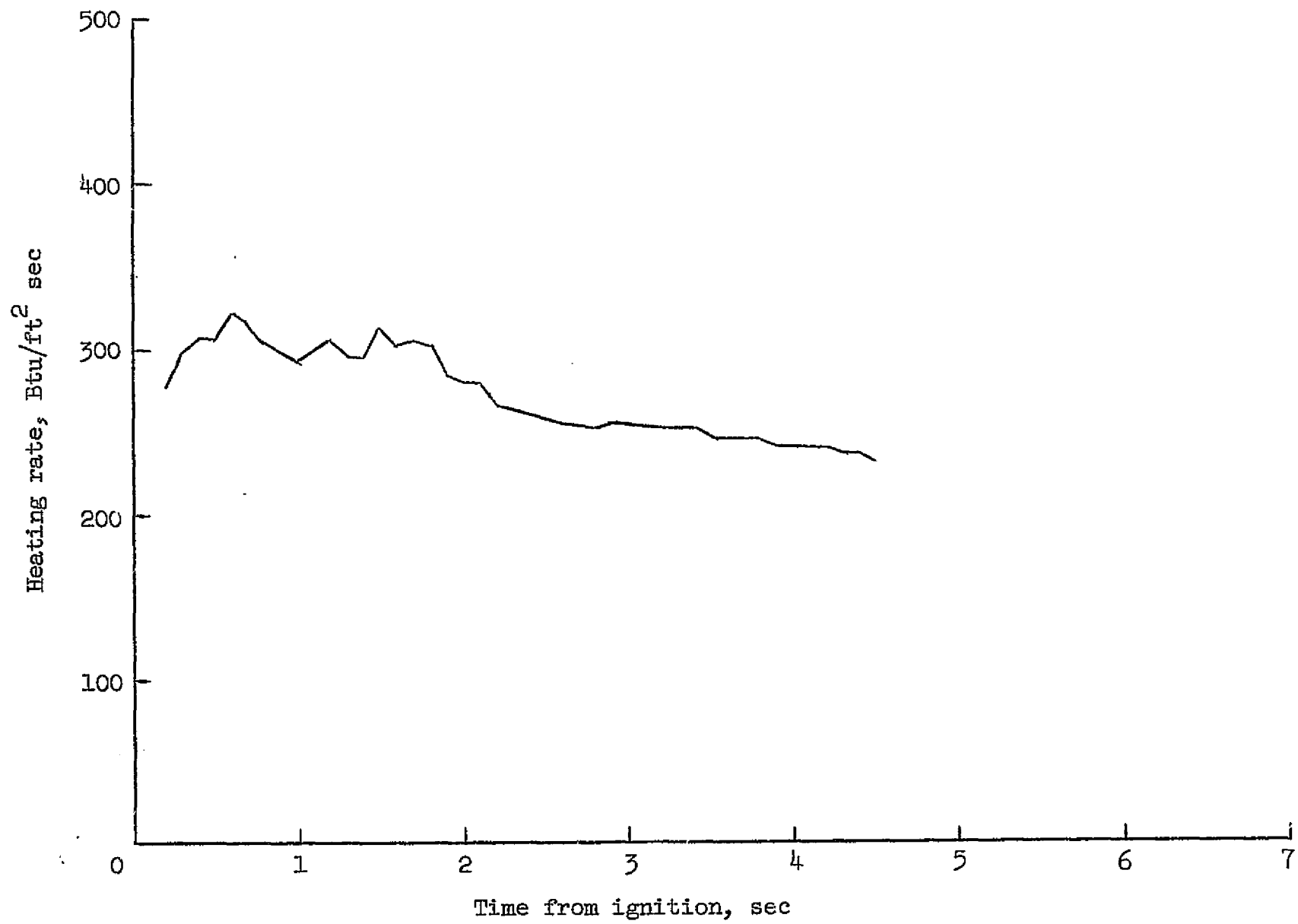


Figure 34. Heating rate vs burn time. Divergent calorimeter - $P_c = 410$ psia

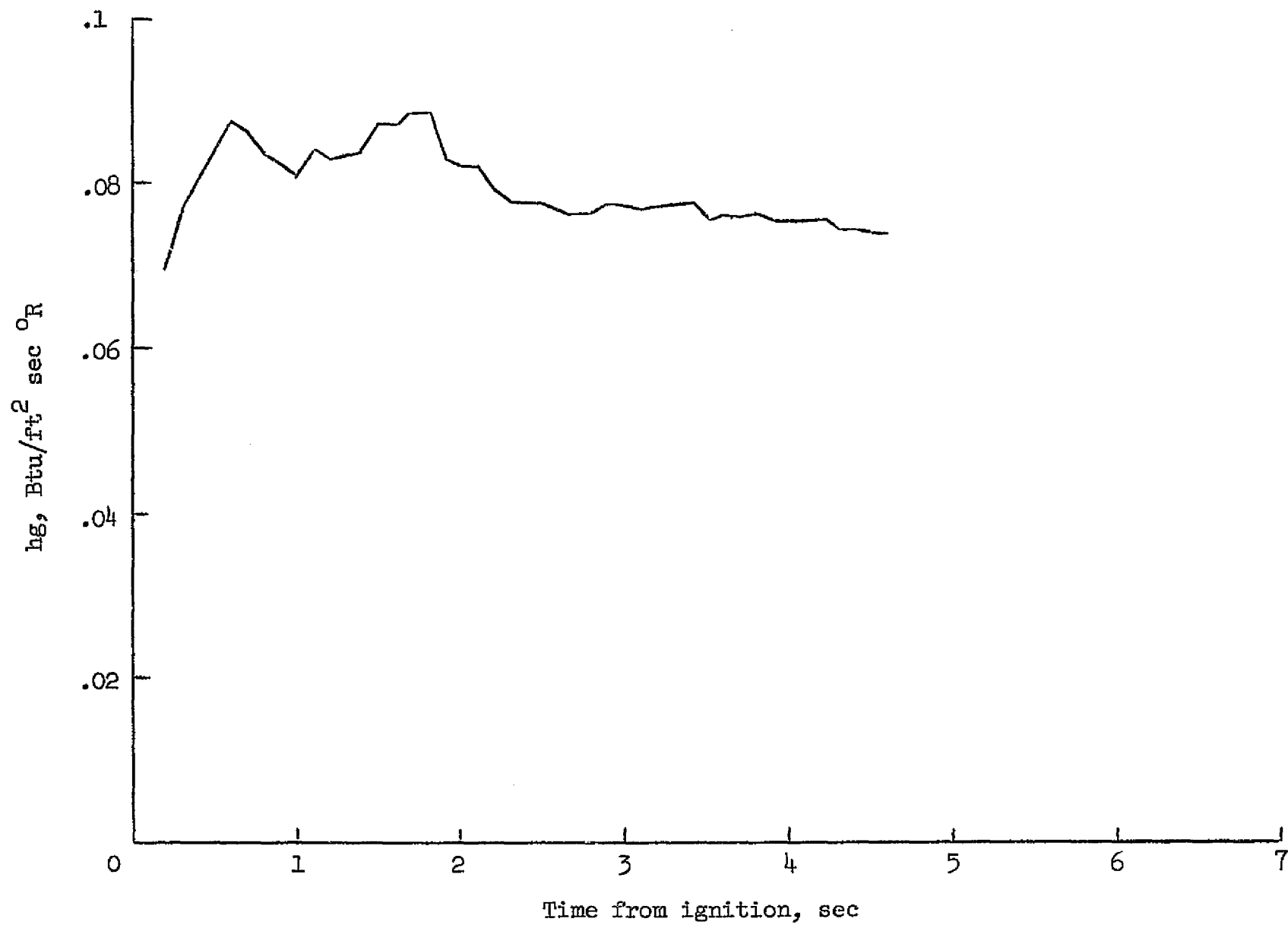


Figure 35. Convective heat-transfer coefficient vs burn time. Divergent calorimeter - $P_c = 410$ psia

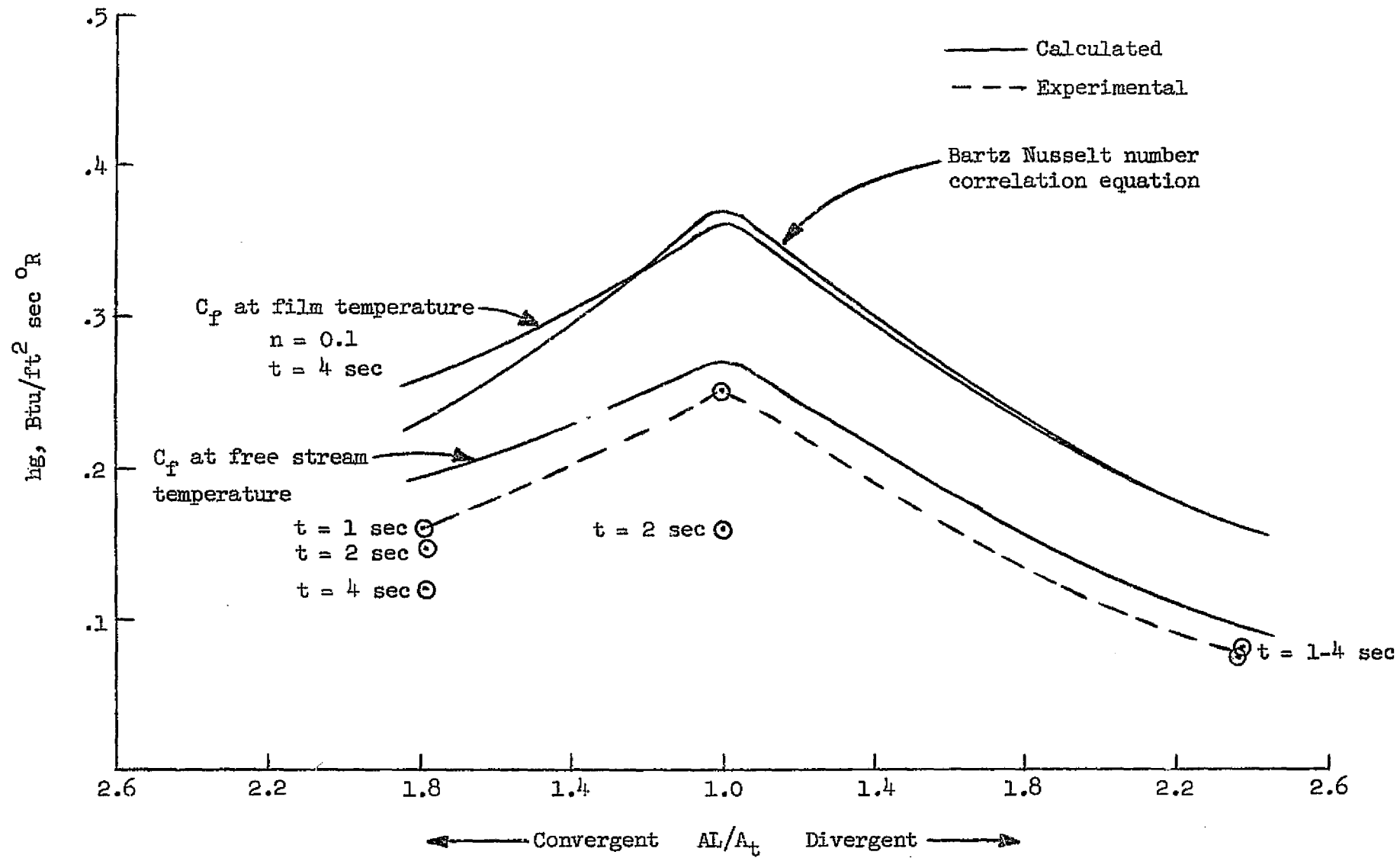


Figure 36. Comparison of analytical and experimental heat-transfer coefficients - $P_c = 410 \text{ psia}$

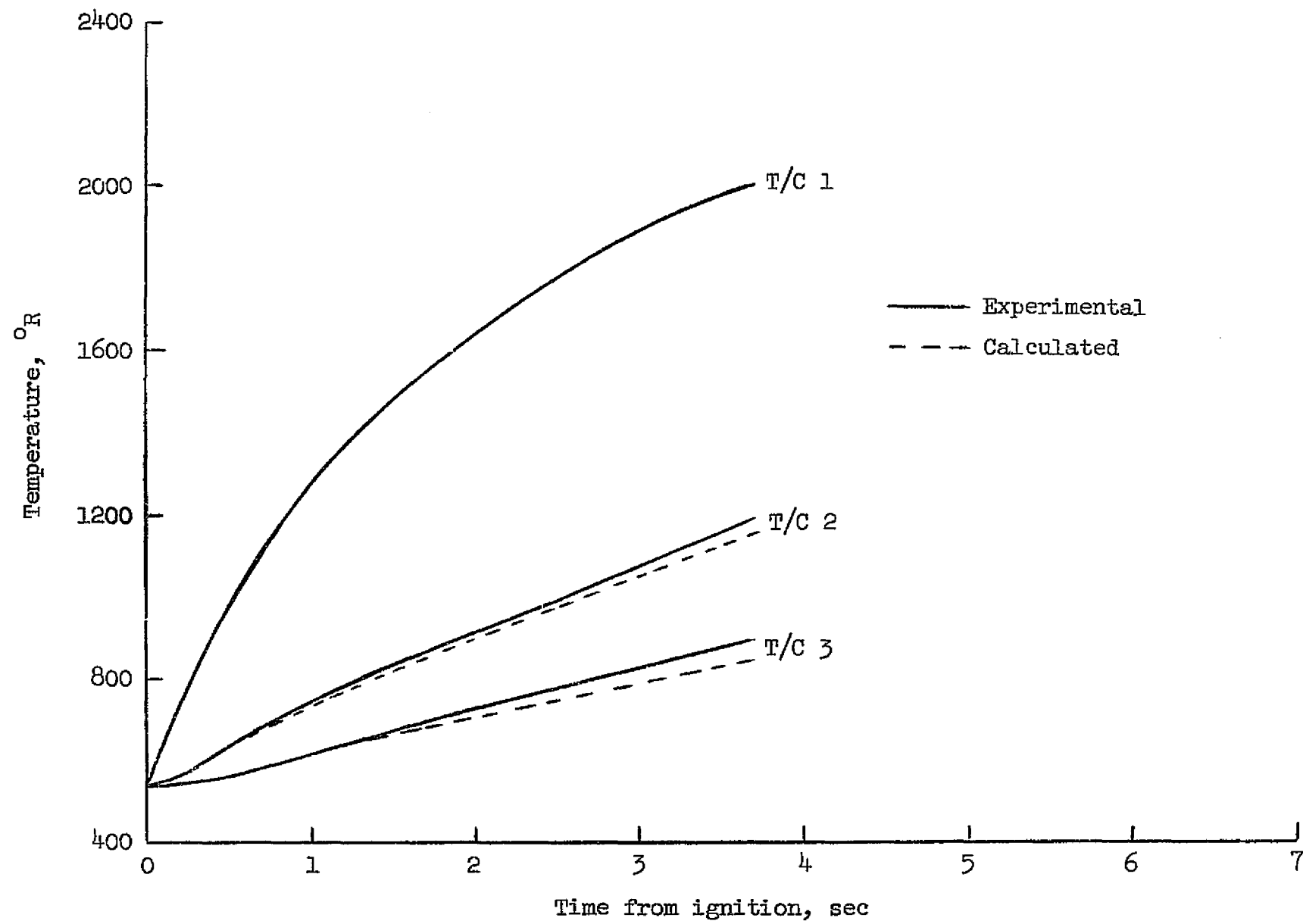


Figure 37. Comparison of experimental and calculated temperature response of thermocouples 1, 2, and 3. Convergent calorimeter - $P_c = 742$ psia

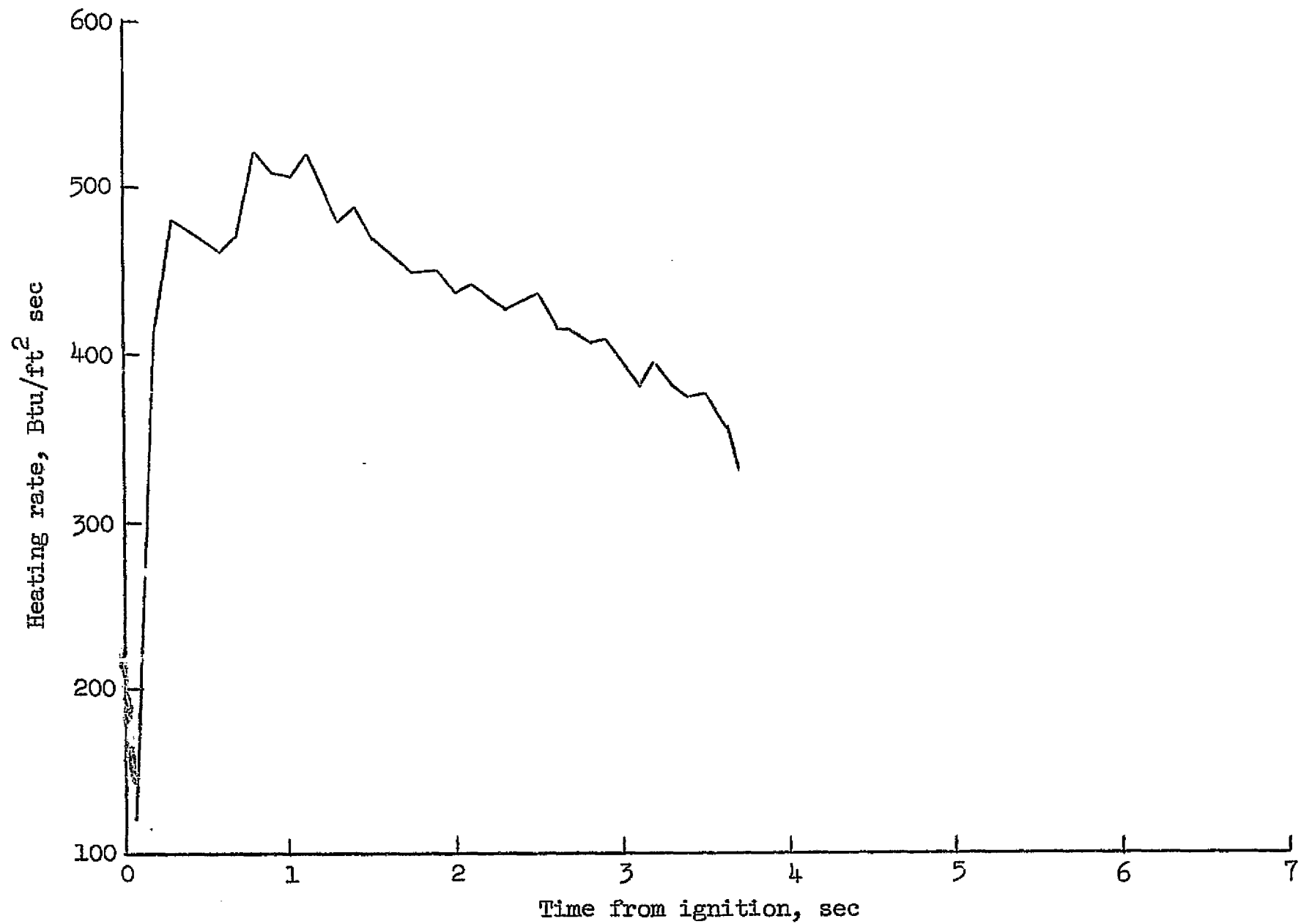


Figure 38. Heating rate vs burn time. Convergent calorimeter - $P_c = 742$ psia

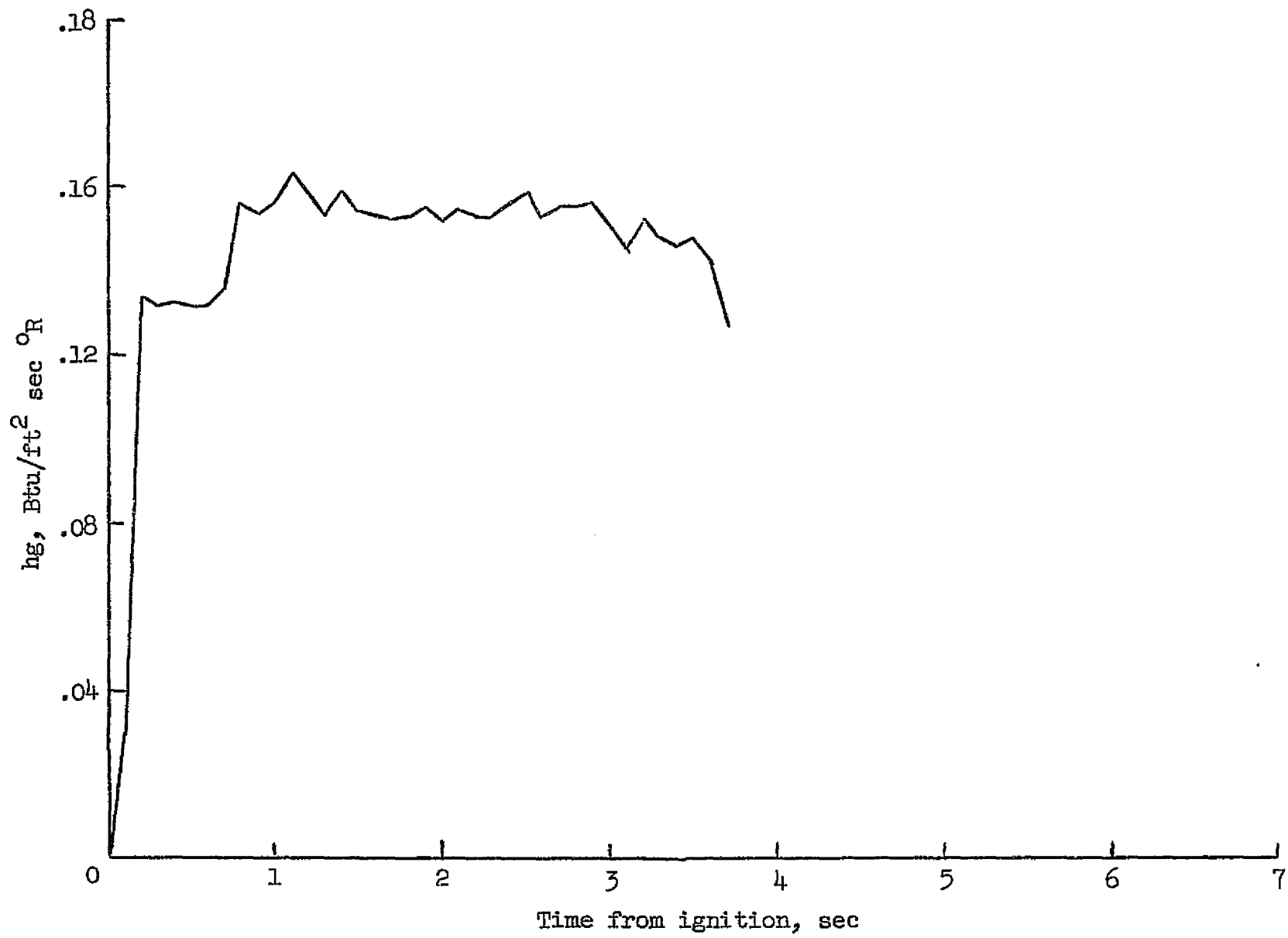


Figure 39. Convective heat-transfer coefficient vs burn time. Convergent calorimeter - $P_c = 742$ psia

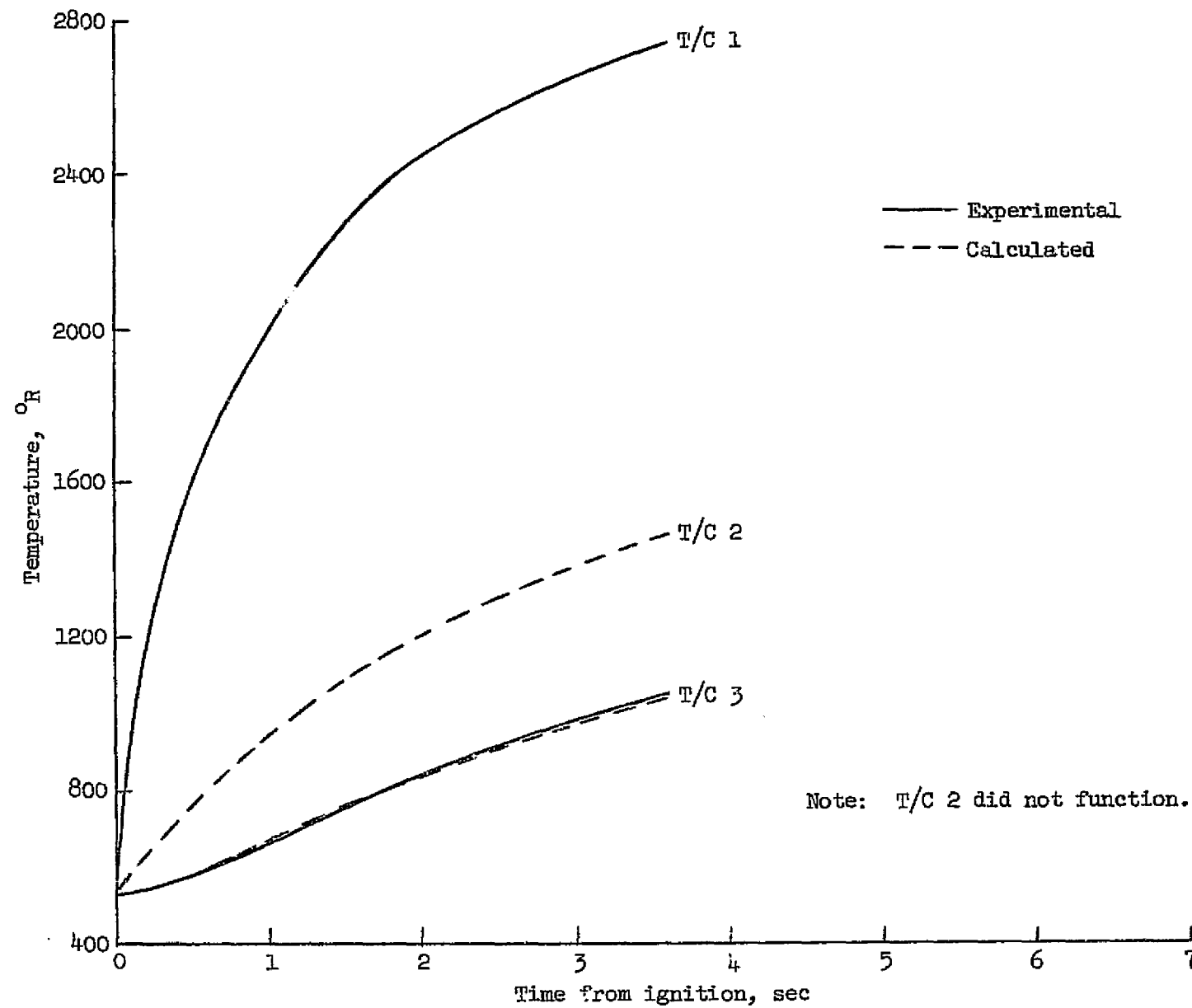


Figure 40. Comparison of experimental and calculated temperature response of thermocouples 1, 2, and 3. Throat calorimeter - $P_c = 742$ psia

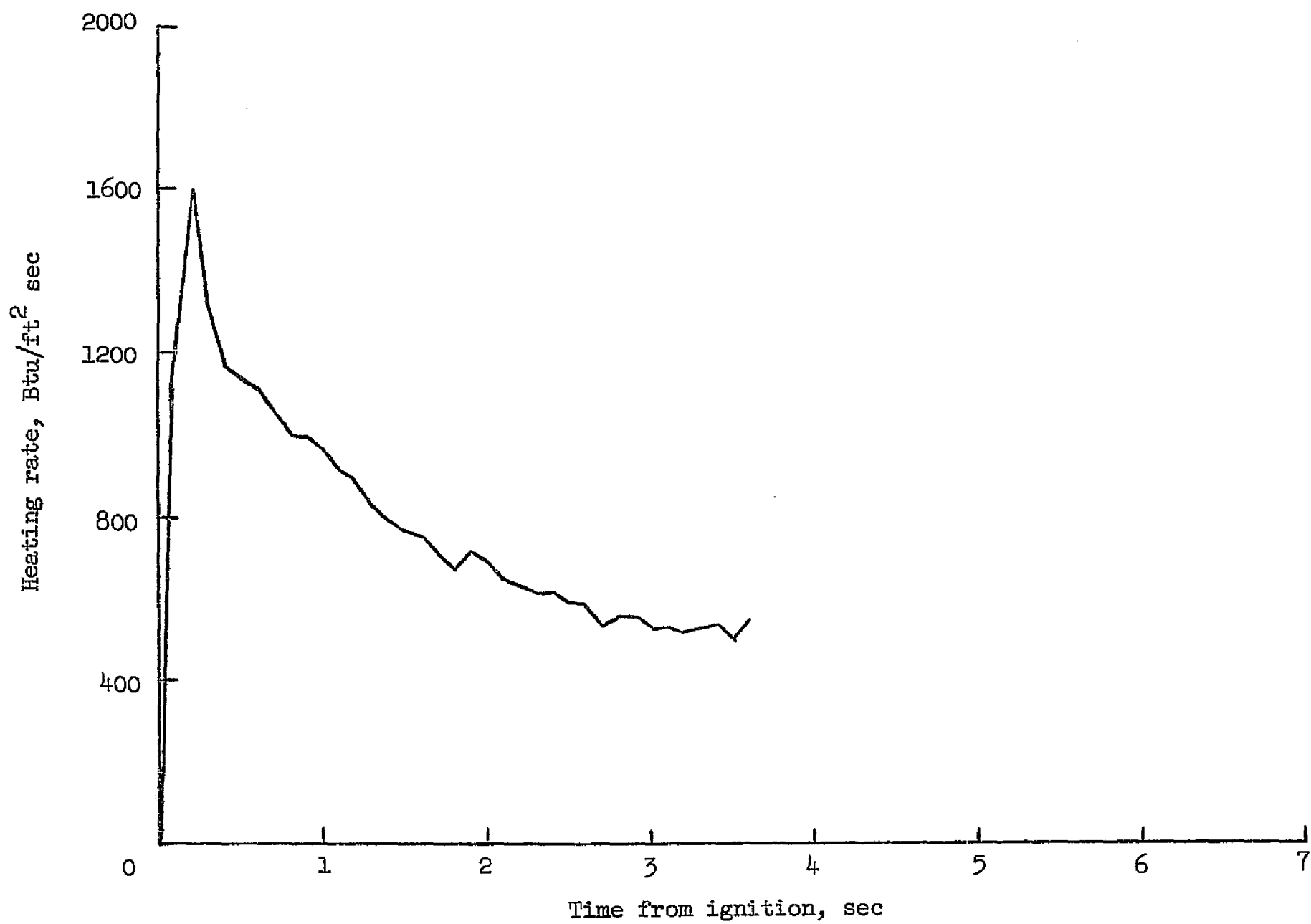


Figure 41. Heating rate vs burn time. Throat calorimeter - $P_c = 742$ psia

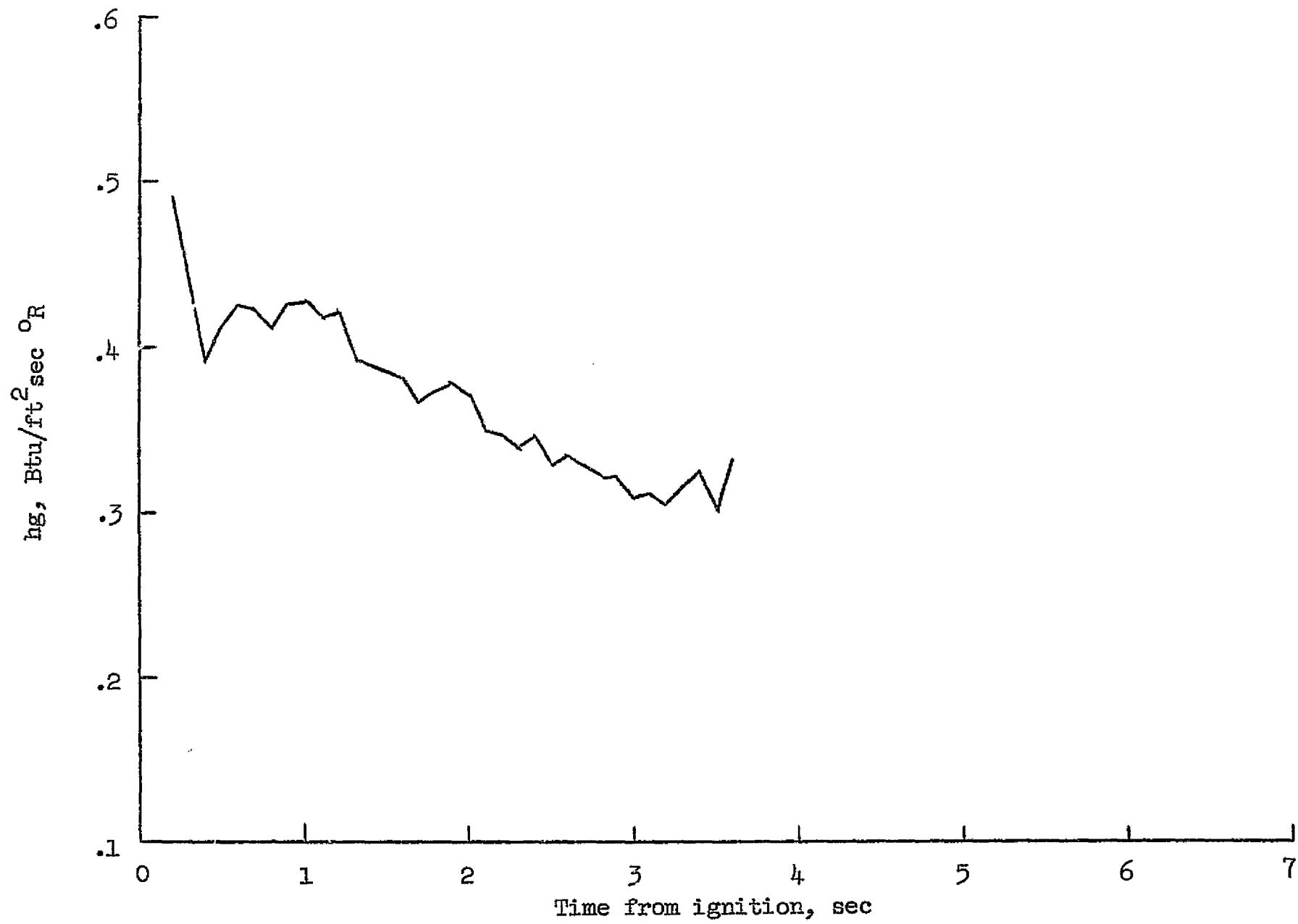


Figure 42. Convective heat-transfer coefficient vs burn time. Throat calorimeter -
 $P_c = 742$ psia

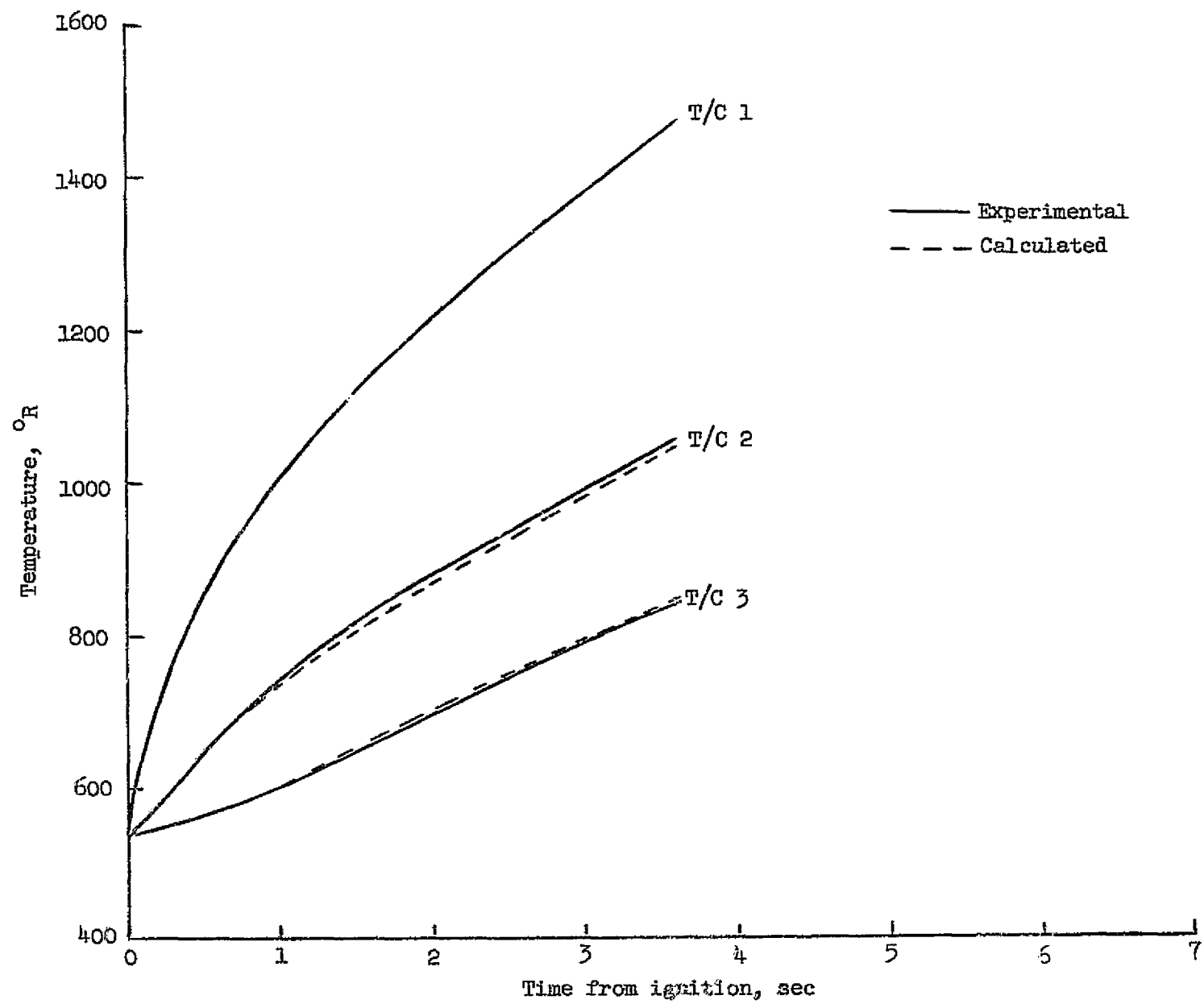


Figure 43. Comparison of experimental and calculated temperature response of thermocouples 1, 2, and 3. Divergent calorimeter - $P_c = 742$ psia.

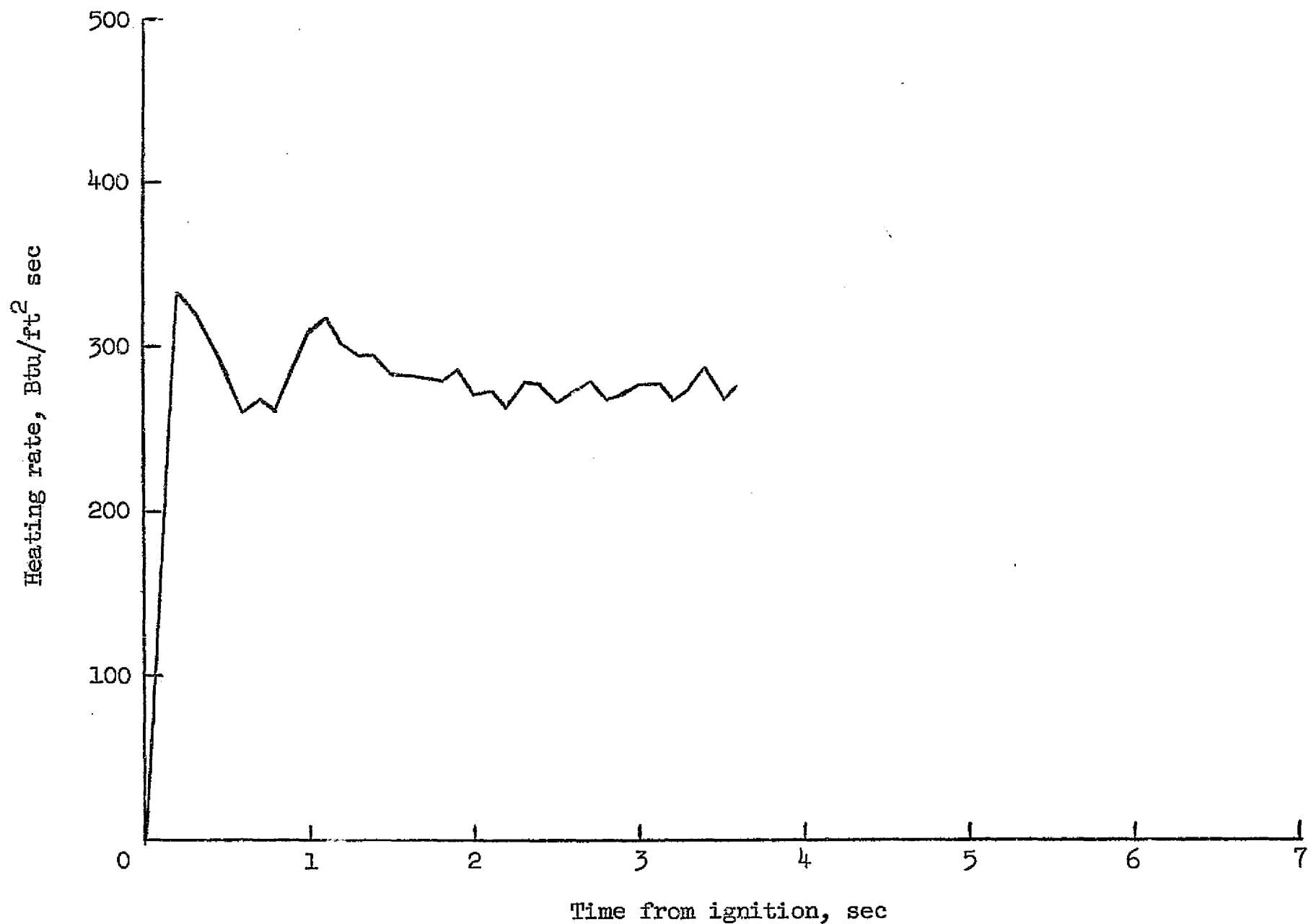


Figure 44. Heating rate vs burn time. Divergent calorimeter - $P_c = 742$ psia

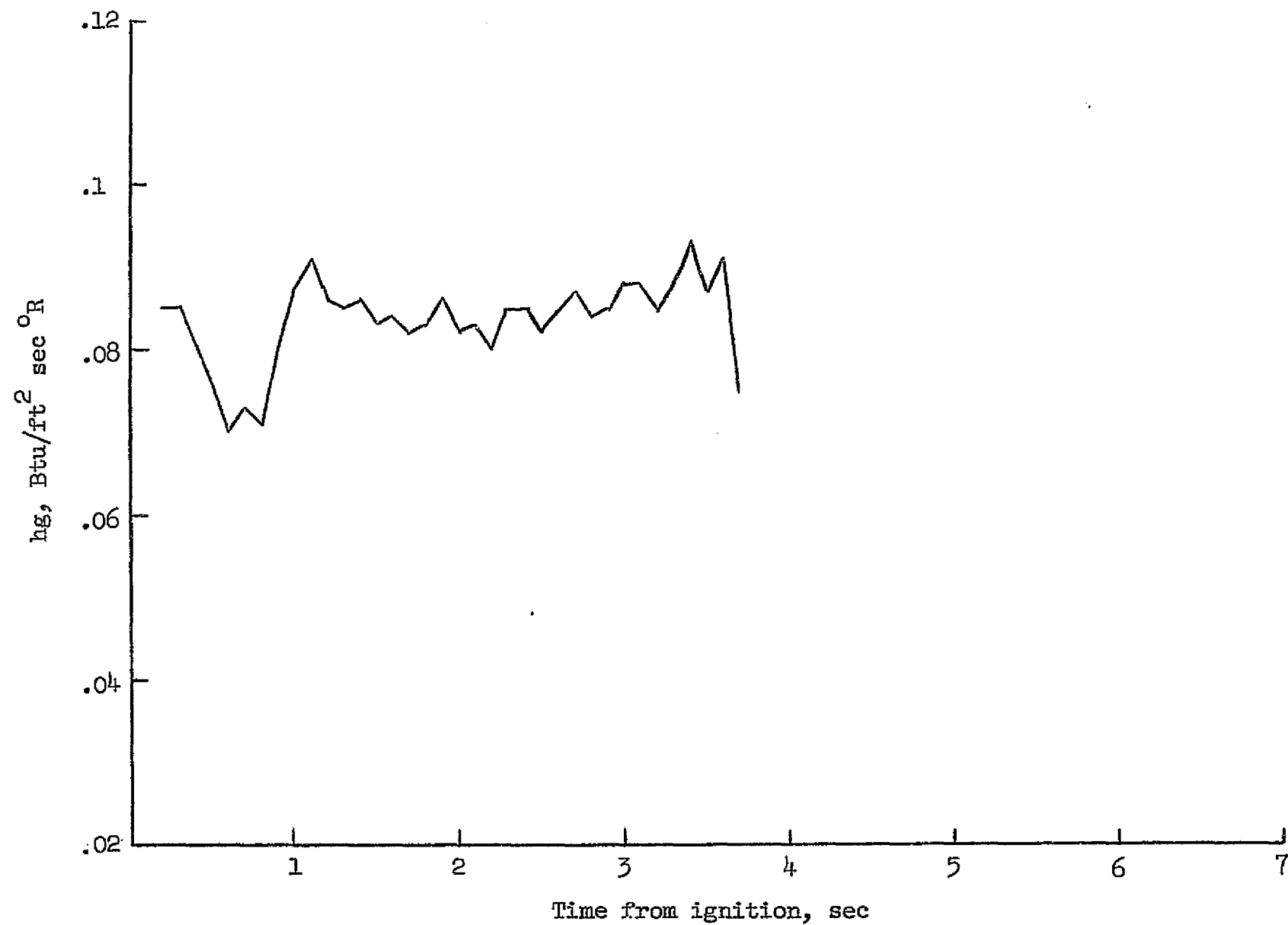


Figure 45. Convective heat-transfer coefficient vs burn time. Divergent calorimeter - $P_c = 742$ psia.

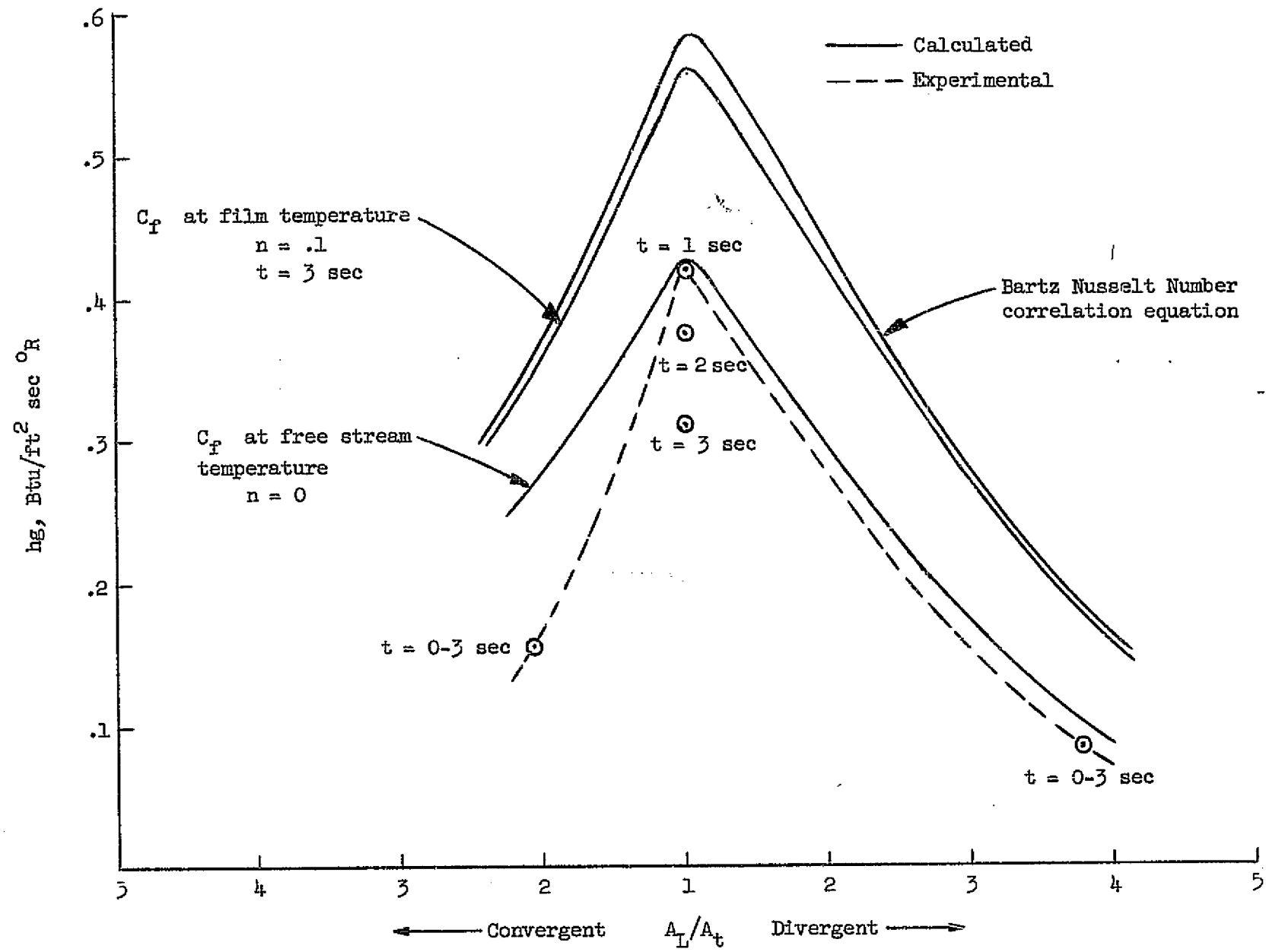


Figure 46. Comparison of experimental and analytical heat-transfer coefficients - $P_c = 742 \text{ psia}$

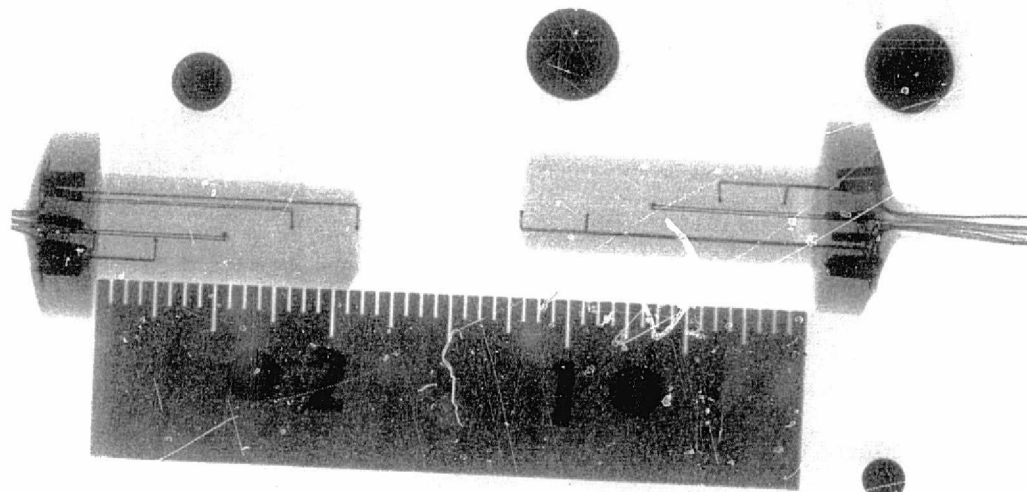


Figure 47. Typical X-ray of calorimeters

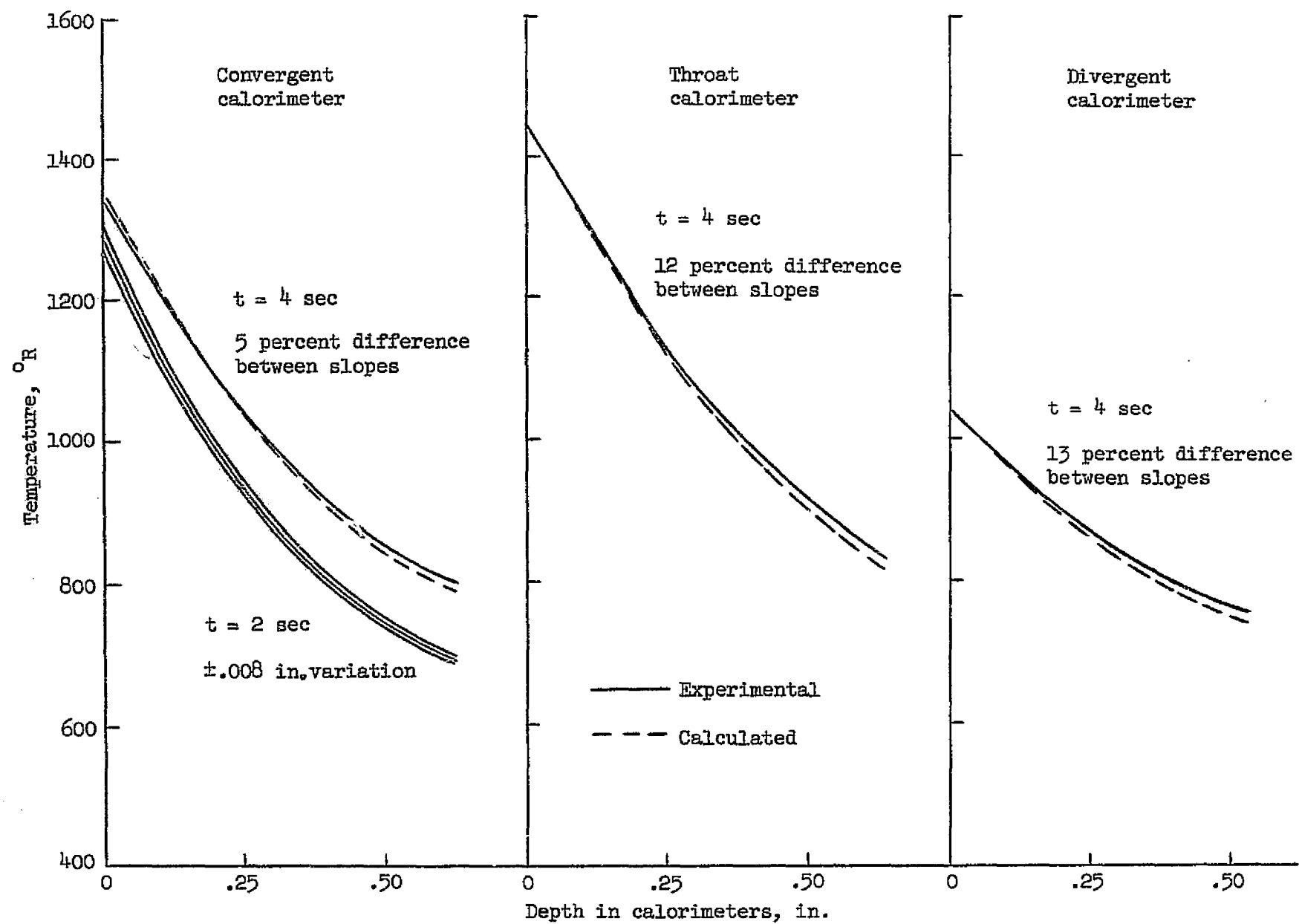


Figure 48. Comparison of analytical and experimental temperature distributions - $P_c = 220$ psia

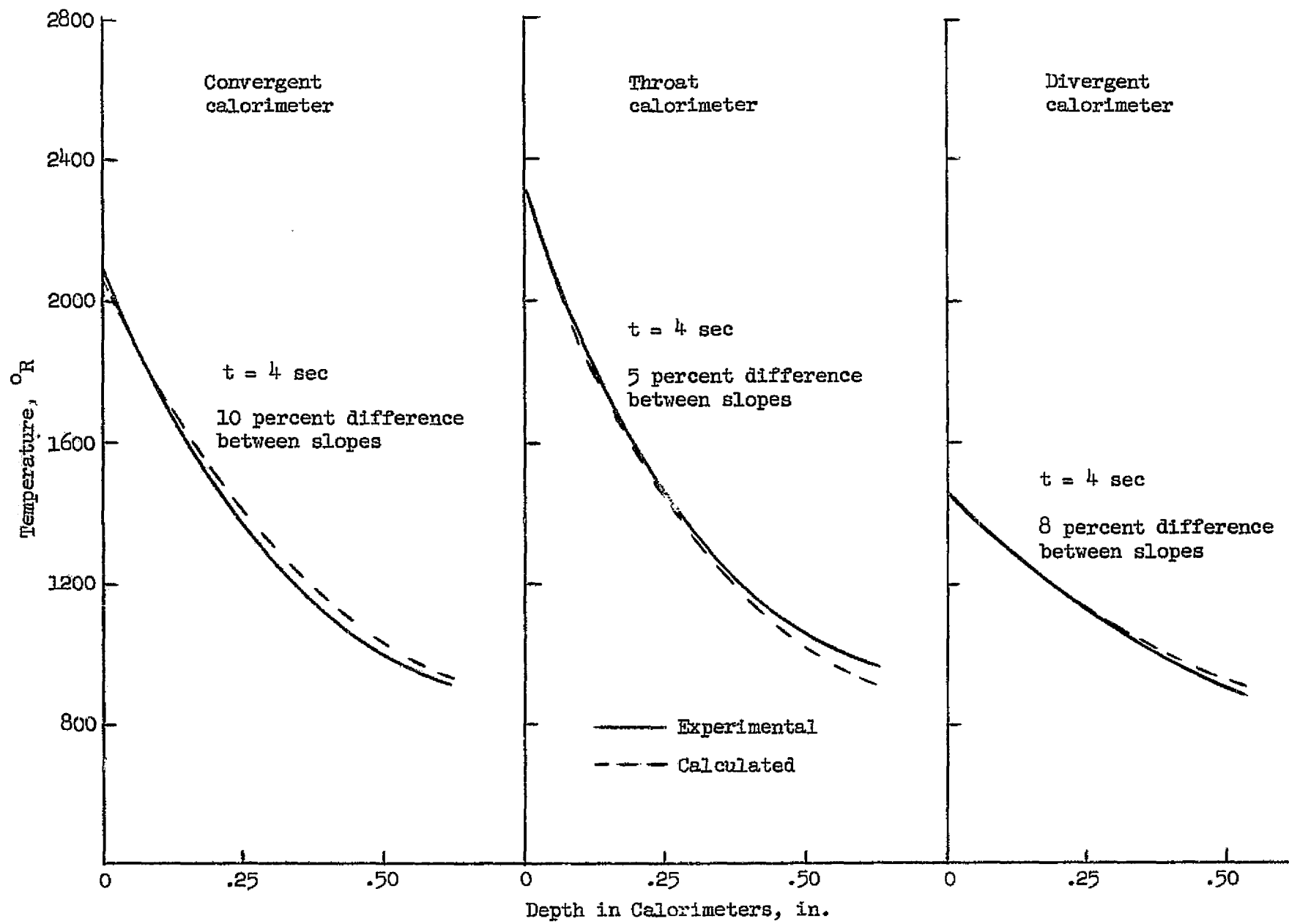


Figure 49. Comparison of analytical and experimental temperature distributions - $P_c = 410$ psia

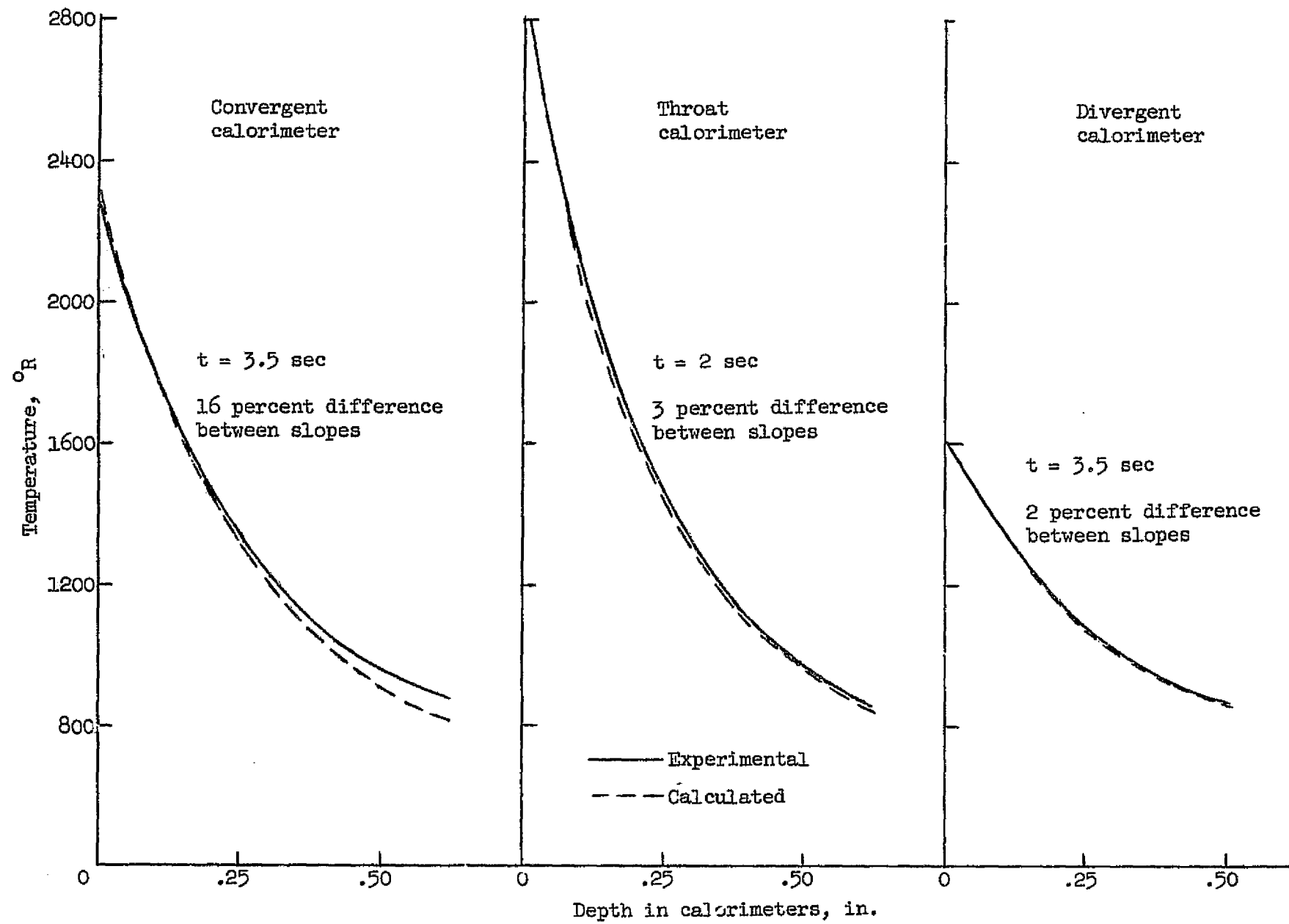


Figure 50. Comparison of analytical and experimental temperature distributions - $P_c = 742$ psia